Coupled-Cluster in Real Space:
CC2 Correlation and Excitation Energies using Multiresolution Analysis

Dissertation zur Erlangung des akademischen Grades
doctor rerum naturalium
(Dr. rer. nat.)

Im Fach: Chemie
Spezialisierung: Physikalische und Theoretische Chemie

eingereicht an der
Mathematisch-Naturwissenschaftlichen Fakultät
Der Humboldt-Universität zu Berlin

von
M. Sc. Jakob Siegfried Kottmann

Präsidentin der Humboldt-Universität zu Berlin

Prof. Dr.-Ing. habil. Dr. Sabine Kunst

Dekan der Mathematisch-Naturwissenschaftlichen Fakultät

Prof. Dr. Elmar Kulke

Gutachter: 1. PD Dr. Denis Usvyat

2. Prof. Robert J. Harrison

3. Prof. Dr. Willem M. Klopper

Tag der mündlichen Prüfung: 25.7.2018

Parts of this work (parts of Ch. 5 and Ch. 6) have already been published in Ref. 1 and Ref. 2 which are explicitly stated on this page.

Specifically Tabs. 5.1, 5.2, 6.1, 6.3, 6.4, 6.7 where adapted with permission from

as well as Tabs. 5.3, 6.11, 6.12, 6.13, 6.15 which were adapted which permission from

Sec. 5.2 and the discussion of the corresponding tables in Sec. 6.2 follows mostly Ref. 1 while Sec. 5.3 and the discussion of the corresponding tables in Sec. 6.3 follows mostly Ref. 2.

Zusammenfassung

In dieser Arbeit werden Algorithmen für die Berechnung elektronischer Korrelations- und Anregungsenergien mittels der Coupled-Cluster Methode auf adaptiven Gittern entwickelt und implementiert. Die jeweiligen Funktionen und Operatoren werden adaptiv durch Multiskalenanalyse dargestellt, was eine Basissatz unabängige Beschreibung mit kontrollierter numerischer Genauigkeit ermöglicht. Gleichungen für die Coupled-Cluster Methode werden in einem verallgemeinerten Rahmen, unabhängig von virtuellen Orbitalen und globalen Basissätzen, neu formuliert. Hierzu werden die amplitudengewichteten Anregungen in virtuelle Orbitale ersetzt durch Anregungen in n-Elektronenfunktionen, welche durch Gleichungen im n-Elektronen Ortsraum bestimmt sind. Die erhaltenen Gleichungen können, analog zur Basissatz abhängigen Form, mit leicht angepasster Interpretation diagrammatisch dargestellt werden. Aufgrund des singulären Coulomb Potentials werden die Arbeitsgleichungen mit einem explizit korrelierten Ansatz regularisiert. Coupled-Cluster singles mit genäherten doubles (CC2) und ähnliche Modelle werden, für geschlossenschalige Systeme und in regularisierter Form, in die MADNESS Bibliothek (eine allgemeine Bibliothek zur Darstellung von Funktionen und Operatoren mittels Multiskalenanalyse) implementiert. Mit der vorgestellten Methode können elektronische CC2 Paarkorrelationsenergien und Anregungsenergien mit bestimmter numerischer Genauigkeit unabhängig von globalen Basissätzen berechnet werden, was anhand von kleinen Molekülen verifiziert wird.

Summary

In this work algorithms for the computation of electronic correlation and excitation energies with the Coupled-Cluster method on adaptive grids are developed and implemented. The corresponding functions and operators are adaptively represented with multiresolution analysis allowing a basis-set independent description with controlled numerical accuracy. Equations for the coupled-cluster model are reformulated in a generalized framework independent of virtual orbitals and global basis-sets. For this, the amplitude weighted excitations into virtuals are replaced by excitations into n-electron functions which are determined by projected equations in the n-electron position space. The resulting equations can be represented diagrammatically analogous to basis-set dependent approaches with slightly adjusted rules of interpretation. Due to the singular Coulomb potential, the working equations are regularized with an explicitly correlated ansatz. Coupled-cluster singles with approximate doubles (CC2) and similar models are implemented for closed-shell systems and in regularized form into the MADNESS library (a general library for the representation of functions and operators with multiresolution analysis). With the presented approach electronic CC2 pair-correlation energies and excitation energies can be computed with definite numerical accuracy and without dependence on global basis sets, which is verified on small molecules.

Acknowledgement

List of Acronyms

BSH   bound-state Helmholtz

CC   coupled-cluster

CCS   coupled-cluster singles

CCSD   coupled-cluster singles doubles

CCSDT coupled-cluster singles doubles triples

CC2   coupled-cluster singles with approximate doubles

CI   configuration interaction

CIS   configuration interaction singles

CISD   configuration interaction singles doubles

CISDT configuration interaction singles doubles triples

LCAO   linear combination of atomic orbitals

MP2   Møller-Plesset perturbation theory of second order

MRA   multiresolution analysis

NEMO   numerical exponential molecular orbital

SVD   singular value decomposition

Contents

List of Figures

List of Tables

1 Introduction

The solution of the quantum mechanical equations which describe the physical properties of molecules and other small particles is, with a few exceptions, unknown in closed analytical form and numerically hard to compute. Usually the full molecular Hamiltonian is approximated by some quantum chemical model for which the Schrödinger equation is solved numerically. Numerical solutions include a further approximation by the introduction of a finite basis in which the solution of the underlying equations are formally expanded. The most common basis for molecular systems is a linear combination of atomic orbitals (LCAO), in most cases realized by atom centred Gaussian functions. LCAO basis-sets are pre-parametrized sets of functions used to represent all involved functions of a given calculation. Although it is in principle possible to construct basis-sets which are generally applicable, the large size and the resulting linear dependencies of such sets makes their usage impractical. This results in a vast amount of available basis-sets for each atom[a] specialized for specific models and properties. The error resulting from the incompleteness of the basis set depends on the underlying quantum chemical model as well as on the system of interest and can usually not be accessed in a general way. Apart from many advantages like the rapid evaluation of integrals, major drawbacks of LCAO based approaches are the inaccessible numerical error and the non-universality of most sets. An alternative approach is multiresolution analysis (MRA): A general framework to represent arbitrary functions adaptively and with given numerical precision on a spatial grid. Instead of expanding every function into the same globally defined basis-set, adaptive local refinement of the grid results in an optimized representation with controlled accuracy for each individual function making MRA a general black-box framework when it comes to numerical representation. MRA based solvers have been developed for several applications like total ground state energies[5–7] and properties,[8,9] as well as for excitation energies[10–12] and magnetic properties.[13]

Quantum chemical models which describe correlated electrons show slow convergence with respect to the size of the underlying basis-sets which is mostly due to the electronic cusp.[14,15] The development of explicitly correlated methods (see Refs. 16, 17 for an introduction), where the electronic cusp is represented explicitly, improved the basis set convergence significantly for ground state correlation energies. Due to the singular Coulomb potential, explicitly correlated ansätze are unavoidable for practical implementations of correlated models based on MRA.[6,18]

In order to compute accurate electronic excitation energies, the underlying basis (-set) has to represent the functions associated with the ground and the excited state in a balanced way.

---

[a]the EMSL Basis Set Library lists for example 394 different basis-sets for the carbon atom.[3,4]

This especially affects explicitly correlated models for excitation energies making the development of those approaches more difficult than for ground state energies.[19–21] Approaches based on MRA have the potential to describe all functions with accuracy and balance. In currently developed approaches for electronic excitation energies, electron correlation is taken into account either in an averaged way[11] or via density functionals[10,12] but not with correlated electron pairs as it is done in (truncated) coupled-cluster models. This motivates the following work in which an MRA based framework for the computation of coupled-cluster ground state correlation energies and excitation energies is developed and implemented for closed shell coupled-cluster singles with approximate doubles (CC2)[22] and related models.

1.1 Quantum Mechanics and Hilbert Spaces

In quantum mechanics the state of a physical system is described in terms of wavefunctions and the time evolution of the corresponding state is determined by the time-dependent Schrödinger equation

$$i\frac{\partial}{\partial t}\Psi\left(\mathbf{r},t\right) = \hat{\mathrm{H}}\Psi\left(\mathbf{r},t\right), \tag{1.1}$$

with the time-dependent wave function Ψ and the Hamiltonian $\hat{\mathrm{H}}$. The explicit form of the Hamiltonian depends on the physical system. In many cases it is sufficient to solve for the stationary solutions of the time-dependent Schrödinger equations which is equivalent to solving the time-independent Schrödinger equation

$$\hat{\mathrm{H}}\Psi\left(\mathbf{r}\right) = E\Psi\left(\mathbf{r}\right). \tag{1.2}$$

Wavefunctions which describe quantum mechanical systems are elements of a complete inner product vector space, called Hilbert space. In real-space representation (meaning that the wave function is a function of the particle coordinates) this Hilbert space is the Lebesgue space $L^2\left(\Omega\right)$ which is the space of square-integrable functions on the domain $\Omega \subseteq \mathbb{R}$.[a] Functions of $L^2\left(\Omega\right)$ will be denoted either in braket form $|f\rangle \in L^2\left(\Omega\right)$ or explicitly as functions $f\left(x\right)$ with $x \in \Omega$. The inner product on $L^2\left(\Omega\right)$ is given by

$$\langle\varphi|\psi\rangle \equiv \langle\varphi|\psi\rangle_{L^2} = \int_\Omega \mathrm{d}r\varphi^*\left(r\right)\psi\left(r\right). \tag{1.3}$$

$L^2\left(\Omega\right)$ is separable meaning that one can always find a countable subset which is dense in $L^2\left(\Omega\right)$ so that every function of $L^2\left(\Omega\right)$ can be approximated by a sequence of functions of this subset. The continuous functions of $L^2\left(\Omega\right)$ or the set of all polynomials on the domain Ω are for example such dense subsets.[23] A set of functions $\{\varphi_i\}$ is called a basis (or a complete

---

[a]Strictly speaking $L^2\left(\Omega\right)$ is the space of equivalence classes of functions whose values only differ on a null set of their support (See for example Ref. 23). For two functions f_1 and f_2 of such an equivalence class it holds that $\|f_1 - f_2\|_{L^2(\Omega)} = 0$. Often the phrasing $f_1 = f_2$ *a.e.* (equality almost everywhere) is used to emphasis this. In order to simplify notation the *a.e.* statement will be dropped in this work.

orthonormal system) of $L^2(\Omega)$ if the following relations hold[a]

$$\sum_i |\varphi_i\rangle\langle\varphi_i| = 1 \quad \text{and} \quad \langle\varphi_i|\varphi_j\rangle = \delta_{ij}, \tag{1.4}$$

stating that the set is complete and orthonormal. $L^2(\Omega)$ functions can then be represented as

$$|f\rangle = \sum_i c_i|\varphi_i\rangle, \quad c_i = \langle\varphi_i|f\rangle. \tag{1.5}$$

The coefficients c_i are elements of the Hilbert space $\ell^2(E)$ with the discrete domain $E \subseteq \mathbb{Z}$ and the inner product

$$\langle c|d\rangle_{\ell^2} = \sum_{i \in E} c_i^* d_i. \tag{1.6}$$

For finite E, the canonical basis for $\ell^2(E)$ are the usual unit vectors and the inner product is the usual Euclidean inner product. For N-dimensional domains Ω^N the corresponding space is $L^2(\Omega^N)$.

1.2 The Electronic Schrödinger Equation

The Hamiltonian for molecules contains the kinetic energy operators for all electrons and all nuclei as well as the corresponding Coulomb potentials. If the Born-Oppenheimer approximation is applied the molecular Schrödinger equation can be separated resulting into two equations, one describing the electronic and one the nuclear wave function. In the electronic Schrödinger equation the nuclei are represented as fixed points and the corresponding electronic wave function only depends parametrically on those points. The electronic Hamiltonian contains the kinetic energy operator ($\hat{T}$) of the electrons and the Coulomb potential of the electron-electron ($\hat{G}$) as well as electron-nuclei (V_{ne}) interaction[b]

$$\hat{H} = \hat{T} + \hat{G} + V_{ne}, \tag{1.7}$$

if the Hamiltonian describes an N_e-electron system with N_n nuclei the corresponding operators are sums of one- and -two-electron operators

$$\hat{T} = -\frac{1}{2}\sum_{i=1}^{N_e} \nabla_i^2, \tag{1.8}$$

---

[a]$|f\rangle\langle g|$ with $f, g \in L^2(\Omega)$ denotes an operator which acts on any $h \in L^2(\Omega)$ as $|f\rangle\langle g||h\rangle = |f\rangle \cdot \langle g|h\rangle$.

[b]The constant expression for the Coulomb repulsion of the nuclei is not included here and should be added to the total electronic energy after its calculation.

$$\hat{G} = \sum_{i<j}^{N_e} g_{ij}, \quad g_{ij} = \frac{1}{\|\mathbf{r}_i - \mathbf{r}_j\|}, \tag{1.9}$$

$$V_{\text{ne}} = \sum_{i=1}^{N_e} v_{\text{ne}}(\mathbf{r}_i), \quad v_{\text{ne}}(\mathbf{r}) = -\sum_{a=1}^{N_n} \frac{Z_a}{\|\mathbf{R}_a - \mathbf{r}\|}, \tag{1.10}$$

with the electronic and nuclear coordinates $\mathbf{r}, \mathbf{R} \in \mathbb{R}^3$.

1.3 One-Electron Wavefunctions

Electrons have an intrinsic degree of freedom called spin. The spin degree of freedom is described by a two-dimensional Hilbert space and the basis functions are usually chosen as the eigenfunctions of the $\hat{s}_z$ operator[a]

$$\hat{s}_z |\pm s\rangle = \pm s|\pm s\rangle, \quad s = \frac{1}{2}. \tag{1.11}$$

The Hilbert space for the electron spin is $\ell\left(\{\pm\frac{1}{2}\}\right)$[b] and the Hilbert space for the electron is constructed from the spatial and spin domains as[c]

$$\mathcal{L}^2 \equiv L^2\left(\mathbb{R}^3\right) \otimes \ell\left(\{\pm\frac{1}{2}\}\right). \tag{1.12}$$

Orthonormal bases for $\mathcal{L}^2$ can be constructed as tensor products between the spatial and spin bases

$$|\chi_p\rangle = |\phi_p\rangle \otimes |s_p\rangle, \quad s_p \in \left\{\pm\frac{1}{2}\right\}. \tag{1.13}$$

Such functions are generally referred to as spin orbitals while the spatial parts ϕ_p are referred to as orbitals. In the canonical case the spin orbitals are eigenfunctions of some one-electron Hamiltonian which is in most cases the Hartree-Fock Hamiltonian introduced in the next section.[d] In this work the common short notation for spin orbitals is used

$$|\chi_p\rangle \equiv |p\rangle. \tag{1.14}$$

---

[a]There are various notations for the spin eigenfunctions like $|\frac{1}{2}\rangle \equiv |\uparrow\rangle \equiv |\alpha\rangle$ and $|-\frac{1}{2}\rangle \equiv |\downarrow\rangle \equiv |\beta\rangle$.

[b]Any two distinct points could be chosen as domain. The convenient choice $E = \{\pm\frac{1}{2}\}$ follows Refs. 24 and 25.

[c]This is often written in short notation as $L^2\left(\mathbb{R}^3 \times \{\pm\frac{1}{2}\}\right)$ (see for example Refs. 24 and 25). Let it also be noted here, that electrons are actually elements of the Sobolev space H^1 which is a Hilbert space with the inner product $\langle f|g\rangle_{H^1} = \langle f|g\rangle_{L^2} + \langle \nabla f|\nabla g\rangle_{L^2}$. Restricting the wave function to H^1 ensures the kinetic energy $E_{\text{kin}} = \frac{1}{2}\langle \nabla\Psi|\nabla\Psi\rangle$ to be finite. Further details can be found for example in Refs. 26 and 24.) In the scope of this work it is not necessary to explicitly use this restriction.

[d]In other approaches the spin orbitals are not exactly eigenfunctions of the corresponding one-electron Hamiltonian, but can be constructed from them by a unitary transformation (*e.g.* localized orbitals). In this work canonical orbitals are used.

1.4 Multi-Electron Wavefunctions

Wavefunctions of many electrons have to fulfil the Pauli principle and are therefore antisymmetric with respect to the permutation of electrons. The Hilbert space for N-electron wave functions can be constructed by the antisymmetric product of the one-electron space[a]

$$\mathcal{L}_N^2 \equiv \bigwedge_{n=1}^N \mathcal{L}^2 \equiv \left\{ f \in \mathcal{L}^{\otimes N} : f \text{ is antisymmetric under particle permutations} \right\}. \tag{1.15}$$

Correspondingly a basis of the $\mathcal{L}_N^2$ space can be constructed by normalized antisymmetric products of the one-electron basis. Such basis functions are called Slater determinants since they can be written as formal determinants over the one-particle basis functions. If the electronic wave function is approximated by a single determinant a variational optimization of the involved one-electron spin orbitals leads to the Hartree-Fock equations (see Ref. 27 for a detailed introduction)

$$\hat{f}|i\rangle = \epsilon_i |i\rangle, \tag{1.16}$$

where the Fock operator $\hat{f}$ is an effective one-electron operator given by

$$\hat{f} = -\frac{\nabla^2}{2} + \hat{v}_f, \quad \hat{v}_f = v_{ne} + \hat{j} - \hat{k}. \tag{1.17}$$

The Coulomb operator $\hat{j}$ and exchange operator $\hat{k}$ are defined by

$$\hat{j} \equiv \sum_k \langle k|g_{12}|k\rangle, \quad k \in \mathcal{I} \tag{1.18}$$

$$\hat{k}|f\rangle = \sum_k |k\rangle \cdot \langle k|g_{12}|f\rangle, \quad \forall f \in \mathcal{L}_1^2, \ k \in \mathcal{I}, \tag{1.19}$$

with the notation for convolutions as

$$\langle p|g_{12}|q\rangle \equiv \sum_s \int d\mathbf{r}_2 \chi_p(\mathbf{r}_2, s) \, g_{12} \chi_q(\mathbf{r}_2, s). \tag{1.20}$$

The index set $\mathcal{I}$ indexes the spin orbitals which form the Hartree-Fock determinant (also referred to as occupied spin orbitals). In addition to the occupied spin orbitals the Fock operator has additional eigenfunctions which are called virtual (or unoccupied) spin orbitals. Occupied and virtual spin orbitals together form a orthonormal basis for the one-electron space $\mathcal{L}^2$. The usual labelling convention in quantum chemistry is i, j, k, l for occupied, a, b, c, d for virtual and p, q, r, s for general spin orbitals. Virtual and occupied orbitals span closed subspaces and the projectors from $\mathcal{L}^2$ onto those spaces are

$$\mathcal{O} = \sum_i |i\rangle\langle i|, \quad \mathcal{Q} = \sum_a |a\rangle\langle a| = 1 - \mathcal{O}. \tag{1.21}$$

---

[a]The multi-electron wave function also has finite kinetic energy. The corresponding antisymmetric Sobolev space is[25] $\mathcal{H}_N^1 = \left(H^1 \left(\left(\mathbb{R}^3 \times \{\pm\frac{1}{2}\} \right)^N \right) \right) \cap \left(\bigwedge_{n=1}^N L^2 \left(\mathbb{R}^3 \times \{\pm\frac{1}{2}\} \right) \right).$

1 Introduction

In order to accurately describe a multi-electronic system the representation of its wave function with just one determinant is insufficient since the Coulomb interaction between the electrons can only be taken into account in an averaged way. A correlated wave function can be constructed by using more than one determinant. Additional determinants are usually constructed from the Hartree-Fock determinant by formally exciting electrons into virtual spin orbitals. The Hartree-Fock determinant is then denoted as $|0\rangle$ and is called the reference determinant. Excited determinants constructed are denoted relative to the reference determinant so that $|_{ij\ldots}^{ab\ldots}\rangle$ denotes the determinant where the occupied orbitals $i, j, \ldots$ are replaced by the virtual orbitals $a, b, \ldots$.

The difference between the Hartree-Fock energy and the true eigenvalue of the electronic Schrödinger equation is called correlation energy. Various methods which use excited determinants to calculate the full or approximated correlation energy exist like for example the configuration interaction (CI) and the coupled-cluster (CC) expansion

$$|\text{CI}\rangle \equiv \left(1 + \hat{\mathcal{T}}\right)|0\rangle, \tag{1.22}$$

$$|\text{CC}\rangle \equiv e^{\hat{\mathcal{T}}}|0\rangle, \tag{1.23}$$

where the cluster operator $\hat{\mathcal{T}} = \sum_n \hat{\mathcal{T}}_n$ creates all types of weighted excited determinants

$$\hat{\mathcal{T}}_n|0\rangle = \sum_{i_1} \cdots \sum_{i_n} \sum_{a_1} \cdots \sum_{a_n} t_{i_1,\ldots,i_n}^{a_1,\ldots,a_n} |_{i_1,\ldots,i_n}^{a_1,\ldots,a_n}\rangle. \tag{1.24}$$

CC and CI expansion are formally exact but their computational complexity scales exponentially with system size. In order to reduce the complexity, approximations to the full CC (and CI) expansions are introduced where the cluster operator is truncated after some excitation level. The resulting truncated models are then called CCS, CCSD, CCSDT, ... (or CIS, CISD, CISDT, ...) where S, D, T stand for singles, doubles, triples *etc.*. Perturbative approaches using the Fock operator as zeroth order Hamiltonian are also in wide use. Prominent examples are Møller-Plesset perturbation theory of second order (MP2) and CC2 (see Ch. 5).

1.5 Adaptive-Real-Space and Fixed-Basis-Set Methods

One- and multi-electron function spaces can be approximated by countable infinite bases where in numerical applications the basis is truncated at some point. In quantum chemistry atomic orbitals are most frequently used as basis for the spatial part of the one-electron space. This approach is referred to as linear combination of atomic orbitals (LCAO) and the most prominent realization is by Gaussian functions which mimic the properties of atomic orbitals. LCAO based methods profit from the fast and efficient evaluation of Gaussian integrals but are often hard to converge systematically towards the basis-set limit. Furthermore they are not universal since most basis sets are constructed for specific types of properties. Alternatively the wave function can be represented on a grid in real-space. Grid based representation of functions with locally adaptive resolution can be constructed with multiresolution analysis (MRA) where one of the main differences to LCAO is that MRA represents each function in a different optimized basis while LCAO represents all functions with the same fixed basis-set. Real-space methods are not necessarily adaptive (see for example the BIGDFT project[28,29]) but in this work the term real-space will refer to adaptive methods like MRA. In the following the Hartree-Fock equations (1.16) are used to give an instructive example of the adaptive real-space and fixed-basis (LCAO) approach.

In a fixed global basis like LCAO with Gaussians, the Hartree-Fock equations are called Roothaan-Hall equations[a]

$$\mathbf{FC} = \mathbf{SC}\boldsymbol{\epsilon}, \tag{1.25}$$

with the Fock matrix $\mathbf{F}$, overlap matrix $\mathbf{S}$ and the LCAO coefficient matrix $\mathbf{C}$ (see Ref. 27 for details). Through the LCAO basis the Hartree-Fock equations are transferred into a standard linear algebra problem which is solved self-consistently resulting in N_e occupied and $N_\mathrm{b} - N_e$ virtual spin orbitals where N_b is the number of LCAO basis functions and N_e the number of electrons.

The real-space Hartree-Fock equations (1.17) were already given in the last section. For MRA based applications it is beneficial to rearrange the equations to[5]

$$\left(-\nabla^2 + \mu^2\right)|i\rangle = -2\hat{\mathrm{v}}_\mathrm{f}|i\rangle, \quad \mu = \sqrt{-2\epsilon_i}, \tag{1.26}$$

so that an equation to determine the Hartree-Fock orbitals can be obtained by

$$|i\rangle = -2\left(-\nabla^2 + \mu^2\right)^{-1}\hat{\mathrm{v}}_\mathrm{f}|i\rangle \equiv -2\mathcal{G}_\mu\left(\hat{\mathrm{v}}_\mathrm{f}|i\rangle\right). \tag{1.27}$$

For bound states ($\epsilon_i < 0$), the Green's operator $\mathcal{G}_\mu$ is a convolution operator with the bound-state Helmholtz (BSH) Green's function as kernel

$$\mathcal{G}_\mu f\left(\mathbf{r}\right) = \int \mathrm{d}\mathbf{r}' G_\mu\left(\|\mathbf{r} - \mathbf{r}'\|\right) f\left(\mathbf{r}'\right). \tag{1.28}$$

---

[a]The name Roothaan-Hall equations refers usually to restricted Hartree-Fock equations (closed-shell) while for unrestricted Hartree-Fock the equations are often called Pople-Nesbet equations.

The BSH Green's function is in d dimensions generally given by[30]

$$G_\mu (r) = \frac{\mu^\alpha}{(2\pi)^{\alpha+1}} \frac{K_\alpha (\mu r)}{r^\alpha}, \quad \alpha = \frac{d}{2} - 1,$$ (1.29)

where K_α is the modified Bessel function of second kind (see the appendix A1 for details). For $d = 3$ the BSH Green's function has the simple form[a]

$$G_\mu (r) = \frac{e^{-\mu r}}{4\pi r}.$$ (1.30)

The real-space Hartree-Fock orbitals are solved self consistently by iterative application of Eq. (1.27) resulting in optimized multiresolution representations of the different occupied orbitals. The formulation as integral equation and the resulting restriction to bound-states can be seen as preconditioner because of its smoothing properties and since it restricts the vast number of unbound states from the solution space.[5] While virtual orbitals are a simple by-product of the Roothan-Hall equations (1.25) they are not calculated in the real-space equations (1.27).

The working equations derived in this work are implemented into MADNESS[32,33], a software environment to represent general functions (with currently up to 6 spatial dimensions) and operators with MRA. In Ch. 2 the basic concept of MRA is introduced. A coupled-cluster formulation suitable for adaptive real-space methods is given in Ch. 3 (general framework for ground state correlation energies) and Ch. 4 (linear response). The working equations for closed-shell CC2 and related models are derived in Ch. 5.

---

[a]This follows from the identity $K_{\frac{1}{2}} (r) = \sqrt{\frac{\pi}{2}} \frac{e^{-r}}{\sqrt{r}}$ (see for example Ref. 31).

1.6 Notation and Conventions

Sum Convention   The Einstein sum convention will be used through the whole work (*i.e.* repeated indices are summed over). In some cases the sum convention is not used, but this will be clear from the structure of the corresponding equations (*e.g.* if the corresponding indices are on left and right hand side of the equation).

Index Sets   Occupied Reference spin orbitals are indexed by the set $\mathcal{I} \equiv \{1, 2, \ldots, N_e\}$. The standard convention that elements of $\mathcal{I}$ are denoted as i, j, k, l is used here. Virtual (spin) orbitals (*i.e.* χ_a with $a \notin \mathcal{I}$) are indexed by a, b, c, d and general (spin) orbitals by p, q, r, s. In the real-space formulation all indices refer to occupied orbitals. Up to Ch. 5 the corresponding indices refer to spin orbitals while from Ch. 5 they will refer to closed-shell spatial orbitals indexed by the set $|\mathcal{I}| \equiv \{1, 2, \ldots, N_e/2\}$.

Multi-Index Notation   Bold letters denote multi-indices and the same conventions as for single indices apply. Take for example the multi-index $\mathbf{i}$ representing all indices $i_1, \ldots, i_n$ which are all part of the index set $\mathcal{I}$ over the occupied reference spin orbitals. A general n-fold determinant for arbitrary n and the corresponding amplitude are then denoted as

$$|{}^{\mathbf{a}}_{\mathbf{i}}\rangle \equiv |{}^{a_1,\ldots,a_n}_{i_1,\ldots,i_n}\rangle, \quad t^{\mathbf{a}}_{\mathbf{i}} \equiv t^{a_1,\ldots,a_n}_{i_1,\ldots,i_n}. \tag{1.31}$$

Take for example Eq. (1.24) which can be compactly written with multi-index notation and sum convention

$$\hat{\mathcal{T}}_n|0\rangle = \sum_{i_1} \cdots \sum_{i_n} \sum_{a_1} \cdots \sum_{a_n} t^{a_1,\ldots,a_n}_{i_1,\ldots,i_n} |{}^{a_1,\ldots,a_n}_{i_1,\ldots,i_n}\rangle \equiv t^{\mathbf{a}}_{\mathbf{i}} |{}^{\mathbf{a}}_{\mathbf{i}}\rangle. \tag{1.32}$$

It will also be convenient to use multi-index notation for arguments of functions *e.g.*

$$f(\boldsymbol{\mu}) \equiv f(\mu_1, \mu_2, \ldots, \mu_n). \tag{1.33}$$

The given notation holds for arbitrary dimension n of the multi-index. If a specific n has to be denoted explicitly this will be done by $\mathbf{i}_n$. A specific n-fold excited determinant can for example be written as $|{}^{\mathbf{a}_n}_{\mathbf{i}_n}\rangle$. Usually this notation will be used in combination with the sum convention *e.g.*

$$\hat{\mathcal{T}}|0\rangle = \sum_n \hat{\mathcal{T}}_n|0\rangle = t^{\mathbf{a}_n}_{\mathbf{i}_n} |{}^{\mathbf{a}_n}_{\mathbf{i}_n}\rangle. \tag{1.34}$$

Whether the sum convention is used or not is again always clear from the context.

2 Multiresolution Analysis

In this section, a framework for systematic construction of orthonormal $L^2\left(\Omega^N\right)$ bases called multiresolution analysis (MRA) is introduced. The domains Ω^N are finite hypercubes constructed from a one-dimensional real interval. The spatial parts of the molecular orbitals are for example approximated on the finite cube Ω^3. Without loss of generality, the domain Ω can be set to the unit interval.

A good starting point to construct systematic bases on $L^2\left(\Omega\right)$ are polynomials where in this work the Legendre polynomials $P_k\left(x\right)$ will be used. They can be constructed by the Rodriguez formula[34]

$$P_k\left(x\right) = \frac{(-1)^k}{2^k\,k!}\frac{\mathrm{d}^k}{\mathrm{d}x^k}\left[\left(1-x^2\right)^k\right], \quad k \in \mathbb{N}. \tag{2.1}$$

Legendre Polynomials which are orthonormal on the unit interval can be constructed by rescaling and shifting the original polynomials

$$\tilde{P}_k\left(x\right) = \sqrt{2k+1}P_k\left(2x-1\right). \tag{2.2}$$

In Fig. 2.1 the Legendre polynomials $\tilde{P}_k\left(x\right)$ up to $k = 4$ are plotted and in Fig. 2.2 an explicit example is given where a combination of two exponential functions is approximated with polynomials of increasing order. The function in the example shows typical features of molecular orbitals like cusps and asymptotic exponential decay. Globally defined polynomials on the other hand neither decrease towards the boundary nor have cusps leading to slow convergence when representing a function like the one given in Fig. 2.2. Asymptotic exponential decay of the function can only be represented by destructive interference of the polynomials resulting in high-frequency oscillations at the boundaries. A representation by piecewise defined polynomials is superior since the boundary intervals and the cusps could be represented independently. Consider a splitting of the domain in Fig. 2.2 into four domains of equal size

$$[0,1] = \left[0,\frac{1}{4}\right] \cup \left[\frac{1}{4},\frac{1}{2}\right] \cup \left[\frac{1}{2},\frac{3}{4}\right] \cup \left[\frac{3}{4},1\right], \tag{2.3}$$

and a basis of piecewise polynomials supported on those four subdomains. In such a basis the exponentially decreasing tails and the cusps of the function from Fig. 2.2 can be represented independently. For the representation of the cusps a further subdivision of the inner domains would increase the accuracy in this region further. MRA offers a way to systematically construct such bases.
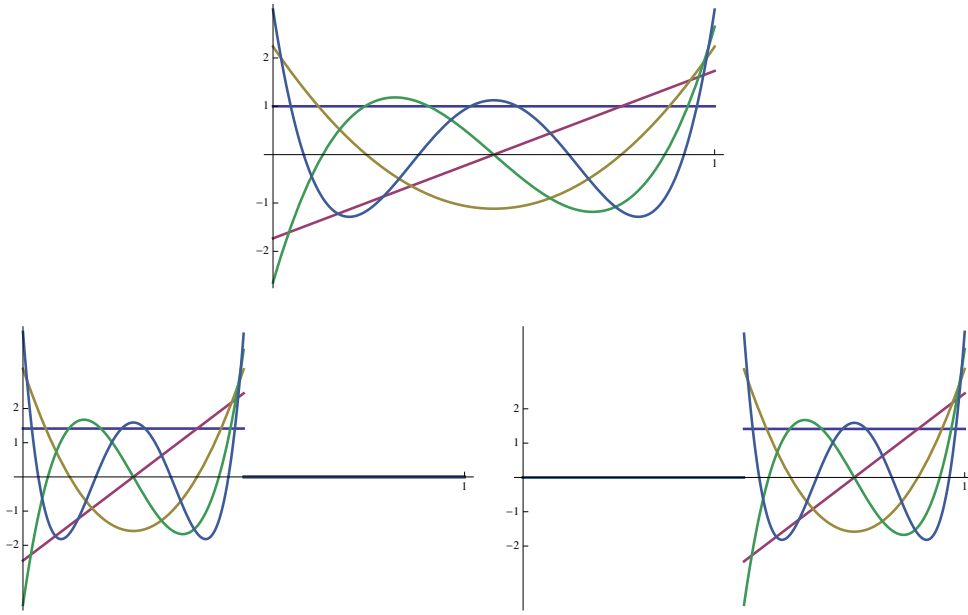
Figure 2.1: Scaling functions of the parent space V_0 (top), as well as the shifted and scaled scaling functions which span V_1^0 (bottom left) and V_1^1 (bottom right). The scaling functions are the shifted and scaled Legendre polynomials $\tilde{P}_k(x)$ (shown for $k = 0, \ldots, k = 4$)

In the following sections the basic ideas of MRA are introduced. A general introduction to MRA and related concepts can be found in Ref. 35. Further detailed information about MRA as it is introduced in this work can be found for example in Refs. 5, 36–38.

2.1 One-Dimensional Functions

Following Alpert *et al.*[38] a multiresolution analysis of $L^2(\Omega)$ is a telescoping series of subspaces V_n

$$V_0 \subset V_1 \subset \cdots \subset V_n \subset \cdots \subset L^2(\Omega), \tag{2.4}$$

where the union of those spaces V_n is dense in $L^2(\Omega)$. The parameter n is referred to as length scale and the functions which span V_0 are called scaling functions and are for this work the first k Legendre polynomials of Eq. (2.2)

$$\varphi_i(x) = \begin{cases} \tilde{P}_i(x), x \in \Omega \\ 0, \text{ else} \end{cases} \quad i = 0, \ldots, k-1. \tag{2.5}$$

The spaces V_n can be decomposed into direct sums

$$V_n = \bigoplus_{l=0}^{2^n-1} V_n^l, \tag{2.6}$$
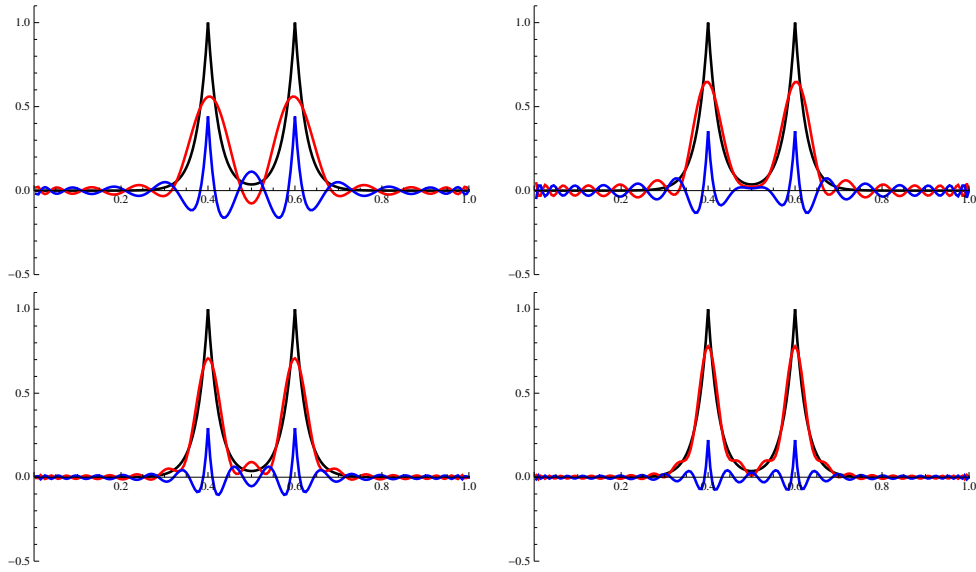
Figure 2.2: Function representation with global polynomials: The function $f(x) = e^{-\alpha(x-\beta)} + e^{-\alpha(x-\gamma)}$ (in black, with $\alpha = 40, \beta = 0.4, \gamma = 0.6$) approximated by the shifted and rescaled Legendre polynomials (in red) and the difference (in blue) where the first 20 (top left), 30 (top right), 40 (bottom left) and 50 (bottom right) polynomials are used to approximate $f(x)$.
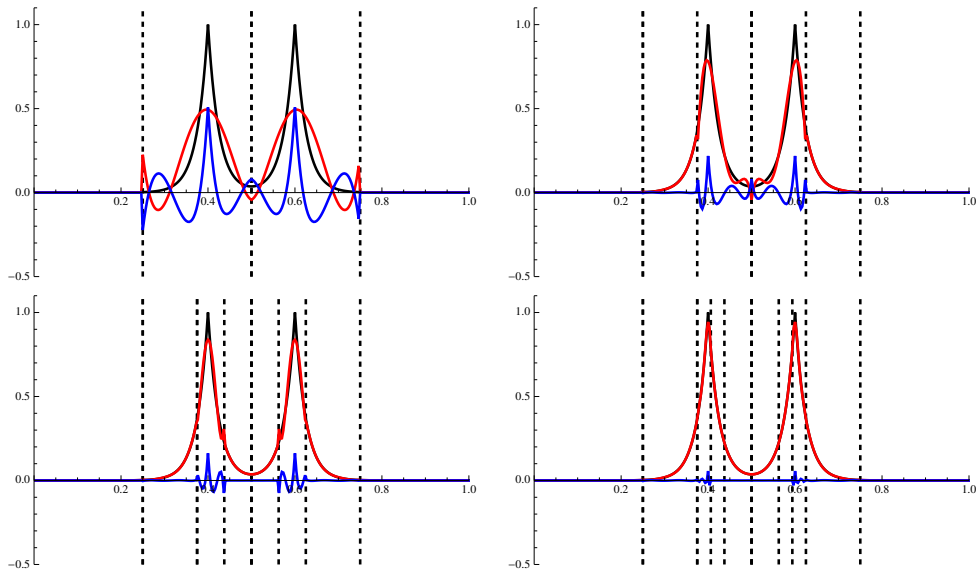
Figure 2.3: Function representation with MRA: The function $f(x) = e^{-\alpha(x-\beta)} + e^{-\alpha(x-\gamma)}$ (in black, with $\alpha = 40, \beta = 0.4, \gamma = 0.6$) approximated by a multiresolution analysis of the first 5 normalized Legendre polynomials (in red). The difference is plotted in blue and the dashed lines indicate the subdivision scheme.

and the spaces V_n^l are spanned by the translated and dilated basis functions of V_0 *i.e.*

$$V_0 = \text{span}\{\boldsymbol{\varphi}(x)\} \quad \leftrightarrow \quad V_n^l = \text{span}\{\boldsymbol{\varphi}_n^l(x) = 2^{\frac{n}{2}}\boldsymbol{\varphi}(2^n x - l)\}, \tag{2.7}$$

where a vector notation was introduced in order to keep the notation readable

$$\boldsymbol{\varphi}_n^l \equiv \left(\varphi_{n0}^l, \dots, \varphi_{nk-1}^l\right)^{\mathsf{T}}. \tag{2.8}$$

The support of the V_n^l functions are the dyadic intervals Ω_n^l which are constructed by dividing the original domain Ω into 2^n equal sized subdomains (see again Eq. (2.3)). The resolution on the domain Ω which is approximated by the "parent"[a] scaling functions of V_0 can be increased by its "children" V_1^0 and V_1^1. This procedure can be repeated to locally increase the resolution on the domains Ω_1^0 and Ω_1^1 of V_1^0 or V_1^1. In Fig. 2.1 this is illustrated for the spaces V_1^0 and V_1^1 which originate from V_0.

To estimate the error between child and parent spaces so called wavelet spaces are introduced. The wavelet spaces W_n^l are defined as the orthogonal complement between the child and parent spaces. Consider for example the space V_0 and the scaling space on the next length scale $V_1 = V_1^0 \oplus V_1^1$. Since $V_0 \subset V_1$ the k functions that span V_0 can be represented by linear combinations of the $2k$ functions which span V_1. In order to span the whole space V_1 with the functions of V_0, k additional functions are needed. The k orthonormal functions which fulfil this requirement are called wavelets and are part of the wavelet space W_0 defined by

$$V_0 \oplus W_0 = V_1^0 \oplus V_1^1, \tag{2.9}$$

or in general

$$V_n^l \oplus W_n^l = V_{n+1}^{2l} \oplus V_{n+1}^{2l+1}. \tag{2.10}$$

Like the scaling spaces, the wavelet spaces W_n^l are spanned by the rescaled and translated wavelets of W_0

$$W_0 = \text{span}\{\boldsymbol{\psi}(x)\} \quad \leftrightarrow \quad W_n^l = \text{span}\{\boldsymbol{\psi}_n^l(x) = 2^{\frac{n}{2}}\boldsymbol{\psi}(2^n x - l)\}. \tag{2.11}$$

By recursive application of Eq. (2.10) one gets for an arbitrary V_n

$$V_n = V_0 \bigoplus_{m=0}^{n-1} W_m = V_0 \bigoplus_{m=0}^{n-1} \left(\bigoplus_{l=0}^{2^m-1} W_m^l \right), \tag{2.12}$$

where W_n is defined analogue to Eq.(2.6). The wavelets are not unique and can be constructed with additional requirements like additional vanishing moments. In MADNESS the so called Alpert wavelets[37] are used.

---

[a]Sometimes the scaling functions of V_0 are referred to as "father wavelets" in analogy to the functions of W_0 which are called "mother wavelets".
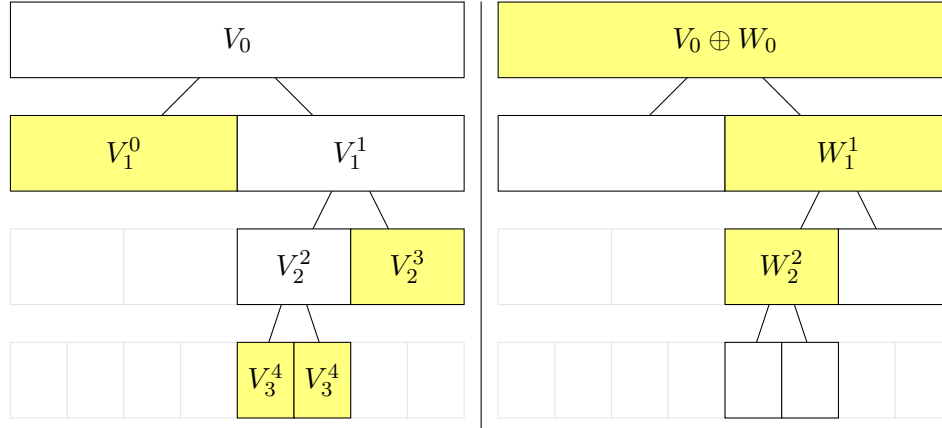
Figure 2.4: Adaptive tree structure in the reconstructed (left) and compressed (right) representation. The corresponding $L^2([0,1])$ function is approximated by the spaces in the coloured nodes.

The approximation of an arbitrary function on $L^2(\Omega)$ can be represented as a tree-structure with V_0 as root[a], and the V_n^l or W_n^l spaces as inner nodes and leafs. If the scaling spaces V_n^l are used, only the leaves of the tree contribute to the approximation and the tree is referred to as reconstructed tree. Alternatively the tree can be represented by the scaling functions and wavelets of the root, and the wavelets of all inner nodes. In this representation the leaves are empty and the tree is referred to as compressed tree. A schematic example for an adaptive tree in reconstructed and compressed representation is given in Fig. 2.4. The number of basis function in both representation is the same and both representations are orthonormal. Orthonormality of the reconstructed representation results from the non-overlapping support of the spaces which contribute to the representation. For the compressed representation the support of the basis functions can overlap and the orthonormality is assured by the orthonormality of the wavelet spaces between all scales.

The relation between the scaling functions and wavelets of parent and child nodes is given by the two-scale difference equations

$$\begin{pmatrix} \boldsymbol{\varphi}_n^l \\ \boldsymbol{\psi}_n^l \end{pmatrix} = \begin{pmatrix} \mathbf{H}^0 & \mathbf{H}^1 \\ \mathbf{G}^0 & \mathbf{G}^1 \end{pmatrix} \begin{pmatrix} \boldsymbol{\varphi}^{n+1,2l} \\ \boldsymbol{\varphi}^{n+1,2l+1} \end{pmatrix}, \tag{2.13}$$

with the $k \times k$ filter matrices $\mathbf{H}^0, \mathbf{H}^1, \mathbf{G}^0, \mathbf{G}^1$. Since the scaling functions are already given, the $\mathbf{H}$ filter matrices can be constructed straightforwardly. Once the wavelets ψ are determined, the $\mathbf{G}$ filter matrices can be constructed, and vice versa. Originally Alpert *et al.* constructed the wavelets explicitly and computed the $\mathbf{G}$ matrix from them.[37,38] Recently an alternative approach to construct the $\mathbf{G}$ matrices without explicit construction of the wavelets was published.[39] Note that the explicit analytical form of the wavelets is usually not needed

---

[a]Instead of choosing V_0 as root it is also possible to choose a different length scale n which leads to a tree structure with multiple roots.

Figure 2.5: A function with a sharp cusp at the origin (gray) evaluated at the Gauss-Legendre quadrature nodes (red points) for the length scales $n = 1$ (top left), $n = 2$ (top right), $n = 3$ (bottom left) and $n = 4$ (bottom right). Every refined interval contains 4 quadrature points (*i.e.* $k = 4$). Up to $n = 2$ the cusp at the origin is undersampled.
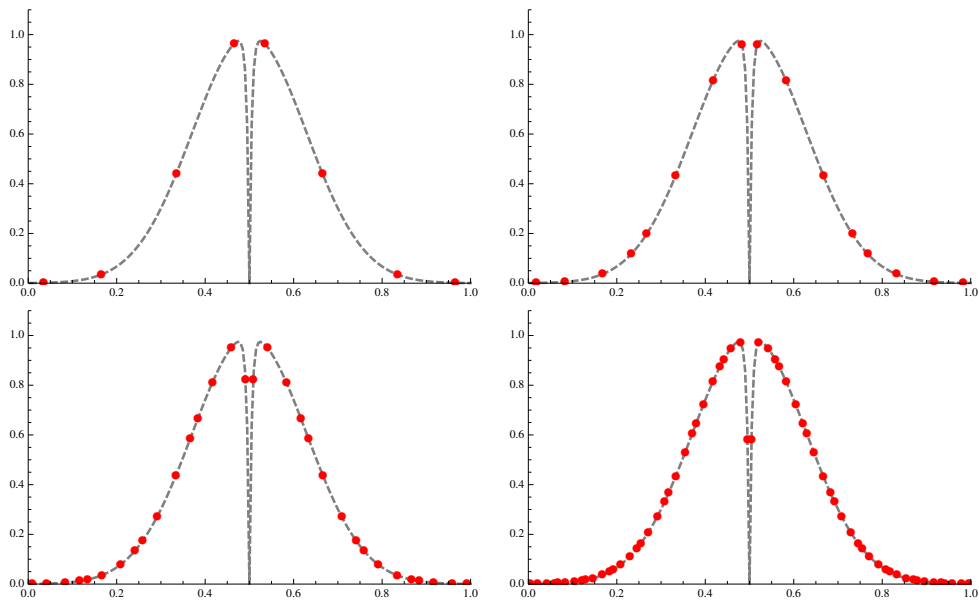
since function evaluation and projection can be done in the reconstructed representation.

For the representation of functions (and later operators) it is convenient to introduce the projectors onto the scaling and wavelet spaces

$$\hat{\mathrm{P}}_n^l : L^2(\Omega) \to V_n^l, \tag{2.14}$$

$$\hat{\mathrm{Q}}_n^l : L^2(\Omega) \to W_n^l. \tag{2.15}$$

From the definition of the wavelet spaces (2.10) it follows for the projectors

$$\hat{\mathrm{P}}_n^l + \hat{\mathrm{Q}}_n^l = \left(\hat{\mathrm{P}}_{n+1}^{2l} + \hat{\mathrm{P}}_{n+1}^{2l+1} \right), \tag{2.16}$$

and the corresponding projectors onto V_n and W_n follow from Eq. (2.6)

$$\hat{\mathrm{P}}_n = \sum_{l=0}^{2^n-1} \hat{\mathrm{P}}_n^l, \quad \hat{\mathrm{Q}}_n = \sum_{l=0}^{2^n-1} \hat{\mathrm{Q}}_n^l. \tag{2.17}$$

With those projectors, the compressed representation of a function is given by

$$\begin{aligned}
|f\rangle &= \hat{\mathrm{P}}_0|f\rangle + \sum_n \hat{\mathrm{Q}}_n|f\rangle \\
&= \mathbf{s}_0^0|\boldsymbol{\varphi}_0^0\rangle + \mathbf{d}_n^l|\boldsymbol{\psi}_n^l\rangle,
\end{aligned} \tag{2.18}$$

with the notation $\mathbf{s}|\boldsymbol{\varphi}\rangle \equiv s_i|\varphi_i\rangle$ for the sum of coefficients and functions. The scaling and wavelet coefficients are computed as $\mathbf{s}_n^l = \langle\boldsymbol{\varphi}_n^l|f\rangle$ and $\mathbf{d}_n^l = \langle\boldsymbol{\psi}_n^l|f\rangle$, and an adaptive representation is constructed by truncating small wavelet coefficients in this expansion. In Fig. 2.3 the function from the preceding chapter (see Fig. 2.2) is adaptively represented with multiresolution analysis leading to strong refinement in the vicinity of the cusps and lower refinement at the borders. In order to compare the two examples, the total number of basis functions was chosen to be equal for each plot of Figs. 2.3 and 2.2. The representation with MRA clearly shows better convergence with increasing number of basis functions. Also the undesired oscillations observed in Fig. 2.3 are not present any more.

In the MADNESS code, the multiresolution representation for a given function is constructed by leveling down the tree from the root or an arbitrary initial length scale (usually set to two). Between the refinement levels the wavelet coefficients are computed by the two-scale relations (2.13) and their norm is used as a criterium for further refinement. The wavelet coefficients of a given node are computed from the scaling coefficients of its children while the scaling coefficients are computed via projection of the original function. For the projection, the Gauss-Legendre quadrature is applied. With this procedure it can happen that the function of interest is undersampled (see Fig. 2.5 for an illustration) especially at domains where the function changes fast or is not smooth. To avoid undersampling, local refinement around specific domains or points can be enforced. For the example in Fig. 2.5, it is sufficient to

enforce local refinement up to the third length scale on all domains which include the origin
. Multi-dimensional functions with cusps, like for example

$$\frac{1 - e^{-\|\mathbf{x}-\mathbf{y}\|}}{\|\mathbf{x} - \mathbf{y}\|}, \tag{2.19}$$

occur in regularized potentials of electronic structure theory. [15,40] Here the refinement up to
a given resolution is enforced at all domains close to the diagonal ($\|\mathbf{x} - \mathbf{y}\| = 0$).

2.2 Multi-Dimensional Functions

Locally refined bases for higher dimensional domains Ω^d can be constructed with tensor
products of the scaling spaces on Ω

$$V_n^{l_1,l_2,\dots,l_d} = \bigotimes_{i=1}^{d} V_n^{l_i} \tag{2.20}$$

resulting in spaces whose functions are supported on dyadic hypercubes. The corresponding
wavelet spaces are constructed from all combinations of one-dimensional wavelet and scaling
spaces of a given length scale

$$W_n^{l_1,l_2,\dots,l_d} = \bigotimes_{i=1}^{d} \left(V_n^{l_i} \oplus W_n^{l_i} \right) \ominus V_n^{l_1,l_2,\cdots,l_d}. \tag{2.21}$$

For the two dimensional case the corresponding spaces are for example given by

$$V_n^{l_1,l_2} = V_n^{l_1} \otimes V_n^{l_2} \tag{2.22}$$

$$W_n^{l_1,l_2} = \left(V_n^{l_1} \otimes W_n^{l_2} \right) \oplus \left(W_n^{l_1} \otimes V_n^{l_2} \right) \oplus \left(W_n^{l_1} \otimes W_n^{l_2} \right). \tag{2.23}$$

The wavelet and scaling spaces adopt a similar tree structure to the one-dimensional case
where the number of children of each node is 2^d. The number of basis functions needed for
the compressed and reconstructed representations stays the same, regardless of the dimension
d. In Fig. 2.6 an example for the tree structure of a two dimensional domain is given. If k
Legendre functions are used the individual scaling spaces $V_n^{l_1,l_2}$ are spanned by k^2 functions
and the wavelet spaces $W_n^{l_1,l_2}$ by $3 \cdot k^2$ functions (see Eq. (2.22) and Eq. (2.23)). In the
particular example in Fig. 2.6, both representations are spanned by $10 \cdot k^2$ functions.

For high dimensional domains, the coefficients which expand a given function in a multires-
olution basis are d-fold indexed quantities

$$c_{k_1,k_2,\dots,k_d}, \quad \forall i \; k_i = 0, \dots, k-1, \tag{2.24}$$

where $k - 1$ denotes the highest polynomial order of the multiresolution analysis. The size
of each coefficient tensor increases exponentially with the dimension, which is known as the
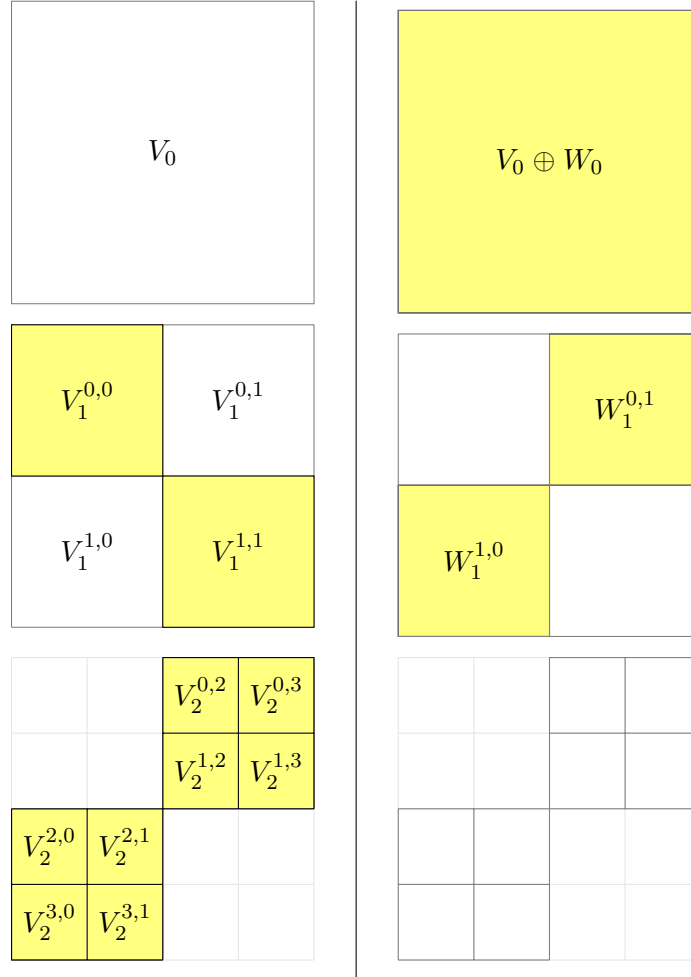
Figure 2.6: Reconstructed (left) and compressed (right) tree structure of an $L^2\left(\Omega^2\right)$ function. The function is represented by the spaces in the coloured nodes. Note that the wavelet spaces contain three times more functions than the scaling spaces (see Eq. (2.23)) so that the overall number of functions which contribute the the two representation is the same.

curse of dimensionality.[41] For $d > 3$ it is crucial to use low rank tensor formats like the singular value decomposition (SVD) to reduce the number of coefficients.[18,42] For $d = 3$ and lower the use of low-rank formats is possible but the savings in memory are not as significant.[42] The implementation in this work uses SVD format for $d = 6$ and full tensors for $d = 3$ similar to Ref. [18].

The construction of multidimensional functions which was introduced here can also be used to construct operators. This is called the non-standard form of operators[43,44] which will be introduced in the next section.[a]

2.3 Operators

This section gives a short introduction about the multiresolution representation of operators in non-standard form[43] which is related to the representation of functions introduced in the last section. The operators of interest act on $L^2(\Omega)$ functions and also give back $L^2(\Omega)$ functions, *i.e.*

$$\hat{O} : L^2(\Omega) \to L^2(\Omega), \quad \hat{O}|f\rangle = |g\rangle, \ f, g \in L^2(\Omega). \tag{2.25}$$

Using the projectors of Eq. (2.17) an operator in non-standard form is represented as

$$\begin{aligned}
\hat{O} &= \hat{P}_0\hat{O}\hat{P}_0 + \left(\hat{P}_n\hat{O}\hat{Q}_n + \hat{Q}_n\hat{O}\hat{P}_n + \hat{Q}_n\hat{O}\hat{Q}_n\right) \\
&= \hat{T}_0 + \sum_n \left(\hat{C}_n + \hat{B}_n + \hat{A}_n\right),
\end{aligned} \tag{2.26}$$

where each of the four introduced operators $\hat{T}_n, \hat{A}_n, \hat{B}_n, \hat{C}_n$ can be decomposed into $\hat{A}_n = \sum_{l,l'} \hat{A}_n^{ll'}$ according to Eq. (2.17). If applied to a function f the operator $\hat{O}$ in non-standard form acts on wavelet and scaling coefficients on all length scales and the resulting function $\tilde{f}$ is also represented with scaling and wavelet functions of all length scales

$$\begin{aligned}
|\tilde{f}\rangle = \hat{O}|f\rangle &= \hat{P}_0\hat{O}\hat{P}_0|f\rangle + \left(\hat{P}_n\hat{O}\hat{Q}_n|f\rangle + \hat{Q}_n\hat{O}\hat{P}_n|f\rangle + \hat{Q}_n\hat{O}\hat{Q}_n|f\rangle\right) \\
&= \tilde{s}_n^l|\varphi_n^l\rangle + \tilde{d}_n^l|\psi_n^l\rangle.
\end{aligned} \tag{2.27}$$

The coefficients of the resulting function $\tilde{f}$ are determined as

$$\tilde{\mathbf{s}}_0^0 = \mathbf{T}_0^0\mathbf{s}_0^0 + \mathbf{C}_0^0\mathbf{d}_0^0, \tag{2.28}$$

$$\tilde{\mathbf{s}}_n^l = \mathbf{C}_n^{ll'}\mathbf{d}_n^{l'}, \quad n > 0, \tag{2.29}$$

$$\tilde{\mathbf{d}}_n^l = \mathbf{B}_n^{ll'}\mathbf{s}_n^{l'} + \mathbf{A}_n^{ll'}\mathbf{d}_n^{l'}, \quad n \geq 0, \tag{2.30}$$

---

[a]The representation for multidimensional functions introduced here could also be referred to as non-standard representation of functions. In the standard representation, the wavelet spaces are constructed by simple tensor products over all length scales which leads to mixed length scales between dimensions, and basis functions which are supported on rectangles instead of squares. As a consequence, local refinement is not possible for the standard form.

with the matrices

$$\mathbf{T}_n^{ll'} = \langle \boldsymbol{\varphi}_n^l | \hat{\mathrm{O}} | \boldsymbol{\varphi}_n^{l'} \rangle, \quad \mathbf{A}_n^{ll'} = \langle \boldsymbol{\psi}_n^l | \hat{\mathrm{O}} | \boldsymbol{\psi}_n^{l'} \rangle, \tag{2.31}$$

$$\mathbf{B}_n^{ll'} = \langle \boldsymbol{\psi}_n^l | \hat{\mathrm{O}} | \boldsymbol{\varphi}_n^{l'} \rangle, \quad \mathbf{C}_n^{ll'} = \langle \boldsymbol{\varphi}_n^l | \hat{\mathrm{O}} | \boldsymbol{\psi}_n^{l'} \rangle. \tag{2.32}$$

In order to provide wavelet and scaling coefficients on all length scales, the function f, on which the operator is applied, is transformed into a redundant form. This redundant form is sometimes also called non-standard form of the function tree.[a] In Fig. 2.7 the application of an operator in non-standard form on a function in redundant representation is illustrated. The resulting function tree is in a mixed representation meaning the function is represented by scaling functions and wavelets on all levels but is not redundant. In a post-processing step, the result tree is transformed into reconstructed representation.

Multiresolution operators in non-standard form have a similar structure to the two dimensional functions from the preceding section. The connection can be illustrated by considering an integral operator

$$\hat{\mathrm{O}} f(x) = \int \mathrm{d}x' K(x, x') f(x'). \tag{2.33}$$

The kernel $K(x, x')$ can be represented as a two-dimensional function tree shown in Fig. 2.6 and the elements of the tree will be the same as for the non-standard operator. The main difference is that the operators are not constructed adaptively to a given precision but are constructed on demand when acting on an adaptive function tree (see Fig. 2.8). Convolution operators (*i.e.* $K(x, x') = K(x - x')$) which decay with increasing distance from the diagonal are represented with banded matrices making the application efficient. In Fig. 2.8 the application of a banded operator on refinement level 4 is shown. The banded structure of the operator reduces the matrices which have to be constructed significantly and also results in a already locally refined result tree. Since the input tree is also locally refined the number of matrices which have to be constructed decreases further.

Convolution operators on higher dimensional functions can be applied efficiently if separated representations can be constructed.[45] For the convolution with the Coulomb potential, and the BSH Green's function, which are used in electronic structure theory, this is possible.[5] In MADNESS the separated form of the convolution operators is represented by a sum of Gaussians.[5,30]

---

[a]For multidimensional function trees this might lead to confusion since the term non-standard could also be referring to the construction of the multidimensional wavelet bases (see Sec. 2.2).
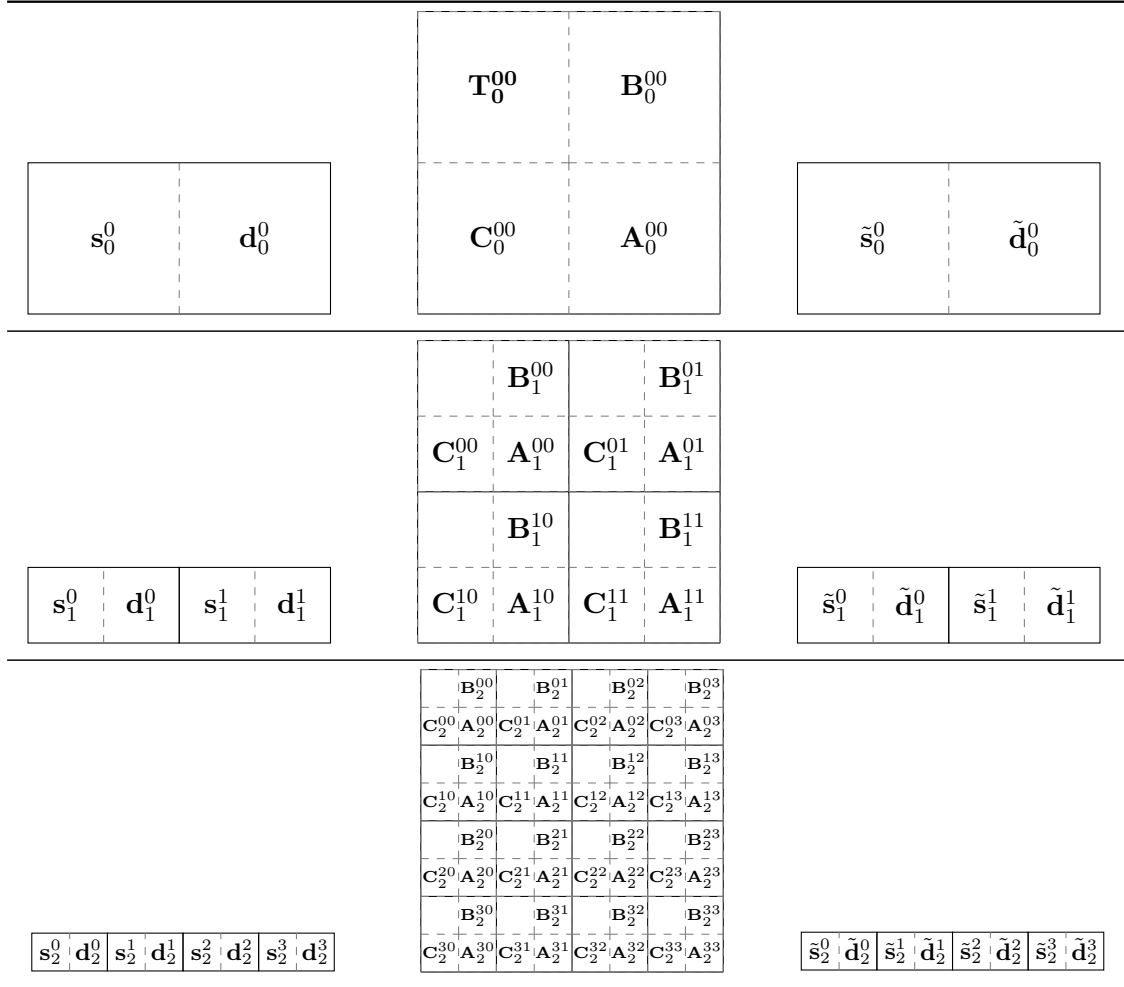
Figure 2.7: Non-standard form of an operator (middle) applied to a function tree in redundant form (left) on length scales $n = 0$, $n = 1$, and $n = 2$ with the resulting function tree in mixed representation (right). The Figure illustrates Eq. (2.28),(2.29) and (2.30) where in order to keep the tree structure similar to the previous figures the equations are represented in transposed form.
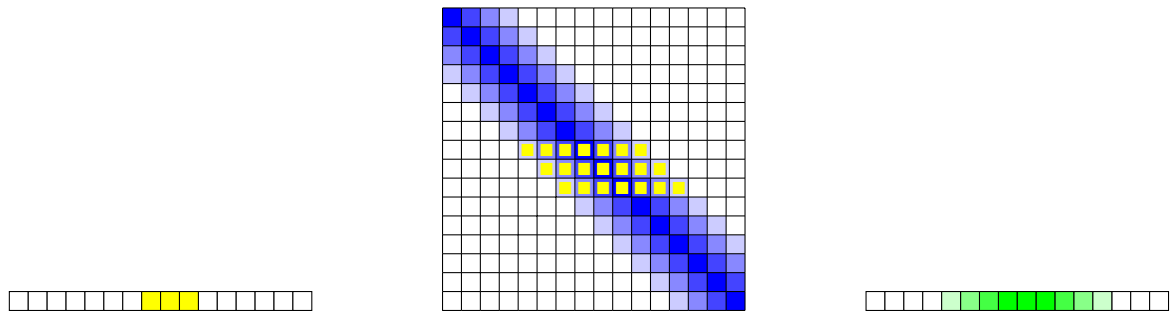
Figure 2.8: A banded operator applied to an adaptive tree on length scale $n = 4$. The blue boxes indicate the banded structure of the operator with entries above a given accuracy. The green (respectively yellow) boxes indicate non-zero entries of the adaptive output (respectively input) trees. Only the yellow marked operator boxes act on the non zero entries of the adaptive input tree.

3 Real-Space Coupled-Cluster: Ground State

The real-space solution scheme to the Hartree-Fock equations given in Eq. (1.27) is restricted to bound states (*i.e.* negative eigenvalues) and is usually used to compute only the occupied Hartree-Fock orbitals. Although some systems also have bounded virtual orbitals the vast majority of them is unbounded. Unbounded virtuals could in principle also be computed with Eq. (1.27) (either by introduction of a constant energy shift in the potential or by applying the Green's operator for unbounded states[46]), but due to their unbounded nature, the virtual orbitals become less and less confined making them hard to converge on finite domains and also a bad choice to construct a basis for bounded multi-electron states.[a] Since only a finite number of virtuals can be calculated, the resulting truncation in the one-electron basis leads to an uncontrolled error in the multi-electron basis which is also not desirable in an MRA approach. The coupled-cluster equations will therefore be reformulated in a basis-set independent way similar to Refs. [47] and [48] which derived real-space equations for closed-shell CCSD. Coupled-cluster theory based on occupied and virtual orbitals can be represented very elegantly with second-quantized creation and annihilation operators and their diagrammatic interpretation.[49] It is shown that the real-space formalism introduced here can be formulated in the same diagrammatic language with only minor modifications.

3.1 First-Quantized Formalism

The Schrödinger equation for the coupled-cluster wavefunction is

$$\hat{H}|CC\rangle = E_{CC}|CC\rangle, \quad |CC\rangle = e^{\hat{\mathcal{T}}}|0\rangle. \tag{3.1}$$

Since the coupled-cluster energy is a sum of the reference energy E_0 and the coupled-cluster correlation energy E_{corr}, it is convenient to rearrange Eq. (3.1) to

$$\mathcal{H}|0\rangle = E_{corr}|0\rangle, \tag{3.2}$$

with the similarity transformed, non-hermitian Hamiltonian

$$\mathcal{H} = e^{-\hat{\mathcal{T}}}\left(\hat{H} - E_0\right)e^{\hat{\mathcal{T}}}. \tag{3.3}$$

The correlation energy can then be obtained by projecting the transformed Schrödinger equation onto the reference

$$\langle 0|\mathcal{H}|0\rangle = E_{corr}. \tag{3.4}$$

---

[a]In fixed basis-set approaches, the chosen basis-set puts a constraint on the virtuals so that the unbounded nature of the true virtual orbitals is not an issue here.

Similarly, the projection onto excited determinants results in equations which determine the coupled-cluster amplitudes $t_{\mathbf{i}}^{\mathbf{a}}$

$$\Omega_{\mathbf{i}}^{\mathbf{a}} \equiv \langle_{\mathbf{i}}^{\mathbf{a}}|\mathcal{H}|0\rangle = 0. \tag{3.5}$$

To avoid the usage of virtual orbitals, the cluster operators in real-space formalism excite electrons from the reference determinant into correlated n-electron functions

$$\hat{\mathcal{T}}_n|0\rangle = |_{i_1,\ldots,i_n}^{\tau_{i_1,\ldots,i_n}}\rangle \equiv |_{\mathbf{i}_n}^{\tau_{\mathbf{i}_n}}\rangle \equiv |_{\mathbf{i}}^{\tau_{\mathbf{i}}}\rangle, \quad \tau_{\mathbf{i}_n} \in \mathcal{L}_n^2. \tag{3.6}$$

The functions τ are called n-body cluster functions[48] and are purely virtual

$$\boldsymbol{Q}_n|\tau_{\mathbf{i}}\rangle = |\tau_{\mathbf{i}}\rangle, \quad \boldsymbol{Q}_n \equiv \bigotimes_{i=1}^{n}\boldsymbol{Q} = \boldsymbol{Q}\otimes\boldsymbol{Q}\otimes\ldots, \tag{3.7}$$

and antisymmetric with respect to permutations of the electrons or in the multi-index $\mathbf{i}^{\mathbf{a}}$. Comparison of Eq. (3.6) with Eq. (1.24) gives the relation of the Cluster functions to the virtual spin orbitals

$$|\tau_{\mathbf{i}}\rangle = t_{\mathbf{i}}^{\mathbf{a}}|\mathbf{a}\rangle, \quad |\mathbf{a}\rangle \equiv \bigotimes_{m=1}^{n}|a_m\rangle. \tag{3.8}$$

where the coupled-cluster amplitudes are the expansion coefficients of the cluster functions in the virtual tensor-product basis

$$t_{\mathbf{i}}^{\mathbf{a}} = \langle\mathbf{a}|\tau_{\mathbf{i}}\rangle. \tag{3.9}$$

Equations (3.8) and (3.9) provide a simple scheme to switch from the amplitude to the real-space formalism. The cluster functions can be determined from Eq. (3.5) as

$$|\Omega_{\mathbf{i}}\rangle \equiv \Omega_{\mathbf{i}}^{\mathbf{a}}|\mathbf{a}\rangle = 0. \tag{3.10}$$

If the amplitude equations (3.5) are known explicitly, the real-space equations (3.10) can be determined by the following steps:[1]

1. Multiply the amplitude equations (3.5) by tensor products of virtuals according to Eq. (3.10).

2. Replace all amplitudes by the inner products given in Eq (3.9).

3. Do the summation over all virtuals and identify $\boldsymbol{Q}_n$ projectors given by Eq. (3.7) and (1.21).

4. If possible, use Eq. (3.7) to absorb the $\boldsymbol{Q}_n$ projectors into the cluster functions to simplify the expression.

The real-space equations can also be determined directly (see for example Ref. 48). Compared to diagrammatic approaches, this derivation is rather tedious so that it is not explicitly repeated here. A framework to derive the real-space equations directly via diagrammatic techniques is introduced in the next section.

---

[a]Note that in Ref. 48 the cluster functions are given for the closed-shell case and only for the spatial domain which will be treated in Sec. 5.1.

3.2 Second-Quantized and Diagrammatic Formalism

The equations of coupled-cluster and other many-body theories can be described in an elegant way by expressing the multi-electron states in terms of operators (second-quantized representation) and their diagrammatic interpretation. In Sec. 3.2.1 the formalism for fixed basis-set approaches like LCAO is briefly introduced; a detailed introduction into second-quantized and diagrammatic approaches in the context of non-relativistic many-body physics can be found in Ref. 49. In Sec. 3.2.2 the necessary changes for a real-space description are made. Explicit expressions for the individual terms of the coupled-cluster equations in real-space are not given in this section but in Ch. 5 where the implementation of closed-shell CC2 is described. The notation as well as the used conventions mainly follow Ref. 49.

3.2.1 Fixed Basis-Set

Instead of Slater determinants many-particle states can also be expressed as string of creation (and annihilation) operators $\hat{a}_p^\dagger$ ($\hat{a}_p$) which act on a vacuum state; here denoted as $|\rangle$. The operator $\hat{a}_p^\dagger$ (or $\hat{a}_p$) creates (or annihilates) particles in specific one-particle states χ_p which are usually the occupied and virtual orbitals of the reference system. An arbitrary n-electron state expressed by a single Slater determinant can then be expressed as a string of creation operators acting on the vacuum state

$$\hat{a}_{p_1}^\dagger \hat{a}_{p_2}^\dagger \ldots \hat{a}_{p_n}^\dagger |\rangle. \tag{3.11}$$

The last equation is equivalent to a Slater determinant constructed from the spin-orbitals $\chi_{p_1}, \chi_{p_2}, \ldots, \chi_{p_n}$. Antisymmetry of the many-particle state is ensured by the anti-commutation relations

$$\left[\hat{a}_p^\dagger, \hat{a}_q^\dagger\right]_+ = 0, \tag{3.12}$$

$$\left[\hat{a}_p, \hat{a}_q\right]_+ = 0, \tag{3.13}$$

$$\left[\hat{a}_p^\dagger, \hat{a}_q\right]_+ = \delta_{pq}. \tag{3.14}$$

In the particle-hole formalism the vacuum state is denoted as $|0\rangle$ and is defined to be the many-particle state build up from all occupied reference orbitals (*i.e.* the reference determinant)

$$|0\rangle \equiv \prod_i \hat{a}_i^\dagger |\rangle. \tag{3.15}$$

The vacuum state $|0\rangle$ of the particle-hole formalism is also called Fermi vacuum. The creation (and annihilation) operators of occupied and virtual states act differently on the Fermi

vacuum[a]

$$\hat{a}_i^\dagger|0\rangle = 0, \qquad\qquad\qquad \hat{a}_i|0\rangle = |_i\rangle, \qquad\qquad (3.16)$$

$$\hat{a}_a^\dagger|0\rangle = |^a\rangle, \qquad\qquad\qquad \hat{a}_a|0\rangle = 0, \qquad\qquad (3.17)$$

where the $|_i\rangle$ (respectively $|^a\rangle$) state denotes an $(N_e - 1)$-electron state (or respectively an $(N_e + 1)$-electron state).[b] The action of $\hat{a}_i$ on the Fermi vacuum can be interpreted as the creation of a hole while $\hat{a}_a^\dagger$ still creates particles in the usual sense. Virtual states of the reference are therefore referred to as particle states, and occupied reference states as hole states. In Fig. 3.1 a schematic overview over second quantization and the corresponding antisymmetric many-particle spaces is given.

Operators in the second-quantized form are represented as strings of creation and annihilation operators weighted by matrix elements of the operator with the corresponding one-electron states. It is convenient to express operators in normal ordered form meaning that creation and annihilation operators are ordered such that the expectation value with the vacuum vanishes. In the particle-hole formalism this means that hole-creation operators $\hat{a}_i^\dagger$ and particle-annihilation operators $\hat{a}_a$ have to be on the right of the operator string. General one-electron and two-electron operators in normal-order are, with respect to the particle-hole vacuum, expressed as[49]

$$\hat{F}_N = \langle p|\hat{f}|q\rangle\{\hat{a}_p^\dagger\hat{a}_q\}, \qquad\qquad (3.18)$$

$$\hat{G}_N = \frac{1}{4}\langle pq||rs\rangle\{\hat{a}_p^\dagger\hat{a}_q^\dagger\hat{a}_s\hat{a}_r\}, \qquad\qquad (3.19)$$

with the antisymmetrized two electron integrals

$$\langle pq||rs\rangle = \langle pq|\hat{g}_{12}|rs\rangle - \langle pq|\hat{g}_{12}|sr\rangle. \qquad\qquad (3.20)$$

The curly brackets denote the normal-product of an operator string defined as

$$\{\text{operator string}\} \equiv (-1)^{\sigma(\hat{P})}\,(\text{normal ordered operator string})\,, \qquad (3.21)$$

where $\sigma(\hat{P})$ denotes the number of individual transpositions in the permutation operator $\hat{P}$ which creates the normal ordered operator string from the initial operator string; take for example

$$\{\hat{a}_i^\dagger\hat{a}_j\} = -\hat{a}_j\hat{a}_i^\dagger, \qquad\qquad (3.22)$$

$$\{\hat{a}_a\hat{a}_b^\dagger\} = -\hat{a}_b^\dagger\hat{a}_a, \qquad\qquad (3.23)$$

$$\{\hat{a}_a^\dagger\hat{a}_i\} = -\hat{a}_i\hat{a}_a^\dagger, \qquad\qquad (3.24)$$

$$\{\hat{a}_i^\dagger\hat{a}_j^\dagger\hat{a}_a\hat{a}_b\} = \hat{a}_i^\dagger\hat{a}_j^\dagger\hat{a}_a\hat{a}_b = -\hat{a}_i^\dagger\hat{a}_j^\dagger\hat{a}_b\hat{a}_a = \ldots, \qquad (3.25)$$

$$\{\hat{a}_a^\dagger\hat{a}_b^\dagger\hat{a}_i\hat{a}_j\} = \hat{a}_i\hat{a}_j\hat{a}_a^\dagger\hat{a}_b^\dagger = -\hat{a}_j\hat{a}_i\hat{a}_a^\dagger\hat{a}_b^\dagger = \ldots. \qquad (3.26)$$

---

[a]Since in the Fermi vacuum all orbitals from the reference determinant are occupied the application of a further creation operator results in the zero vector. This follows from the anti-commutation relation of the operators. Since the common notation $|0\rangle$ is used here for the reference determinant/Fermi vacuum the zero-vector is just denoted as 0.

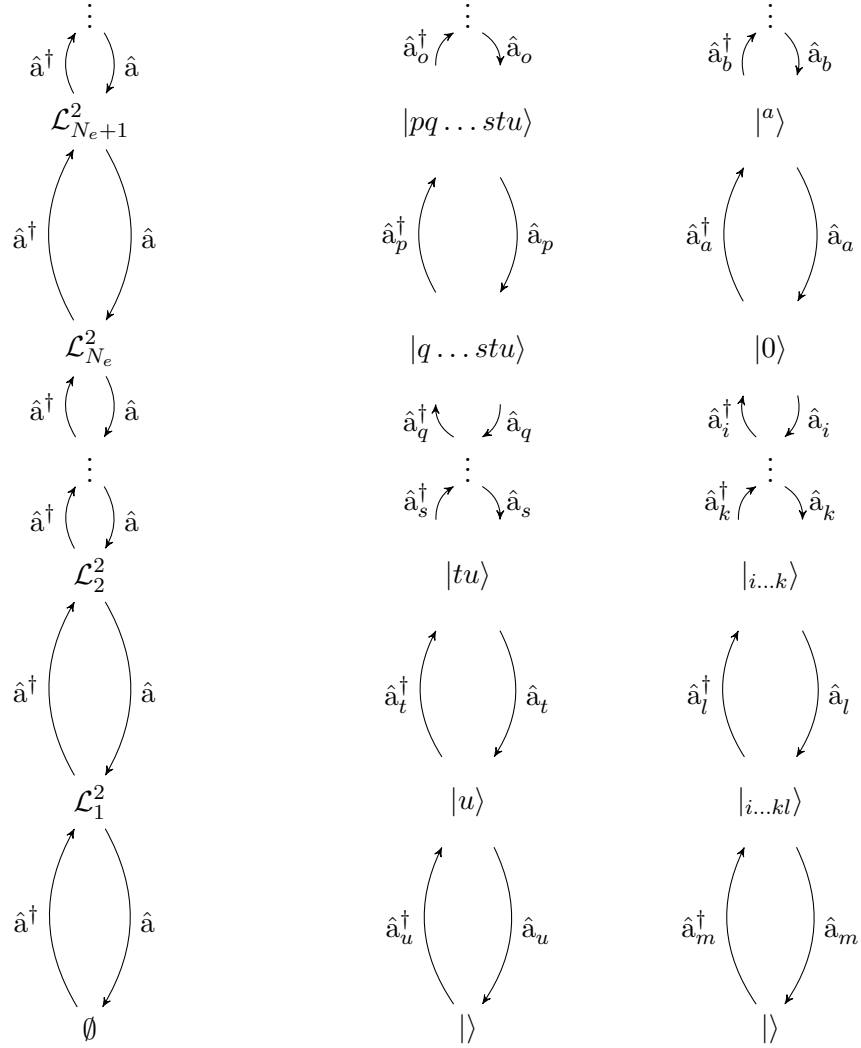[b]Let N_e denote the number of electrons present in the reference state $|0\rangle$.

Figure 3.1: Connection of the second-quantized creation and annihilation operators with the corresponding antisymmetric many-particle spaces (left) and illustrative examples of the formulation with the physical vacuum (middle) and the Fermi vacuum of the particle-hole formulation (right).

A general one-electron operator from Eq. (3.18) can be graphically represented as a vertex with three lines

$$\hat{F}_N = \quad \hat{f}\cdots\diagup^{a}_{b} \quad + \quad \hat{f}\cdots\diagdown^{j}_{i} \quad + \quad \hat{f}\cdots\diagdown^{i}\diagup^{a} \quad + \quad \hat{f}\cdots\diagup_{a}\diagdown_{i} \; . \tag{3.27}$$

The dashed line represents the operator itself while the in and outgoing lines represent particle and hole states. To distinguish particle and hole lines they are given directions indicated by small arrowheads. Upgoing lines are interpreted as particles and downgoing lines as holes. Open lines which enter (leave) the operator vertex are interpreted as annihilators (creators). The matrix element of the operator is also obtained from the in and outgoing lines via $\langle \text{out}|\hat{f}|\text{in}\rangle$. This leads to the following algebraic interpretation of the diagrams of Eq.(3.27)

$$\hat{f}\cdots\diagup^{a}_{b} \equiv \langle a|\hat{f}|b\rangle\{\hat{a}_a^{\dagger}\hat{a}_b\}, \quad \hat{f}\cdots\diagdown^{j}_{i} \equiv \langle i|\hat{f}|j\rangle\{\hat{a}_i^{\dagger}\hat{a}_j\}, \tag{3.28}$$

$$\hat{f}\cdots\diagdown^{i}\diagup^{a} \equiv \langle a|\hat{f}|i\rangle\{\hat{a}_a^{\dagger}\hat{a}_i\}, \quad \hat{f}\cdots\diagup_{a}\diagdown_{i} \equiv \langle i|\hat{f}|a\rangle\{\hat{a}_i^{\dagger}\hat{a}_a\}. \tag{3.29}$$

The diagrammatic representation of the normal-ordered two-electron operator is similar with two vertices connected by the operator line. The matrix elements are then obtained via $\langle \text{left out,right out}||\text{left in, right in}\rangle$. Similar the string of operators is interpreted as $\{\hat{a}_{\text{left out}}^{\dagger}\hat{a}_{\text{right out}}^{\dagger}\hat{a}_{\text{right in}}\hat{a}_{\text{left in}}\}$ One of the diagrams of the normal ordered two-electron operator is for example

$$\diagup^{a}_{b}\rightsquigarrow\diagdown^{i}_{j} \equiv \langle aj||bi\rangle\{\hat{a}_a^{\dagger}\hat{a}_j^{\dagger}\hat{a}_i\hat{a}_b\}. \tag{3.30}$$

In this example, the factor $\frac{1}{4}$ from Eq. (3.19) is not present. This is a result of grouping diagrams with proportional algebraic interpretation together and assigning them weight factors. In the given example there are actually four algebraically equivalent diagrams

$$\diagup^{a}_{b}\rightsquigarrow\diagdown^{i}_{j} \equiv \diagup^{a}_{b}\rightsquigarrow\diagdown^{i}_{j} + \diagdown^{i}_{j}\rightsquigarrow\diagup^{a}_{b} + \diagdown^{i}\diagup^{a}\rightsquigarrow\diagup_{b}\diagdown_{j} + \diagup_{b}\diagdown_{j}\rightsquigarrow\diagdown^{i}\diagup^{a} \; , \tag{3.31}$$

and instead of taking all four diagrams into account only one of them is chosen with the factor of one instead of $\frac{1}{4}$ (the left hand side of Eq. (3.31) is interpreted with weight factor one, while all diagrams on the right hand side would get the factor of $\frac{1}{4}$). In general the weight factors can be deduced by the topological structure of the corresponding diagrams. For the real-space interpretation of diagrams the weight factors will not change and are therefore not discussed further in this work. Detailed information can be found in Ref. 49. In Ch. 5 the rules to assign weight factors for closed-shell coupled-cluster diagrams are given explicitly (see Fig. 5.1).

The n-body cluster operators are diagrammatically represented as

$$\hat{\mathcal{T}}_1 \equiv \overset{a \quad i}{\diagup\!\!\diagup} = t_i^a \{\hat{a}_a^\dagger \hat{a}_i\}, \tag{3.32}$$

$$\hat{\mathcal{T}}_2 \equiv \overset{a \quad i \quad b \quad j}{\diagup\!\!\diagup \quad \diagup\!\!\diagup} = \frac{1}{4} t_{ij}^{ab} \{\hat{a}_a^\dagger \hat{a}_i \hat{a}_b^\dagger \hat{a}_j\}, \tag{3.33}$$

$$\hat{\mathcal{T}}_n \equiv \overset{a_1 \ i_1 \ a_2 \ i_2 \quad a_n \ i_n}{\diagup\!\!\diagup \ \diagup\!\!\diagup \ \cdots\cdots \ \diagup\!\!\diagup} = \frac{1}{(n!)^2} t_{\mathbf{i}}^{\mathbf{a}} \{\hat{a}_{a_1}^\dagger \hat{a}_{i_1} \ldots \hat{a}_{a_n}^\dagger \hat{a}_{i_n}\}. \tag{3.34}$$

Vacuum expectation values over products of operators can be evaluated by Wick's theorem and the so called Wick contractions.[a] In diagrammatic representation this results in a simple contraction scheme were only lines of the same type are contracted. The result is then the sum of all possible contractions which leads to closed diagrams (*i.e.* the diagram has no open lines). Closed diagrams are fully contracted meaning no creation or annihilation operator shows up in their interpretation.

In second quantized form the coupled-cluster Hamiltonian from Eq. (3.3) reads

$$\mathcal{H} = e^{-\hat{\mathcal{T}}} \hat{H}_N e^{\hat{\mathcal{T}}}. \tag{3.35}$$

Applying the Baker-Campbell-Hausdorff expansion in combination with Wick's theorem results in the connected form of the Hamiltonian[49,52]

$$\mathcal{H} = \left(\hat{H}_N e^{\hat{\mathcal{T}}} \right)_C, \tag{3.36}$$

---

[a]The original work of Wick[50] was formulated for electrons and positrons in the context of quantum electrodynamics. An introduction in the context of quantum chemistry can be found in Ref. 49 or Ref. 51.

meaning that the diagrammatic representation will only contain connected diagrams. The coupled-cluster equations in connected form are then given by

$$\langle 0| \hat{H}_N e^{\hat{\mathcal{T}}} |0\rangle_C = E_{\text{corr}}, \tag{3.37}$$

$$\langle^{\mathbf{a}}_{\mathbf{i}}| \hat{H}_N e^{\hat{\mathcal{T}}} |0\rangle_C = \Omega^{\mathbf{a}}_{\mathbf{i}} = 0. \tag{3.38}$$

Diagrams which represent the n-body amplitude equations are often not drawn as closed diagrams but with n pairs of open particle and hole lines which are labelled by the entries of $\mathbf{a}$ and $\mathbf{i}$. In other words, one could say that the $\langle^{\mathbf{a}}_{\mathbf{i}}|$ part is neglected in the diagrammatic representation. Usually the explicit labelling is also omitted. In this work both conventions will be used. A simple example for the two conventions is

$$\langle^{ab}_{ij}| \hat{G}_N |0\rangle_C = \quad {}^i \! \bigcirc a \; j \bigcirc b \quad \equiv \quad \bigvee\!\!\!\bigvee \quad = \langle ab||ij\rangle. \tag{3.39}$$

Because of the used conventions the diagram given in the last equation is identical to one of the diagrams representing the two-electron operator but the interpretation is different since it results only in the matrix element. It is always clear from the context what kind of diagram is represented.

3.2.2 Adaptive Real-Space Formalism

The real-space formalism presented here uses the formal eigenstates of the position operator as a formal basis. Following Ref. 53 a possible $L^2(\Omega)$ eigenfunction of the position operator could be constructed as

$$f_{\mathbf{r}'}(\mathbf{r}) = \begin{cases} c, & \mathbf{r} = \mathbf{r}' \\ 0, & \text{else}, \end{cases} \tag{3.40}$$

with an arbitrary constant c. Since the functions $f_{\mathbf{r}'}$ vanish everywhere except a for single point, their $L^2(\Omega)$-norm is zero which makes them equivalent to the $L^2(\Omega)$ zero-function and therefore not suitable as basis. Instead the eigendistributions of the position operator are used which are the Dirac delta distributions $\delta(\mathbf{r} - \mathbf{r}')$ defined as formal convolutions

$$f(\mathbf{r}) = \int d\mathbf{r}' \delta(\mathbf{r} - \mathbf{r}') f(\mathbf{r}'). \tag{3.41}$$

Although Eq. (3.41) is written as a formal integral there is no $L^2(\Omega)$ function which satisfies the definition. It is however possible to represent the delta distribution as a limit of convolutions with ordinary $L^2(\Omega)$ functions[23,34]

$$f(\mathbf{r}) = \lim_{n\to\infty} \int d\mathbf{r}' g_n(\mathbf{r} - \mathbf{r}') f(\mathbf{r}'), \tag{3.42}$$

where one typical example for g_n is a Gaussian convolution

$$g_n(\mathbf{r}) = \frac{n}{\pi} e^{-n^2 \mathbf{r}^2}. \tag{3.43}$$

Functions on which distributions like the delta distribution act, are usually restricted to the space of test functions which are smooth on the whole domain. [23] The n-cluster functions are certainly not test functions since they have cusps at the electron-electron and electron-nuclei coalescence points (see Sec. 5.2.3). In the end, the functions will be represented with MRA and finite resolution so that instead of taking the limit $n \to \infty$ in Eq. (3.42) an arbitrary large $n < \infty$ can be chosen such that the width of the Gaussian g_n is smaller than the finest used MRA length scale. With arbitrary small width Eq. (3.42) is a Gaussian convolution defined for all $L^2(\Omega)$ functions. The usage of delta distributions in the following should therefore be viewed as a formal scheme to arrive at the coupled-cluster real-space equations suitable for numerical applications with finite precision.

In the real-space formulation the formal excitation into virtual spin-position eigenstates is considered. The spin-position eigenstates are constructed from the corresponding spin and position eigenstates which are denoted as

$$|\mu\rangle = |\mathbf{r}_\mu\rangle \otimes |s_\mu\rangle, \quad \mathbf{r}_\mu \in \mathbb{R}^3, s_\mu \in \{\pm\frac{1}{2}\}. \tag{3.44}$$

The position eigenstates form a continuous set resulting in a real-space representation by delta distributions

$$\langle\mu|\nu\rangle = \delta(\mu - \nu) = \delta(\mathbf{r}_\mu - \mathbf{r}_\nu)\,\delta_{s_\mu s_\nu} \tag{3.45}$$

Virtual spin-position eigenstates are formally obtained by applying the $\boldsymbol{Q}$ projector

$$|v_\mu\rangle \equiv \boldsymbol{Q}|\mu\rangle. \tag{3.46}$$

The particle-creation (and particle-annihilation) operators $\hat{a}_a^\dagger$ (and $\hat{a}_a$) are now replaced by $\hat{a}^\dagger(\mu)$ (and $\hat{a}(\mu)$) which create (and annihilate) particles in $|v_\mu\rangle$. In order to keep the resulting many-particle states anti-symmetric, the new set of commutators needs to fulfil similar anticommutation relations

$$\left[\hat{a}^\dagger(\mu), \hat{a}(\nu)\right]_+ = \delta(\mu - \nu), \tag{3.47}$$

$$\left[\hat{a}^\dagger(\mu), \hat{a}^\dagger(\nu)\right]_+ = 0, \tag{3.48}$$

$$\left[\hat{a}(\mu), \hat{a}(\nu)\right]_+ = 0, \tag{3.49}$$

while the anticommutators of the hole-creation and hole-annihilation operators stay the same, and the mixed anticommutators vanish. From the definition of the $|v_\mu\rangle$ states, a relation between the $\hat{a}_a^\dagger$ and $\hat{a}_\mu^\dagger$ operators can be deduced as

$$\hat{a}^\dagger(\mu) = \chi_a(\mu)\,\hat{a}_a^\dagger \tag{3.50}$$

or correspondingly

$$\hat{a}_a^\dagger = \int d\mu\,\chi_a^*(\mu)\,\hat{a}^\dagger(\mu). \tag{3.51}$$

With those relations, the anticommutation relations given above follow directly from the anticommutation relations in Eqs. (3.13), (3.12) and (3.14). This approach creates (and annihilates) particles at specific points in real-space similar to the first approaches by Fock[54] and Jordan[55] (see also Ref. [56]) while the description of the hole states remains unchanged.

With the new set of operators one arrives at similar normal ordered operators and corresponding diagrammatic interpretation where the indices of the virtual spin-orbitals $a, b, \ldots$ are replaced with the continuous spin-position index $\mu, \nu, \ldots$. Since the new set of indices is a continuous set, summations become integrations and matrix elements depending on the new set of indices become functions.

As an example the two-body cluster operator is given

$$\text{(diagram)} = \hat{\mathcal{T}}_2 = \frac{1}{4} \int \mathrm{d}\mu \int \mathrm{d}\nu \sum_{ij} \mathbf{Q}_{12} \tau_{ij}(\mu, \nu) \{\hat{\mathrm{a}}^\dagger(\mu)\,\hat{\mathrm{a}}_i \hat{\mathrm{a}}^\dagger(\nu)\,\hat{\mathrm{a}}_j\}. \tag{3.52}$$

Due to the $\mathbf{Q}_{12}$ projector the τ_{ij} function can be restricted to the virtual space (as in the first-quantized formalism in section 3.1). With the explicit expression for the $\mathbf{Q}$ projectors in terms of virtual orbitals, Eq. (1.21), and the relation between the creation (and annihilation) operators in Eq. (3.51), the $\hat{\mathcal{T}}_2$ operator can be expressed as

$$\begin{aligned}
\hat{\mathcal{T}}_2 &= \frac{1}{4} \int \mathrm{d}\mu \int \mathrm{d}\nu \sum_{ij} \mathbf{Q}_{12} \tau_{ij}(\mu, \nu) \{\hat{\mathrm{a}}^\dagger(\mu)\,\hat{\mathrm{a}}_i \hat{\mathrm{a}}^\dagger(\nu)\,\hat{\mathrm{a}}_j\} \\
&= \frac{1}{4} \int \mathrm{d}\mu \int \mathrm{d}\nu \sum_{ijab} \chi_a(\mu)\,\chi_b(\nu)\,\langle ab|\tau_{ij}\rangle \{\hat{\mathrm{a}}^\dagger(\mu)\,\hat{\mathrm{a}}_i \hat{\mathrm{a}}^\dagger(\nu)\,\hat{\mathrm{a}}_j\} \\
&= \frac{1}{4} \sum_{ijab} \langle ab|\tau_{ij}\rangle \{\hat{\mathrm{a}}_a^\dagger \hat{\mathrm{a}}_i \hat{\mathrm{a}}_b^\dagger \hat{\mathrm{a}}_j\}.
\end{aligned} \tag{3.53}$$

Through comparison of Eq. (3.53) with Eq. (3.33), the amplitudes can be indentified as

$$t_{ij}^{ab} = \langle ab|\tau_{ij}\rangle, \tag{3.54}$$

so that the τ_{ij} functions are identical to the ones from the first-quantized formalism; the same holds true for a general n-body operator which is in this formalism

$$\text{(diagram)} \equiv \hat{\mathcal{T}}_n = \frac{1}{n!^2} \int \mathrm{d}\boldsymbol{\mu}\, \mathbf{Q}_n \tau_{\mathbf{i}}(\boldsymbol{\mu})\,\hat{\boldsymbol{\mu}}_{\mathbf{i}}, \tag{3.55}$$

with the n-body excitation operator abbreviated as

$$\hat{\boldsymbol{\mu}}_{\mathbf{i}} \equiv \{\prod_{m=1}^{n} \hat{\mathrm{a}}^\dagger(\mu_m)\,\hat{\mathrm{a}}_{i_m}\}. \tag{3.56}$$

The multi-indices are denoted similar as before with the usual notation for multiple integrals

$$\int d\boldsymbol{\mu} \equiv \int d\mu_1 \cdots \int d\mu_n, \tag{3.57}$$

$$\tau_{\mathbf{i}}(\boldsymbol{\mu}) \equiv \tau_{i_1,\ldots,i_n}(\mu_1,\ldots,\mu_n). \tag{3.58}$$

In this notation the electron number n of the n-body operators is not denoted explicitly, so that for example $\tau_{\mathbf{i}}(\boldsymbol{\mu})$ could stand for any of the n-body cluster functions. In some cases it will be useful to explicitly include n into the notation. A specific n-body cluster function (or other quantities) is then denoted as $\tau_{\mathbf{i}_n}(\boldsymbol{\mu})$. The whole cluster operator can then for example be written as

$$\hat{\mathcal{T}} = \sum_n \hat{\mathcal{T}}_n = \int d\boldsymbol{\mu}\, \boldsymbol{Q}_n \tau_{\mathbf{i}_n}(\boldsymbol{\mu})\, \hat{\boldsymbol{\mu}}_{\mathbf{i}_n} \tag{3.59}$$

where the sum convention also holds for the n label. Note, that in this work $\mathbf{i}$ and $\boldsymbol{\mu}$ always have the same number of entries (*i.e.* $\tau_{\mathbf{i}_n}(\boldsymbol{\mu}) \equiv \tau_{\mathbf{i}}(\boldsymbol{\mu}_n) \equiv \tau_{\mathbf{i}_n}(\boldsymbol{\mu}_n)$).[a]

General one- and two-electron operators like in Eq. (3.18) and Eq. (3.19) are represented similar but with functions instead of matrix elements. Those functions can be derived from formal matrix elements, build with the formal virtual spin-position eigenstates $|v_\mu\rangle$. For a general one-electron operator $\hat{\mathrm{f}}$ the formal matrix elements are given by

$$\langle v_\mu | \hat{\mathrm{f}} | i \rangle \equiv \boldsymbol{Q}\hat{\mathrm{f}}(\mu)\, \chi_i(\mu), \tag{3.60}$$

$$\langle i | \hat{\mathrm{f}} | v_{\mu'} \rangle \equiv \boldsymbol{Q}\left(\hat{\mathrm{f}}(\mu')\, \chi_i(\mu')\right)^\dagger, \tag{3.61}$$

$$\langle v_\mu | \hat{\mathrm{f}} | v_{\mu'} \rangle \equiv \boldsymbol{Q}\hat{\mathrm{f}}(\mu)\, \boldsymbol{Q}\delta(\mu - \mu') \tag{3.62}$$

while matrix elements between hole states stay the same. The real-space interpretation of the four diagrams of the one-electron operator is then

$$\mathrm{f} - - - - \begin{array}{c} \uparrow \mu \\ \\ \uparrow \mu' \end{array} \equiv \int d\mu \int d\mu'\, \boldsymbol{Q}_n \hat{\mathrm{f}}(\mu)\, \delta(\mu - \mu')\, \{\hat{\mathrm{a}}^\dagger(\mu)\, \hat{\mathrm{a}}(\mu')\}, \tag{3.63}$$

$$\mathrm{f} - - - - \begin{array}{c} \downarrow i \\ \\ \downarrow j \end{array} \equiv \langle i | \hat{\mathrm{f}} | j \rangle \{\hat{\mathrm{a}}_i^\dagger \hat{\mathrm{a}}_j\}, \tag{3.64}$$

---

[a]For the description of processes which will not keep the number of particles constant (*e.g.* ionization) this would not necessarily be the case

$$\equiv \int \mathrm{d}\mu \, \boldsymbol{Q} \hat{\mathrm{f}}\left(\mu\right) \chi_i\left(\mu\right) \{\hat{\mathrm{a}}^\dagger\left(\mu\right) \hat{\mathrm{a}}_i\} \tag{3.65}$$

$$\equiv \int \mathrm{d}\mu' \left(\hat{\mathrm{f}}\left(\mu'\right) \chi_j\left(\mu'\right)\right)^\dagger \{\hat{\mathrm{a}}_j^\dagger \hat{\mathrm{a}}\left(\mu'\right)\}. \tag{3.66}$$

For the two-electron operator the formal matrix elements are derived from the diagrams as before and their functional interpretations are for example

$$\langle v_{\mu_1} v_{\mu_2} | g_{12} | v_{\mu'_1} v_{\mu'_2} \rangle \equiv \boldsymbol{Q}_{12} g_{12} \boldsymbol{Q}_{12} \, \delta\left(\mu_1 - \mu'_1\right) \delta\left(\mu_2 - \mu'_2\right) \tag{3.67}$$

$$\langle v_{\mu_1} v_{\mu_2} | g_{12} | ij \rangle \equiv \boldsymbol{Q}_{12} g_{12} \chi_i\left(\mu_1\right) \chi_j\left(\mu_2\right) \tag{3.68}$$

$$\langle v_{\mu_1} i | g_{12} | j v_{\mu'_2} \rangle \equiv \chi_i^*\left(\mu'_2\right) \boldsymbol{Q}_1 g_{12'} \chi_j\left(\mu_1\right) \boldsymbol{Q}_{2'}. \tag{3.69}$$

The commutation rules for the new set of virtual creation and annihilation operators lead to the exact same contraction patterns as the formulation with an explicit set of virtual orbitals. Real-space coupled-cluster equations in connected form can then be written as

$$\langle 0 | \hat{\mathrm{H}}_{\mathrm{N}} \, e^{\hat{\mathcal{T}}} | 0 \rangle_{\mathrm{C}} = E_{\mathrm{corr}} \tag{3.70}$$

$$\langle {}^{\boldsymbol{\mu}}_{\mathbf{i}} | \hat{\mathrm{H}}_{\mathrm{N}} \, e^{\hat{\mathcal{T}}} | 0 \rangle_{\mathrm{C}} = \Omega_{\mathbf{i}}\left(\boldsymbol{\mu}\right) = 0, \tag{3.71}$$

and the diagrams which represent those equations are structurally the same as for the fixed basis-set formulation. Only the interpretation rules have slightly changed:

1. Interpretation of hole lines stays the same.

2. Particle lines are labelled with the spin-position index μ and interpreted as formal virtual spin-position eigenstates $|v_\mu\rangle \equiv \boldsymbol{Q}|\mu\rangle$.

3. Summation over particle indices becomes integration over spin-position variables.

4. Former matrix elements with particle indices become functions.

In the interpretation of the real-space diagrams of the connected coupled-cluster equations (3.70) and (3.71), the delta distributions which occur in the formal matrix elements are, after integration, not present in the final expression. Take for example one of the diagrams from the

singles equations

$$
\begin{aligned}
\text{F} &\equiv \int \mathrm{d}\mu' \, \langle v_\mu | \hat{\mathrm{f}} | v_{\mu'} \rangle \tau_i \left(\mu' \right) \\
&\equiv \boldsymbol{Q} \int \mathrm{d}\mu' \, \hat{\mathrm{f}} \left(\mu' \right) \delta \left(\mu - \mu' \right) \tau_i \left(\mu' \right) \\
&= \boldsymbol{Q} \hat{\mathrm{f}} \left(\mu \right) \tau_i \left(\mu \right) \\
&\equiv \boldsymbol{Q} \hat{\mathrm{f}} | \tau_i \rangle
\end{aligned}
\tag{3.72}
$$

Another example is a diagram from the doubles equation (see also Eq.(3.67) for the formal matrix element)

$$
\begin{aligned}
&\equiv \int \mathrm{d}\mu_1' \int \mathrm{d}\mu_2' \, \langle v_{\mu_1} v_{\mu_2} || v_{\mu_1'} v_{\mu_2'} \rangle \tau_i \left(\mu_1' \right) \tau_j \left(\mu_2' \right) \\
&= \langle v_{\mu_1} v_{\mu_2} || \tau_j \left(\mu_1 \right) \tau_i \left(\mu_2 \right) \rangle \\
&\equiv \boldsymbol{Q}_{12} g_{12} \left(\tau_i \left(\mu_1 \right) \tau_j \left(\mu_2 \right) - \tau_i \left(\mu_2 \right) \tau_j \left(\mu_1 \right) \right) \\
&\equiv \boldsymbol{Q}_{12} g_{12} \left(1 - \hat{\mathrm{P}}_{12} \right) \left(| \tau_i \rangle \otimes | \tau_j \rangle \right).
\end{aligned}
\tag{3.73}
$$

4 Real-Space Coupled-Cluster: Linear Response

Molecular properties for excited states can be determined via linear response theory which is formulated in terms of a time-averaged quasienergy if the underlying model is solved variationally; for the case of non-variational models like the projected coupled-cluster equations, the time-averaged quasienergy is replaced by a time-averaged Lagrangian. First, a brief introduction following Ref. 57 is given. Second, the formalism for real-space coupled-cluster is derived and subsequently a general instruction (following the appendix of Ref. 2) to derive the working equations is given. Explicit working equations for the closed-shell CC2 model will not be given in this chapter but in Ch. 5. The notation in Sec. 4.1 follows Ref. 57 and will only be used inside this chapter.

4.1 Linear Response: Introduction

A time-dependent potential is introduced as external perturbation to the time-independent Hamiltonian of the physical system

$$\hat{H}(t) = \hat{H} + V(t),\tag{4.1}$$

where the time-dependent potential is assumed to be periodic with some period T, *i.e.*

$$V(t) = V(t+T).\tag{4.2}$$

The time-dependent potential can be expanded in a Fourier series in which the monochromatic potentials V^{ω_k} are expanded into a set of hermitian perturbation operators $\hat{X}$ weighted by the field strengths $\epsilon_{\hat{X}}(\omega_k)$

$$V(t) = e^{-i\omega_k t} V^{\omega_k},$$
$$= e^{-i\omega_k t} \epsilon_{\hat{X}}(\omega_k)\hat{X}, \quad \omega_k = k\frac{2\pi}{T}, \; k \in \mathbb{Z},\tag{4.3}$$

where the property for the frequencies follows from the periodicity of the potential.[a] The time-dependent perturbation $V(t)$ is required to be hermitian which implies

$$(V(t))^{\dagger} = V(t) \iff (V^{\omega_k})^{\dagger} = V^{-\omega_k} \iff \epsilon^*(\omega_k) = \epsilon(-\omega_k).\tag{4.4}$$

---

[a]Note that there is a sum over the frequencies ω_k as well as over the perturbation operators $\hat{X}$ and the corresponding field strengths. Note also that $\omega_{-k} = -\omega_k$.

4 Real-Space Coupled-Cluster: Linear Response

In the following, various quantities will be expanded into Fourier series and the corresponding Fourier components will be expanded in terms of the field strengths associated with the perturbation $V(t)$. The terms of the expansion are then grouped according to the order in the perturbation. For an arbitrary function $f(t)$ this expansion is given by

$$f(t) = f^{(0)} + f^{(1)}(t) + f^{(2)}(t) + \dots, \tag{4.5}$$

with the Fourier expansion for the time-dependent first and higher order

$$f^{(1)}(t) = f^{(1)}(\omega_k) e^{-i\omega_k t}, \tag{4.6}$$

$$f^{(2)}(t) = f^{(2)}(\omega_k, \omega_l) e^{-i(\omega_k + \omega_l)t} \tag{4.7}$$

$$\dots$$

and the Fourier components expanded in terms of the field strengths as

$$f^{(1)}(\omega_k) = \epsilon_{\hat{X}}(\omega_k) f^{\hat{X}}(\omega_k) \tag{4.8}$$

$$f^{(2)}(\omega_k, \omega_l) = \frac{1}{2} \epsilon_{\hat{X}}(\omega_k) \epsilon_{\hat{Y}}(\omega_l) f^{\hat{X}\hat{Y}}(\omega_k, \omega_l) \tag{4.9}$$

$$\dots$$

Note also, that the zeroth order term is always the corresponding time independent quantity. The time-dependent state $|\bar{0}(t)\rangle$ of the system is determined by the time-dependent Schrödinger equation (1.1) and can be written in a phase isolated form[58]

$$|\bar{0}(t)\rangle = e^{-iF(t)}|\tilde{0}(t)\rangle, \tag{4.10}$$

such that in the time-independent limit the solution $e^{-E_0 t}|0\rangle$ for stationary states is obtained. Consequently $F(t)$ goes to $E_0 t$ in the time-independent limit and the time-derivative of $F(t)$ is called a quasienergy which can be determined from the phase isolated time-dependent Schrödinger equation as

$$Q(t) \equiv \frac{\mathrm{d}F}{\mathrm{d}t} = \langle \tilde{0}(t) | \left(\hat{H}(t) - i\frac{\partial}{\partial t} \right) |\tilde{0}(t)\rangle. \tag{4.11}$$

Expectation values for arbitrary observables represented by hermitian operators can be formally expanded in terms of the field strengths of the perturbation

$$\langle \tilde{0}(t) | \hat{X} | \tilde{0}(t) \rangle = \langle 0|\hat{X}|0\rangle + e^{-i\omega_k t} \epsilon_{\hat{Y}}(\omega_k) \langle\langle \hat{X}; \hat{Y} \rangle\rangle_{\omega_k} + \dots. \tag{4.12}$$

The exansion is done similar to Eqs. (4.5)–(4.9) and the term $\langle\langle \hat{X}; \hat{Y} \rangle\rangle_{\omega_k}$ is called linear response function.

With the solutions to the time-independent Schrödinger equation $\hat{H}\Psi_i = E_i\Psi_i$ the linear response function can be written as [a]

$$\langle\langle \hat{X}; \hat{Y} \rangle\rangle_\omega = \frac{\langle 0|\hat{X}|i\rangle\langle i|\hat{Y}|0\rangle}{\omega - \omega_i} - \frac{\langle 0|\hat{Y}|i\rangle\langle i|\hat{X}|0\rangle}{\omega + \omega_i}, \quad \omega_i = E_i - E_0. \tag{4.13}$$

---

[a]See Ref. 57 for details and note that E_0 is the exact ground state energy of the system (not the Hartree-Fock energy).

The linear response function has poles for the excitation energies ω_i of the unperturbed system. In order to compute excitation energies for approximative models the poles of the corresponding response functions are investigated. The response functions are identified with derivatives of variational time-averaged quasienergies; in the case of non-variational wavefunctions, response functions are identified as derivatives of variational time-averaged Lagrangians.

With the time-average of a function defined as

$$\{f(t)\}_T = \frac{1}{T} \int_{-\frac{T}{2}}^{\frac{T}{2}} dt\, f(t) \tag{4.14}$$

the variational condition for the time-averaged quasienergy[59]

$$\delta\{Q(t)\}_T = 0 \tag{4.15}$$

leads to a Hellmann-Feynman theorem for the time-averaged quasienergy

$$\frac{d\{Q(t)\}_T}{d\epsilon_{\hat{X}}(\omega)} = \left\{ \langle \tilde{0}(t)| \frac{dV(t)}{d\epsilon_{\hat{X}}(\omega)} |\tilde{0}(t)\rangle \right\}_T . \tag{4.16}$$

If the variational condition (4.15) is fulfilled, the linear response function can be identified as second derivative with respect to the field strengths of the time-averaged second-order quasienergy

$$\langle\langle \hat{X}; \hat{Y}\rangle\rangle_\omega = \frac{d^2\{Q^{(2)}\}_T}{d\epsilon_{\hat{X}}(-\omega)\, d\epsilon_{\hat{Y}}(\omega)} . \tag{4.17}$$

This follows from Eq. (4.16) and the expansion of Eq. (4.12)[a]

$$
\begin{aligned}
\frac{d\{Q\}_T}{d\epsilon_{\hat{X}}(\omega)} &= \left\{ \langle \tilde{0}(t)| \hat{X} |\tilde{0}(t)\rangle e^{-i\omega t} \right\}_T \\
&= \left\{ \left(\langle 0|\hat{X}|0\rangle + e^{-i\omega_k t} \epsilon_{\hat{Y}}(\omega_k) \langle\langle \hat{X}; \hat{Y}\rangle\rangle_{\omega_k} + \dots \right) e^{-i\omega t} \right\}_T \\
&= \langle 0|\hat{X}|0\rangle \delta_{0,\omega} + \delta_{0,(\omega+\omega_k)} \epsilon_{\hat{Y}}(\omega_k) \langle\langle \hat{X}; \hat{Y}\rangle\rangle_{\omega_k} + \dots \\
&= \langle 0|\hat{X}|0\rangle \delta_{0,\omega} + \epsilon_{\hat{Y}}(-\omega) \langle\langle \hat{X}; \hat{Y}\rangle\rangle_{-\omega} + \dots .
\end{aligned}
\tag{4.18}
$$

Note that the $Q^{\hat{X}\hat{Y}}$ function[b] coincides with the linear response function if the variational condition (4.15) is fulfilled.

Assume that the time-dependent state $|\tilde{0}\rangle$ is parametrized by some time-dependent parameter λ which is usually a multi-indexed set of parameters or in the real-space case a multi-indexed

---

[a]Note that $\left\{ e^{-i\omega_k t} \right\}_T = \delta_{k,0}$ which follows from the condition in Eq. (4.3)

[b]$Q^{\hat{X}\hat{Y}}$ is obtained from the formal expansion of the quasienergy in terms of the field strengths (Eqs. (4.5)–(4.9) with f replaced by Q)

set of functions. To simplify the notation the parameter is in this section treated like a scalar quantity similar to Ref. 57. The parameters are also expanded according to Eq. (4.5)–(4.9) where the zeroth order parameters correspond to the time-independent ground state. With this expansion of the parameters and the quasienergy, the (total) second derivative of the second-order quasienergy can be expressed as[a]

$$
Q^{\hat{X}\hat{Y}}\left(-\omega,\omega\right) = \frac{\partial^2 \left\{Q^{(2)}\right\}_T}{\partial\epsilon_{\hat{X}}\left(-\omega\right)\partial\lambda^{(1)}\left(\omega\right)}\lambda^{\hat{Y}}\left(\omega\right) + \frac{\partial^2 \left\{Q^{(2)}\right\}_T}{\partial\lambda^{(1)}\left(-\omega\right)\partial\epsilon_{\hat{Y}}\left(\omega\right)}\lambda^{\hat{X}}\left(-\omega\right) \tag{4.19}
$$
$$
+ \frac{\partial^2 \left\{Q^{(2)}\right\}_T}{\partial\lambda^{(1)}\left(-\omega\right)\partial\lambda^{(1)}\left(\omega\right)}\lambda^{\hat{X}}\left(-\omega\right)\lambda^{\hat{Y}}\left(\omega\right) + \frac{\partial^2 \left\{Q^{(2)}\right\}_T}{\partial\lambda^{(2)}\left(-\omega,\omega\right)}\lambda^{\hat{X}\hat{Y}}\left(-\omega,\omega\right)
$$

Since the variational condition (4.15) for the quasienergy holds for variations in the state $|\tilde{0}\rangle$ it implies the same condition for $Q^{\hat{X}\hat{Y}}$ with respect to variation of the parameters of first and second-order

$$
\frac{\partial Q^{\hat{X}\hat{Y}}}{\partial\lambda^{\hat{X}}} = 0, \quad \frac{\partial Q^{\hat{X}\hat{Y}}}{\partial\lambda^{\hat{X}\hat{Y}}} = 0. \tag{4.20}
$$

The first equation determines the first-order parameters

$$
\frac{\partial Q^{\hat{X}\hat{Y}}}{\partial\lambda^{\hat{X}}} = \frac{\partial^2 \left\{Q^{(2)}\right\}_T}{\partial\lambda^{(1)}\left(-\omega\right)\partial\epsilon_{\hat{Y}}\left(\omega\right)} + \frac{\partial^2 \left\{Q^{(2)}\right\}_T}{\partial\lambda^{(1)}\left(-\omega\right)\partial\lambda^{(1)}\left(\omega\right)}\lambda^{\hat{Y}}\left(\omega\right)
$$
$$
\equiv \eta^{\hat{Y}}\left(\omega\right) + F\left(\omega\right)\lambda^{\hat{Y}}\left(\omega\right) = 0, \tag{4.21}
$$

so that the linear response function for variational models can in general be written as

$$
\langle\langle\hat{X};\hat{Y}\rangle\rangle_\omega = \frac{1}{2}\hat{C}^{\pm\omega}\left(1 + \hat{P}_{\hat{X}\hat{Y}}\hat{P}_{\omega,-\omega}\right)\left\{\left(\eta^{\hat{X}}\left(-\omega\right) + \frac{1}{2}\lambda^{\hat{X}}\left(-\omega\right)F\left(\omega\right)\right)\lambda^{\hat{Y}}\left(\omega\right)\right\}. \tag{4.22}
$$

Here the permutation operators and the operator $\hat{C}^{\pm\omega}$ ensure the symmetry $\langle\langle\hat{X};\hat{Y}\rangle\rangle_\omega = \langle\langle\hat{Y};\hat{X}\rangle\rangle_{-\omega} = \langle\langle\hat{X};\hat{Y}\rangle\rangle_{-\omega}^*$.[b]

For non-variational models like coupled-cluster with projected equations, a Lagrangian is used instead of the quasienergy. The Lagrangian is usually constructed from the quasienergy and the time-dependent equations $C\left(\lambda,t\right) = 0$ as

$$
L\left(t\right) = Q\left(\lambda,t\right) + \bar{\lambda}C\left(\lambda,t\right), \tag{4.23}
$$

---

[a]Note that the second partial derivative with respect to the field strengths vanishes since the only part of the quasienergy that depends explicitly on the field strengths is the time-dependent perturbation (4.3) which depends only linearly on the field strengths.

[b]The complex symmetrizer $\hat{C}^{\pm\omega}f\left(\omega\right) = f\left(\omega\right) + f^*\left(-\omega\right)$ is not necessary at this point but for non-variational models.

where the new set of Lagrange parameters $\bar{\lambda}$ was introduced. By requiring the time-averaged Lagrangian to be variational $\delta \{L\}_T = 0$ one receives equations to determine the parameters λ and $\bar{\lambda}$

$$\xi^{\hat{X}}(\omega) + A(\omega) \lambda^{\hat{X}}(\omega) = 0, \tag{4.24}$$

$$\bar{\lambda}^{\hat{X}}(\omega) A(-\omega) + \eta^{\hat{X}}(\omega) + F(\omega) \lambda^{\hat{X}}(\omega) = 0, \tag{4.25}$$

where the quantities F and η are defined as before with $\{L^{(2)}\}_T$ instead of $\{Q^{(2)}\}_T$ and

$$A(\omega) \equiv \frac{\partial^2 \{L^{(2)}\}_T}{\bar{\lambda}^{(1)}(-\omega) \lambda^{(1)}(\omega)}, \quad \xi^{\hat{Y}}(\omega) \equiv \frac{\partial^2 \{L^{(2)}\}_T}{\bar{\lambda}^{(1)}(-\omega) \epsilon_{\hat{Y}}(\omega)}. \tag{4.26}$$

The linear response function can be written in the same way as Eq. (4.22) or when Eq. (4.24) is inserted as

$$\langle\langle \hat{X}; \hat{Y} \rangle\rangle_\omega = -\frac{1}{2} \hat{C}^{\pm\omega} \left(1 + \hat{P}_{\hat{X}\hat{Y}} \hat{P}_{\omega,-\omega}\right) \left\{ \eta^{\hat{X}} \left(A^{-1}\xi^{\hat{Y}}\right) - \frac{1}{2} \left(A^{-1}\xi^{\hat{X}}\right) \left(FA^{-1}\xi^{\hat{Y}}\right) \right\}, \tag{4.27}$$

where the ω dependence was dropped for better readability.[a] The poles of the linear response function are determined by the inverse of $A(\pm\omega)$ which is in the general case the inverse of an operator. For coupled-cluster wavefunctions the inverse of the operator $A(\pm\omega)$ becomes the resolvent of the coupled-cluster Jacobian which is shown in the next section.

4.2 Linear Response: Coupled-Cluster

The coupled-cluster Lagrangian is given by

$$L(t) = Q(t) + \langle \bar{\tau}_{\mathbf{i}_n}(t) | C_{\mathbf{i}_n}(t) \rangle, \tag{4.28}$$

where the $\bar{\tau}_{\mathbf{i}_n}$ functions are the n-body Lagrange multipliers in real-space, $Q(t)$ is the coupled-cluster quasienergy, and $|C_{\mathbf{i}_n}(t)\rangle$ are the time-dependent coupled-cluster equations

$$Q(t) = \langle 0| \left(\hat{H}_N - i\frac{\partial}{\partial t}\right) e^{\hat{\mathcal{T}}(t)} |0\rangle, \tag{4.29}$$

$$C_{\mathbf{i}}(\boldsymbol{\mu}, t) \equiv \boldsymbol{Q}_{\boldsymbol{\mu}} \langle_{\mathbf{i}}^{\boldsymbol{\mu}} | e^{-\hat{\mathcal{T}}(t)} \left(\hat{H}_N - i\frac{\partial}{\partial t}\right) e^{\hat{\mathcal{T}}(t)} |0\rangle = 0. \tag{4.30}$$

The time-dependent cluster operators $\hat{\mathcal{T}}(t)$ are defined in the same way as the time-independent ones but with time-dependent cluster-functions $\tau_{\mathbf{i}}(t)$. With the Fourier expansion similar to Eq. (4.5)–(4.9) the second-order time-averaged Lagrangian becomes

$$\left\{L^{(2)}\right\}_T = \left\{Q^{(2)}\right\}_T + \langle \bar{\tau}_{\mathbf{i}}^{(1)} | \Omega_{\mathbf{i}}^{(1)} \rangle - \omega \langle \bar{\tau}_{\mathbf{i}}^{(1)} | \tau_{\mathbf{i}}^{(1)} \rangle, \tag{4.31}$$

---

[a]For η and ξ the sign of the ω argument is always opposite between the $\hat{X}$ and $\hat{Y}$ dependent terms. The ω dependence of F and A is indicated by bracketing, *i.e.* $\left(FA^{-1}\xi^{\hat{Y}}\right) = F(\omega) A^{-1}(\omega) \xi^{\hat{Y}}(\omega)$

$$\Omega_{\mathbf{i}}^{(1)}\left(\mu,\omega\right) = \boldsymbol{Q}_{\boldsymbol{\mu}}\langle_{\mathbf{i}}^{\boldsymbol{\mu}}|\,\hat{H}_{N}\,\hat{\mathcal{T}}^{(1)}\left(\omega\right)e^{\hat{\mathcal{T}}^{(0)}}|0\rangle_{C}. \tag{4.32}$$

The operator $A\left(\omega\right)$, defined in Eq. (4.26), becomes an integral operator

$$\left(\hat{A}\left(\omega\right)f\right)_{\mathbf{i}} = \int d\boldsymbol{\mu}' A_{\mathbf{ij}}\left(\boldsymbol{\mu},\boldsymbol{\mu}',\omega\right)f_{\mathbf{j}}\left(\boldsymbol{\mu}'\right), \tag{4.33}$$

with the kernel given by the functional derivatives of $\left\{L^{(2)}\right\}_{T}$ with respect to the cluster functions $\tau_{\mathbf{i}}$ and the Lagrangian multipliers $\bar{\tau}_{\mathbf{i}}$

$$A_{\mathbf{ij}}\left(\boldsymbol{\mu},\boldsymbol{\mu}',\omega\right) = \frac{\delta\left\{L^{(2)}\right\}_{T}}{\delta\tau_{\mathbf{j}}^{(1)}\left(\omega,\boldsymbol{\mu}'\right)\delta\bar{\tau}_{\mathbf{i}}^{(1)}\left(-\omega,\boldsymbol{\mu}\right)} = \frac{\delta\Omega_{\mathbf{i}}^{(1)}\left(\omega,\boldsymbol{\mu}\right)}{\delta\tau_{\mathbf{j}}^{(1)}\left(\omega,\boldsymbol{\mu}'\right)} - \omega\delta\left(\boldsymbol{\mu}'-\boldsymbol{\mu}\right)\delta_{\mathbf{i,j}}. \tag{4.34}$$

The first term on the right hand side of Eq. (4.34) is equivalent to the coupled-cluster Jacobian

$$\frac{\delta\Omega_{\mathbf{i}}^{(1)}\left(\omega,\boldsymbol{\mu}\right)}{\delta\tau_{\mathbf{j}}^{(1)}\left(\omega,\boldsymbol{\mu}'\right)} = \frac{\delta\Omega_{\mathbf{i}}\left(\boldsymbol{\mu}\right)}{\delta\tau_{\mathbf{j}}\left(\boldsymbol{\mu}'\right)}, \tag{4.35}$$

with the time-independent cluster functions $\tau_{\mathbf{i}} \equiv \tau_{\mathbf{i}}^{(0)}$ and the projected coupled-cluster equations $\Omega_{\mathbf{i}}$ of Eq. (3.71). The linear dependence on the first-order functions $\tau^{(1)}\left(\omega\right)$ of the first-order cluster operator

$$\hat{\mathcal{T}}^{(1)}\left(\omega,\boldsymbol{\mu}\right) = \tau_{\mathbf{i}}^{(1)}\left(\omega,\boldsymbol{\mu}\right)\hat{\boldsymbol{\mu}}_{\mathbf{i}} \tag{4.36}$$

leads to a functional derivate which is frequency independent and identical to the functional derivative of the unperturbed cluster operator $\hat{\mathcal{T}}$

$$\frac{\delta\hat{\mathcal{T}}^{(1)}\left(\omega,\boldsymbol{\mu}\right)}{\delta\tau_{\mathbf{i}}^{(1)}\left(\omega,\boldsymbol{\mu}'\right)} = \frac{\delta\hat{\mathcal{T}}\left(\boldsymbol{\mu}\right)}{\delta\tau_{\mathbf{i}}\left(\boldsymbol{\mu}'\right)} = \hat{\boldsymbol{\mu}}_{\mathbf{i}}\delta\left(\boldsymbol{\mu}-\boldsymbol{\mu}'\right). \tag{4.37}$$

The functional derivative of the projected coupled-cluster equations is given by

$$\begin{aligned}\frac{\delta\Omega_{\mathbf{i}}\left(\boldsymbol{\mu}\right)}{\delta\tau_{\mathbf{j}}\left(\boldsymbol{\mu}'\right)} &= \boldsymbol{Q}_{\boldsymbol{\mu}}\langle_{\mathbf{i}}^{\boldsymbol{\mu}}|\frac{\delta}{\delta\tau_{\mathbf{j}}\left(\boldsymbol{\mu}'\right)}\left(\hat{H}_{N}\,e^{\hat{\mathcal{T}}}\right)|0\rangle_{C}\\ &= \boldsymbol{Q}_{\boldsymbol{\mu}}\langle_{\mathbf{i}}^{\boldsymbol{\mu}}|\left(\hat{H}_{N}\,\frac{\delta\hat{\mathcal{T}}}{\delta\tau_{\mathbf{j}}\left(\boldsymbol{\mu}'\right)}e^{\hat{\mathcal{T}}}\right)|0\rangle_{C},\end{aligned} \tag{4.38}$$

and results in the same expression as the functional derivative of the first-order functional $\Omega_{\mathbf{i}}^{(1)}\left(\omega\right)$ of Eq. (4.32) with respect to the first-order functions $\tau^{(1)}\left(\omega\right)$.

The poles of the coupled-cluster linear response function are determined by the inverse of the operator $\hat{A}\left(\omega\right)$. For coupled-cluster wavefunction this inverse is the resolvent of the coupled-cluster Jacobian so that the poles of the linear response functions are determined by

the eigenvalues of the Jacobian. Thus in order to determine the excitation energies of the system, one has to find the eigenvalues of the coupled-cluster Jacobian

$$\int \mathrm{d}\boldsymbol{\mu}' \frac{\delta\Omega_{\mathbf{i}_n}(\boldsymbol{\mu})}{\delta\tau_{\mathbf{k}_m}(\boldsymbol{\mu}')} x_{\mathbf{k}_m}(\boldsymbol{\mu}') = \omega x_{\mathbf{i}_n}(\boldsymbol{\mu}). \tag{4.39}$$

Note that the coupled-cluster Jacobian is not hermitian. Consequently there is no guarantee for the eigenvalues to be real and the "left-" and "right-" eigenvectors are in general not the same. In order to compute excitation energies it is sufficient to solve for just one set of eigenvectors; For this work the set of right eigenvectors of Eq. (4.39) is chosen. The non-Hermiticity and the therefore resulting problems (see for example Refs. 60–62 or 63) is an intrinsic problem of the theory and does not depend on the chosen basis. It is therefore not further discussed in the scope of this work. Possible solutions are methods based on variational (instead of projected) coupled-cluster (see for example Refs. 64, 65) or the algebraic diagrammatic construction scheme.[66]

4.3 Real-Space Working Equations

For the following sections it will be convenient to introduce the short notation

$$\delta f \equiv \sum_m \delta_m f \equiv \int \mathrm{d}\boldsymbol{\mu} \, \frac{\delta f(\boldsymbol{\mu})}{\delta\tau_{\mathbf{k}_m}(\boldsymbol{\mu}')} x_{\mathbf{k}_m}(\boldsymbol{\mu}'), \tag{4.40}$$

and call δf just the variation of f. Correspondingly δ_n denotes the variation with respect to a specific n-body cluster function. The eigenvalue equation (4.39) of the coupled-cluster Jacobian is then for example compactly denoted as

$$\delta\Omega_{\mathbf{i}} = \omega x_{\mathbf{i}}. \tag{4.41}$$

The variation of the cluster operator $\hat{\mathcal{T}}$ results in a new cluster operator $\hat{\mathcal{R}}$ (see also Eq. (4.37) for the functional derivative of $\hat{\mathcal{T}}$)

$$\delta\hat{\mathcal{T}} \equiv \int \mathrm{d}\boldsymbol{\mu}' \frac{\delta\hat{\mathcal{T}}(\boldsymbol{\mu})}{\delta\tau_{\mathbf{k}_m}(\boldsymbol{\mu})'} x_{\mathbf{k}_m}(\boldsymbol{\mu}) = \int \mathrm{d}\boldsymbol{\mu}' \delta\left(\boldsymbol{\mu} - \boldsymbol{\mu}'\right) x_{\mathbf{k}_m}(\boldsymbol{\mu}') \hat{\boldsymbol{\mu}}_{\mathbf{k}_m}$$
$$= x_{\mathbf{k}_m}(\boldsymbol{\mu}) \hat{\boldsymbol{\mu}}_{\mathbf{k}_m} \equiv \hat{\mathcal{R}} \tag{4.42}$$

In order for $\hat{\mathcal{R}}$ to be a cluster operator in the sense of Eq. (3.6) the functions $x_{\mathbf{i}}$ need to have similar properties than $\tau_{\mathbf{i}}$ *i.e.* they have to be purely virtual and fulfil certain symmetry constraints under particle and index permutation. This is indeed the case since the projected coupled-cluster equations also have the demanded properties and the $x_{\mathbf{i}}$ functions are eigenfunctions of the coupled-cluster Jacobian. Take for example the constraint for the $x_{\mathbf{i}}$ functions to be purely virtual and use the property of the projected coupled-cluster equations

$$\omega Q_n x_{\mathbf{i}} = \delta\left(Q_n \Omega_{\mathbf{i}}\right) = \delta\left(\Omega_{\mathbf{i}}\right) = \omega x_{\mathbf{i}}. \tag{4.43}$$

Equivalently this is done for the symmetry constraints like for example for the two-body cluster functions

$$\hat{P}_{ij}\Omega_{ij} = -\Omega_{ij} \iff \hat{P}_{ij}x_{ij} = -x_{ij} \tag{4.44}$$

$$\hat{P}_{12}\Omega_{ij} = -\Omega_{ij} \iff \hat{P}_{12}x_{ij} = -x_{ij}. \tag{4.45}$$

In diagrammatic notation, the $\hat{\mathcal{R}}$ operators are represented similar to the $\hat{\mathcal{T}}$ operators

$$\hat{\mathcal{R}}_1 \equiv \ \bigvee \ , \ \hat{\mathcal{R}}_2 \equiv \ \bigvee \ \bigvee \ \dots . \tag{4.46}$$

If the variation of a product of $\hat{\mathcal{T}}$ is computed, the product rule for derivatives has to be taken into account. Take for example the variation of the $\hat{\mathcal{T}}_1\hat{\mathcal{T}}_1$ product which is in diagrammatic form given by

$$\delta\left(\bigvee \ \bigvee\right) = \delta_1 \bigvee \ \bigvee = \left(\bigvee \ \bigvee\right) + \left(\bigvee \ \bigvee\right). \tag{4.47}$$

Taking functional derivatives of the projected coupled-cluster equations in connected form is done in the same way. An explicit example is (see also Eq. (3.73))

$$\delta\left(\bigvee\!\!\!\sim\!\!\!\bigvee\right) = \bigvee\!\!\!\sim\!\!\!\bigvee + \bigvee\!\!\!\sim\!\!\!\bigvee$$
$$= Q_{12}g_{12}\left(1 - \hat{P}_{12}\right)\left(|x_i\rangle \otimes |\tau_j\rangle + |\tau_i\rangle \otimes |x_j\rangle\right) \tag{4.48}$$

In Ch. 5 the equations for the closed-shell CC2 Jacobian will be given explicitly.

5 Implementation of Closed-Shell CC2

In this section, the working equations for an implementation of closed-shell real-space correlation energies and excitation energies are derived. Here the second-order approximate coupled cluster singles and doubles model (CC2) is mainly used. The resulting working equations are implemented into MADNESS. Sec. 5.2 mostly follows Ref. 1 while Sec. 5.3 mostly follows Ref. 2. Tabs. 5.1, 5.2 as well as Tab. 5.3 were taken over from Ref. 1 respectively Ref. 2 in slightly modified form. The implementation uses reference orbitals from already existent solvers in MADNESS (see Refs. 5 and 67) and is based on the MRA-MP2 implementation described in Refs. 6, 18, 40.

5.1 Closed-Shell Formulation

In the closed-shell formulation the hole states are doubly occupied spatial orbitals (occupied by one spin-up and one spin-down electron) and the total wavefunction is required to be a singlet state with respect to the total spin operator. With this restriction the cluster-operator becomes spin independent (see Ref. 47 for a formal proof), *i.e.* the cluster-functions are defined on the spatial domain.[47,51] Let in the following the index set $|\mathcal{I}|$ denote the indices over the spatial hole states. The closed-shell Fock operator is then given by

$$\hat{\mathrm{F}} = -\frac{\nabla^2}{2} + 2\hat{\mathrm{J}} - \hat{\mathrm{K}}, \tag{5.1}$$

with the closed-shell Coulomb and exchange operators defined as

$$\hat{\mathrm{J}} = g_i^i, \quad \hat{\mathrm{K}}|f\rangle = g_f^i|i\rangle, \quad \forall |f\rangle \in L^2\left(\mathbb{R}^3\right), \tag{5.2}$$

with $i \in |\mathcal{I}|$, $|i\rangle \equiv |\phi_i\rangle \in L^2\left(\mathbb{R}^3\right)$, and convolutions with the Coulomb potential denoted as

$$g_q^p \equiv \langle p|g_{12}|q\rangle \equiv \int \mathrm{d}\mathbf{r}_2 \, \phi_p^*\left(\mathbf{r}_2\right) g_{12}\phi_q\left(\mathbf{r}_2\right). \tag{5.3}$$

Analogously, the corresponding Coulomb integrals are written as

$$g_{rs}^{pq} \equiv \langle pq|g_{12}|rs\rangle. \tag{5.4}$$

The closed-shell cluster functions τ_i and τ_{ij} are functions of the spatial electron coordinates indexed by the spatial index set $|\mathcal{I}|$

$$|\tau_i\rangle \in L^2\left(\mathbb{R}^3\right), \quad |\tau_{ij}\rangle \in L^2\left(\mathbb{R}^6\right), \quad i,j \in |\mathcal{I}|, \tag{5.5}$$

Additionally, the closed-shell two-body cluster functions are symmetric with respect to mutual permutation of the indices and electron coordinates

$$\hat{P}_{12}\hat{P}_{ij}|\tau_{ij}\rangle = |\tau_{ij}\rangle. \tag{5.6}$$

For a diagrammatic formulation of the closed-shell coupled-cluster equations, the (formal) matrix elements of the operators are no longer antisymmetrized. Instead, additional exchange diagrams are constructed by reconnecting the contracted operators of the original antisymmetrized diagram. The exchange diagrams are connected diagrams which are topological identical if the two-body vertices are joined together and for the doubles equations, the path connecting the index and coordinate pairs $(i,1)$ and $(j,2)$ remains continuously connected.[49] Overall sign and additional factors of the closed-shell terms given by each diagram can again be derived by the topology of the corresponding diagram.[49] The interpretation rules for closed-shell CC2 (and CCSD) diagrams in real-space are summarized in Fig. 5.1

An explicit example for the generation of exchange diagrams, with real-space interpretation according to Fig. 5.1 is given by the S_i^{4c} diagram (see Tab. 5.1)

$$\left(4\langle l|g_{\tau_k}^k|\tau_{il}\rangle_2\right)$$

$$+ \quad \left(-2\langle l|g_{\tau_k}^k|\tau_{il}\rangle_1\right)$$

$$+ \quad \left(-2\langle k|g_{\tau_k}^l|\tau_{il}\rangle_2\right)$$

$$+ \quad \left(\langle k|g_{\tau_k}^l|\tau_{il}\rangle_1\right), \tag{5.7}$$

where, for convolutions over the two-body cluster functions, a subscript denotes the particle on which the convolution acts; take for example
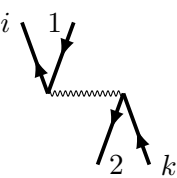
$$\langle k|g_{\tau_k}^l|\tau_{il}\rangle_2 \equiv \int d\mathbf{r}_2 \; \phi_k(\mathbf{r}_2) \, g_{\tau_k}^l(\mathbf{r}_2) \, \tau_{il}(\mathbf{r}_1, \mathbf{r}_2). \tag{5.8}$$
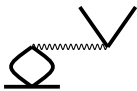
The second diagram in Eq. (5.7) shows the topological structure if the two-body vertices are joined.[a] In the general spin-orbital case, all four diagrams are equivalent leading to only one

---

[a]Such diagrams are referred to as Hugenholtz[68] diagrams while the type of diagrams used in this work are referred to as Goldstone[69] diagrams

Real-space interpretation rules for closed-shell coupled-cluster diagrams

1. All indices $i, j, \ldots$ are part of the closed-shell spatial index set $|\mathcal{I}|$.

2. Label external hole lines from left to right with: $i, j, \ldots$

3. Label external particle lines from left to right with: $1, 2, \ldots$

4. Assign overal sign by $(-1)^{N_{\mathrm{h}} - N_{\mathrm{l}}}$ where N_{h} is the total number of hole-lines and N_{l} the total number of loops (including external loops *i.e.* loops which connect the external particle and hole lines, see section 3.2.1).

5. Multiply with factor $\frac{1}{2}$ if the diagram is symmetric under permutation of external particle and hole labels (affects only diagrams for the doubles equations).

6. Multiply with factor 2 for each internal loop.

7. Interpret one-electron, two-electron, and cluster-operator according to section 3.2.2 with spatial orbitals $|\chi_i\rangle \rightarrow |\phi_i\rangle$, virtual position-eigenstates $|v_\mu\rangle \rightarrow \boldsymbol{Q}|\mathbf{r}_\mu\rangle$, and without antisymmetry in the matrix elements.

$$e.g. \quad \overset{1 \quad i}{\bigvee} \equiv \tau_i(\mathbf{r}_1), \qquad \overset{i \quad 1}{\underset{2 \quad k}{\bigvee}} \equiv \boldsymbol{Q}_{12}\langle \mathbf{r}_1 k | g_{12} | i \mathbf{r}_2 \rangle$$

8. Sum over all indices from internal hole lines (in this work this summation is hidden by the sum convention).

9. Integrate over all coordinates from internal particle lines.

10. Simplify if possible:

    - Absorb $\boldsymbol{Q}$ projectors into the cluster functions
      e.g. $\boldsymbol{Q}|\tau_i\rangle = |\tau_i\rangle$

    - Use the notation $f(\mathbf{r}) \equiv \langle \mathbf{r}|f \rangle$ and the formal resolution of the identity for continuous states[53] $1 = \int d\mathbf{r} |\mathbf{r}\rangle\langle \mathbf{r}|$

      $$e.g. \quad \overset{\bigvee}{\diamondsuit} \equiv \boldsymbol{Q} \int d\mathbf{r}' \langle \mathbf{r}_1 k | g_{12} | i \mathbf{r}' \rangle \tau_k(\mathbf{r}') \equiv \boldsymbol{Q} g_i^k |\tau_k\rangle$$

11. Generate all possible exchange diagrams and interpret them in the same way.

Figure 5.1: Rules for the interpretation of closed shell coupled-cluster diagrams.

diagram with antisymmetrized matrix elements and weight factor one while all four diagrams lead to different contributions in the closed-shell case. Apart from this particular example, the exchange diagrams will not be given explicitly.

5.2 CC2 Ground State Correlation Energies

The coupled-cluster correlation energy (3.37) is in diagrammatic form given by

$$E_{\mathrm{corr}} = \text{(diagrams)} + (2\langle kl|g_{12}|\tau_k\tau_l\rangle - \langle lk|g_{12}|\tau_k\tau_l\rangle)$$
$$+ (2\langle kl|g_{12}|\tau_{kl}\rangle - \langle lk|g_{12}|\tau_{lk}\rangle), \tag{5.9}$$

where the diagrams were interpreted according to Fig. 5.1. For CCSD, the cluster-operator $\hat{\mathcal{T}}$ is truncated after the doubles excitations and the equations for the singles and doubles in connected form are

$$\Omega_i\left(\mathbf{r}_1\right) = \langle{}^1_i|\hat{\mathrm{H}}_{\mathrm{N}}\,e^{\hat{\mathcal{T}}}|0\rangle_{\mathrm{C}} = 0, \qquad\qquad \Omega_i \in L^2\left(\mathbb{R}^3\right), \tag{5.10}$$

$$\Omega_{ij}\left(\mathbf{r}_1,\mathbf{r}_2\right) = \langle{}^{12}_{ij}|\hat{\mathrm{H}}_{\mathrm{N}}\,e^{\hat{\mathcal{T}}}|0\rangle_{\mathrm{C}} = 0, \qquad\qquad \Omega_{ij} \in L^2\left(\mathbb{R}^6\right). \tag{5.11}$$

For the CC2 model, the doubles equations are approximated as

$$\Omega_{ij}\left(\mathbf{r}_1,\mathbf{r}_2\right) \approx \langle{}^{12}_{ij}|\hat{\mathrm{F}}_{\mathrm{N}}\,\hat{\mathcal{T}}_2|0\rangle_{\mathrm{C}} + \langle{}^{12}_{ij}|\hat{\mathrm{H}}_{\mathrm{N}}\,e^{\hat{\mathcal{T}}_1}|0\rangle_{\mathrm{C}} = 0 \tag{5.12}$$

while the singles and the energy equations remain unchanged. Similar to the closed-shell cluster functions, the closed-shell doubles equations are symmetric under simultaneous coordinate and index permutations

$$\Omega_{ij}\left(\mathbf{r}_1,\mathbf{r}_2\right) = \Omega_{ji}\left(\mathbf{r}_2,\mathbf{r}_1\right). \tag{5.13}$$

The connected form of the CCSD equations can be expanded in terms of connected diagrams which are then interpreted according to Fig. 5.1 resulting in[a]

$$|\Omega_i\rangle = \sum_n \boldsymbol{\mathcal{Q}}|\mathrm{S}^n_i\rangle, \tag{5.14}$$

$$|\Omega_{ij}\rangle = \left(1 + \hat{\mathrm{P}}_{ij}\hat{\mathrm{P}}_{12}\right)\sum_n \boldsymbol{\mathcal{Q}}_{12}|\mathrm{D}^n_{ij}\rangle, \tag{5.15}$$

where the corresponding interpretation of the diagrams for the singles and doubles is abbreviated with the symbols S and D. In Tabs. 5.1 and 5.2 the explicit expressions for the diagrams are given. For reasons that will become clear later, the abbreviations $|\mathrm{S}^n_i\rangle$ and $|\mathrm{D}^n_{ij}\rangle$ denote the interpretation of the corresponding diagrams explicitly without the projectors $\boldsymbol{\mathcal{Q}}$ and $\boldsymbol{\mathcal{Q}}_{12}$ resulting from the external lines.

Table 5.1: Diagrams for the closed-shell CC2 singles equations (5.14) and the corresponding interpretation in real-space formalism.[a]

abbrev	diagram	expression
$\boldsymbol{Q}\lvert S_i^{2b}\rangle$		$\boldsymbol{Q}\left(2\langle k\lvert g_{12}\lvert\tau_{ik}\rangle_2 - \langle k\lvert g_{12}\lvert\tau_{ik}\rangle_1\right)$
$\boldsymbol{Q}\lvert S_i^{2c}\rangle$		$-\boldsymbol{Q}\left(2\langle l\lvert g_i^k\lvert\tau_{kl}\rangle_2 - \langle l\lvert g_i^k\lvert\tau_{kl}\rangle_1\right)$
$\boldsymbol{Q}\lvert S_i^{3b}\rangle$		$\boldsymbol{Q}\left(\hat{F}\lvert\tau_i\rangle\right)$
$\boldsymbol{Q}\lvert S_i^{3a}\rangle$		$-\boldsymbol{Q}\left(\lvert\tau_k\rangle\langle k\lvert\hat{F}\lvert i\rangle\right)$
$\boldsymbol{Q}\lvert S_i^{3c}\rangle$		$\boldsymbol{Q}\left(2g_{\tau_k}^k\lvert i\rangle - g_i^k\lvert\tau_k\rangle\right)$
$\boldsymbol{Q}\lvert S_i^{5b}\rangle$		$\boldsymbol{Q}\left(2g_{\tau_k}^k\lvert\tau_i\rangle - g_{\tau_i}^k\lvert\tau_k\rangle\right)$
$\boldsymbol{Q}\lvert S_i^{5c}\rangle$		$-\boldsymbol{Q}\left(2g_{i\tau_l}^{kl} - g_{\tau_l i}^{kl}\right)\lvert\tau_k\rangle$
$\boldsymbol{Q}\lvert S_i^{6}\rangle$		$-\boldsymbol{Q}\left(2g_{\tau_i\tau_l}^{kl} - g_{\tau_l\tau_i}^{kl}\right)\lvert\tau_k\rangle$
$\boldsymbol{Q}\lvert S_i^{4a}\rangle$		$-\boldsymbol{Q}\left(2\langle l\lvert g_{\tau_i}^k\lvert\tau_{kl}\rangle_2 - \langle l\lvert g_{\tau_i}^k\lvert\tau_{kl}\rangle_1\right)$
$\boldsymbol{Q}\lvert S_i^{4b}\rangle$		$-\boldsymbol{Q}\left(2g_{\tau_{il}}^{kl} - g_{\tau_{li}}^{kl}\right)\lvert\tau_k\rangle$
$\boldsymbol{Q}\lvert S_i^{4c}\rangle$		$\boldsymbol{Q}\left(4\langle l\lvert g_{\tau_k}^k\lvert\tau_{il}\rangle_2 - 2\langle l\lvert g_{\tau_k}^k\lvert\tau_{il}\rangle_1\right.$ $\left. -2\langle k\lvert g_{\tau_k}^l\lvert\tau_{il}\rangle_2 + \langle k\lvert g_{\tau_k}^l\lvert\tau_{il}\rangle_1\right)$

[a]Adapted with permission from Ref. 1. Copyright 2017 American Chemical Society.

Table 5.2: Diagrams for the closed-shell CC2 doubles equations (5.15) and the corresponding interpretation in real-space formalism.[a]

abbrev.	diagram	expression
$\boldsymbol{Q}_{12}\lvert\mathrm{D}_{ij}^{1}\rangle$		$\boldsymbol{Q}_{12}\left(\frac{1}{2}g_{12}\lvert ij\rangle\right)$
$\boldsymbol{Q}_{12}\lvert\mathrm{D}_{ij}^{2a}\rangle$		$\boldsymbol{Q}_{12}\left(\hat{\mathrm{F}}\left(\mathbf{r}_1\right)\lvert\tau_{ij}\rangle\right)$
$\boldsymbol{Q}_{12}\lvert\mathrm{D}_{ij}^{2b}\rangle$		$-\boldsymbol{Q}_{12}\left(\lvert\tau_{kj}\rangle\langle k\lvert\hat{\mathrm{F}}\lvert i\rangle\right)$
$\boldsymbol{Q}_{12}\lvert\mathrm{D}_{ij}^{4a}\rangle$		$\boldsymbol{Q}_{12}\left(g_{12}\lvert\tau_i j\rangle\right)$
$\boldsymbol{Q}_{12}\lvert\mathrm{D}_{ij}^{4b}\rangle$		$-\boldsymbol{Q}_{12}\left(\lvert\tau_k\rangle\otimes g_i^k\lvert j\rangle\right)$
$\boldsymbol{Q}_{12}\lvert\mathrm{D}_{ij}^{6a}\rangle$		$\boldsymbol{Q}_{12}\left(\frac{1}{2}g_{12}\lvert\tau_i\tau_j\rangle\right)$
$\boldsymbol{Q}_{12}\lvert\mathrm{D}_{ij}^{6b}\rangle$		$\boldsymbol{Q}_{12}\left(\frac{1}{2}g_{ij}^{kl}\lvert\tau_k\tau_l\rangle\right)$
$\boldsymbol{Q}_{12}\lvert\mathrm{D}_{ij}^{6c}\rangle$		$-\boldsymbol{Q}_{12}\left(\lvert\tau_k\rangle\otimes\left(g_{\tau_i}^k\lvert j\rangle+g_i^k\lvert\tau_j\rangle\right)\right)$
$\boldsymbol{Q}_{12}\lvert\mathrm{D}_{ij}^{8a}\rangle$		$-\boldsymbol{Q}_{12}\left(\lvert\tau_k\rangle\otimes g_{\tau_i}^k\lvert\tau_j\rangle\right)$
$\boldsymbol{Q}_{12}\lvert\mathrm{D}_{ij}^{8b}\rangle$		$\boldsymbol{Q}_{12}\left(g_{\tau_i j}^{kl}\lvert\tau_k\tau_l\rangle\right)$
$\boldsymbol{Q}_{12}\lvert\mathrm{D}_{ij}^{8c}\rangle$		$\boldsymbol{Q}_{12}\left(\frac{1}{2}g_{\tau_i\tau_j}^{kl}\lvert\tau_k\tau_l\rangle\right)$

[a]Adapted with permission from Ref. 1. Copyright 2017 American Chemical Society.

The CC2 equations can be simplified by introducing relaxed orbitals defined by the sum of the hole states with their corresponding one-body cluster function

$$|t_i\rangle = |i\rangle + |\tau_i\rangle. \tag{5.16}$$

Furthermore, modified $\boldsymbol{Q}$ and $\boldsymbol{O}$ projectors introduced similar to Eq. (1.21)

$$\boldsymbol{O}^t \equiv |t_k\rangle\langle k|, \quad \boldsymbol{Q}^t \equiv 1 - \boldsymbol{O}^t. \tag{5.17}$$

Both operators are still projectors

$$\boldsymbol{O}^t\boldsymbol{O}^t = \boldsymbol{O}^t, \quad \boldsymbol{Q}^t\boldsymbol{Q}^t = \boldsymbol{Q}^t. \tag{5.18}$$

While $\boldsymbol{O}^t$ projects onto occupied and virtual space, $\boldsymbol{Q}^t$ still projects onto the virtual space which can be seen by

$$\boldsymbol{Q}\boldsymbol{Q}^t = \boldsymbol{Q}^t, \quad \boldsymbol{O}\boldsymbol{Q}^t = 0. \tag{5.19}$$

Two-body projectors are constructed as before as

$$\boldsymbol{Q}^t_{12} = \boldsymbol{Q}^t \otimes \boldsymbol{Q}^t,. \tag{5.20}$$

The notation will also be used for other functions indexed by $|\mathcal{I}|$ *e.g.* $\boldsymbol{O}^\tau \equiv |\tau_k\rangle\langle k|$.

In the following, the singles and doubles CC2 equations are simplified with the relaxed orbitals t_i and the modified projectors $\boldsymbol{Q}^t$ and $\boldsymbol{Q}^t_{12}$. A useful identity which will be used later is

$$\begin{aligned}
\boldsymbol{Q}^t\left[\hat{\mathrm{F}}, \boldsymbol{Q}^t\right] &= -\boldsymbol{Q}^t\left[\hat{\mathrm{F}}, \boldsymbol{O}^\tau\right] \\
&= -\left[\hat{\mathrm{F}}, \boldsymbol{O}^\tau\right] + \boldsymbol{O}^\tau\left[\hat{\mathrm{F}}, \boldsymbol{O}^\tau\right] \\
&= -\left[\hat{\mathrm{F}}, \boldsymbol{O}^\tau\right] \\
&= \left[\hat{\mathrm{F}}, \boldsymbol{Q}^t\right],
\end{aligned} \tag{5.21}$$

which follows directly from $\left[\hat{\mathrm{F}}, \boldsymbol{Q}\right] = 0$, $\boldsymbol{Q}^t = \boldsymbol{Q} - \boldsymbol{O}^\tau$, $\boldsymbol{O}^\tau\boldsymbol{O}^\tau = 0$, as well as

$$\begin{aligned}
\boldsymbol{O}^\tau\hat{\mathrm{F}}\boldsymbol{O}^\tau &= |\tau_k\rangle\langle k_k|\hat{\mathrm{F}}|\tau_l\rangle\langle l| \\
&= \epsilon_k|\tau_k\rangle\langle k_k|\tau_l\rangle\langle l| = 0
\end{aligned} \tag{5.22}$$

---
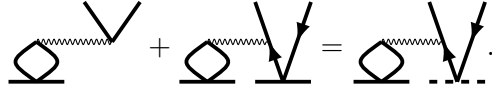
[a]Note that for the doubles the $\left(1 + \hat{\mathrm{P}}_{ij}\hat{\mathrm{P}}_{12}\right)$ operation is sometimes included into the interpretation rules.

5.2.1 Singles Equations

Some of the CC2 singles diagrams in Tab 5.1 can be summed up to give a new diagram with the relaxed orbital t_i instead of the hole state ϕ_i. Take for example the diagrams S^{3c} and S^{5b}

$$
\begin{aligned}
|S_i^{3c}\rangle + |S_i^{5b}\rangle &= \left(2g_{\tau_k}^k|i\rangle - g_i^k|\tau_k\rangle\right) + \left(2g_{\tau_k}^k|\tau_i\rangle - g_{\tau_i}^k|\tau_k\rangle\right) \\
&= \left(2g_{\tau_k}^k|t_i\rangle - g_{t_i}^k|\tau_k\rangle\right) \\
&\equiv |S_{t_i}^{5b}\rangle.
\end{aligned}
\tag{5.23}
$$

Or in diagrammatic notation with dashed bars as relaxed orbitals t_i

$$\tag{5.24}$$

Similarly, it holds that

$$
|S_{t_i}^{4a}\rangle = |S_i^{2c}\rangle + |S_i^{4a}\rangle
\tag{5.25}
$$

$$
|S_{t_i}^{6}\rangle = |S_i^{5c}\rangle + |S_i^{6}\rangle.
\tag{5.26}
$$

Further simplifications can be obtained with the modified projector like

$$
\boldsymbol{Q}^t|S_{t_i}^{5b}\rangle = \boldsymbol{Q}\left(|S_{t_i}^{5b}\rangle + |S_{t_i}^{6}\rangle\right)
\tag{5.27}
$$

$$
\boldsymbol{Q}^t|S_i^{2b}\rangle = \boldsymbol{Q}\left(|S_i^{2b}\rangle + |S_i^{4b}\rangle\right).
\tag{5.28}
$$

Because the $\boldsymbol{Q}$ projector is always present in diagrammatic interpretation and $\boldsymbol{Q}^t\boldsymbol{Q} = \boldsymbol{Q}$ the last two equations are not represented with new diagrams.[a] With this simplifications, the CC2 singles equations can be written as

$$
|\Omega_i\rangle = \left(\hat{F} - \epsilon_i\right)|\tau_i\rangle + |V_{\tau_i}\rangle,
\tag{5.29}
$$

where the applied singles potential was introduced as

$$
|V_{\tau_i}\rangle = \boldsymbol{Q}\left(|S_{t_i}^{4a}\rangle + |S_i^{4c}\rangle\right) + \boldsymbol{Q}^t\left(|S_{t_i}^{5b}\rangle + |S_i^{2b}\rangle\right).
\tag{5.30}
$$

5.2.2 Doubles Equations

Similar to the singles equations in the last section, the doubles equations can be simplified. The following doubles diagrams given in Tab 5.2 can be summed up to new diagrams

$$
\left(1 + \hat{P}_{ij}\hat{P}_{12}\right)|D_{t_it_j}^{6a}\rangle = \left(1 + \hat{P}_{ij}\hat{P}_{12}\right)\left(|D_{ij}^{1}\rangle + |D_{ij}^{4a}\rangle + |D_{ij}^{6a}\rangle\right),
\tag{5.31}
$$

$$
\left(1 + \hat{P}_{ij}\hat{P}_{12}\right)|D_{t_it_j}^{8a}\rangle = \left(1 + \hat{P}_{ij}\hat{P}_{12}\right)\left(|D_{ij}^{4b}\rangle + |D_{ij}^{6c}\rangle + |D_{ij}^{8a}\rangle\right),
\tag{5.32}
$$

$$
\left(1 + \hat{P}_{ij}\hat{P}_{12}\right)|D_{t_it_j}^{8c}\rangle = \left(1 + \hat{P}_{ij}\hat{P}_{12}\right)\left(|D_{ij}^{6b}\rangle + |D_{ij}^{8b}\rangle + |D_{ij}^{8c}\rangle\right).
\tag{5.33}
$$

---

[a]This is the reason why the $\boldsymbol{Q}$ projector is excluded from the short-notation of the $|S\rangle$ and $|D\rangle$ terms. The equation could be represented with $\hat{\mathcal{T}}_1$ transformed diagrams (see section 5.2.4). Since this would only be a partial $\hat{\mathcal{T}}_1$ transformation in specific terms this formulation is not beneficial here.

Those new diagrams can again be summed up to give

$$\left(1 + \hat{P}_{ij}\hat{P}_{12}\right)\boldsymbol{Q}_{12}^{t}|D_{t_it_j}^{6a}\rangle = \left(1 + \hat{P}_{ij}\hat{P}_{12}\right)\boldsymbol{Q}_{12}\left(|D_{t_it_j}^{6a}\rangle + |D_{t_it_j}^{8a}\rangle + |D_{t_it_j}^{8c}\rangle\right)$$
$$= \boldsymbol{Q}_{12}^{t}g_{12}|t_it_j\rangle. \tag{5.34}$$

The CC2 doubles equations are then given in the simple form

$$|\Omega_{ij}\rangle = \left(1 + \hat{P}_{12}\hat{P}_{ij}\right)\left(\boldsymbol{Q}_{12}|D_{ij}^{2a}\rangle + \boldsymbol{Q}_{12}|D_{ij}^{2b}\rangle + \boldsymbol{Q}_{12}^{t}|D_{t_it_j}^{6a}\rangle\right)$$
$$= \left(\hat{F}_{12} - \epsilon_{ij}\right)|\tau_{ij}\rangle + \boldsymbol{Q}_{12}^{t}g_{12}|t_it_j\rangle, \tag{5.35}$$

with the two-body Fock operator $\hat{F}_{12} = \hat{F}(\mathbf{r}_1) + \hat{F}(\mathbf{r}_2)$ and the sum of the corresponding eigenvalues $\epsilon_{ij} = \epsilon_i + \epsilon_j$.

5.2.3 Regularization

The second term on the right hand side of the real-space CC2 doubles equations (5.35) contains the unscreened Coulomb potential

$$\boldsymbol{Q}_{12}^{t}g_{12}|t_it_j\rangle = g_{12}|t_it_j\rangle - \left(\boldsymbol{O}_1^{t} + \boldsymbol{O}_2^{t} - \boldsymbol{O}_{12}^{t}\right)g_{12}|t_it_j\rangle, \tag{5.36}$$

which is singular at the three dimensional subspace spanned by the coalescence points of the two electrons. This and the high separation ranks of the Coulomb potential make Eq. (5.35) unfavourable for a direct grid-based representation. In order for the CC2 doubles equations (5.11) to hold, the singularity has to be cancelled out by another singular term. The only other term which can result in a singularity of similar form is the Laplacian applied to the cluster function. As a consequence, the two-body cluster functions have cusps at the electron-electron coalescence points.[14] Following Refs. [15] and [18] the cusp in the two-body cluster function is introduced by an explicitly correlated ansatz similar as it was done for MP2[18] but with the relaxed orbitals t_i and the modified projector $\boldsymbol{Q}_{12}^{t}$

$$|\tau_{ij}\rangle = |u_{ij}\rangle + \boldsymbol{Q}_{12}^{t}f_{12}|t_it_j\rangle. \tag{5.37}$$

In this work the correlation factor is given by a Slater-type geminal[70]

$$f_{12} = \frac{1}{2\gamma}\left(1 - e^{-\gamma r_{12}}\right), \tag{5.38}$$

with the real parameter $\gamma > 0$. The regularized two-body cluster functions $|u_{ij}\rangle$ inherit the properties from the τ_{ij} functions

$$\boldsymbol{Q}_{12}|u_{ij}\rangle = |u_{ij}\rangle \tag{5.39}$$
$$\hat{P}_{12}\hat{P}_{ij}|u_{ij}\rangle = |u_{ij}\rangle. \tag{5.40}$$

With the explicitly correlated Ansatz of Eq. (5.37) the Coulomb singularity is cancelled from the CC2 doubles equations (5.35). The commutator of the correlation factor with the kinetic energy operator is[15,18]

$$-\frac{1}{2}\left[\nabla_{12}^2, f_{12}\right] = \hat{U}_{12} - g_{12}, \quad \nabla_{12}^2 \equiv \nabla_1^2 + \nabla_2^2, \tag{5.41}$$

with Kutzelniggs regularized two-electron operator which is for the correlation factor of Eq. (5.38) given by

$$\hat{U}_{12} = \frac{1 - e^{-\gamma r_{12}}}{r_{12}} + \frac{\gamma}{2}e^{-\gamma r_{12}} - \frac{1}{2}e^{-\gamma r_{12}}\frac{\mathbf{r}_{12}}{r_{12}}\left(\nabla_1 - \nabla_2\right). \tag{5.42}$$

Using the commutator in Eq. (5.41) and the commutator relation in Eq. (5.21) the following relation holds

$$\left(\hat{F}_{12} - \epsilon_{ij}\right)\boldsymbol{Q}_{12}^t f_{12}|t_i t_j\rangle + \boldsymbol{Q}_{12}^t g_{12}|t_i t_j\rangle \tag{5.43}$$

$$=\boldsymbol{Q}_{12}^t\left\{\left(\hat{F}_{12} - \epsilon_{ij}\right)f_{12} + \left[\hat{F}_{12}, \boldsymbol{Q}_{12}^t\right]f_{12} + g_{12}\right\}|t_i t_j\rangle$$

$$=\boldsymbol{Q}_{12}^t\left\{f_{12}\left(\hat{F}_{12} - \epsilon_{ij}\right) + \left[\hat{F}_{12}, f_{12}\right] + \left[\hat{F}_{12}, \boldsymbol{Q}_{12}^t\right]f_{12} + g_{12}\right\}|t_i t_j\rangle$$

$$=\boldsymbol{Q}_{12}^t\left\{f_{12}\left(\hat{F}_{12} - \epsilon_{ij}\right) - \left[\hat{K}_{12}, f_{12}\right] + \left[\hat{F}_{12}, \boldsymbol{Q}_{12}^t\right]f_{12} + \hat{U}_{12}\right\}|t_i t_j\rangle,$$

$$\equiv\boldsymbol{Q}_{12}^t\tilde{g}_{12}^{(ij)}|t_i t_j\rangle. \tag{5.44}$$

In the last equation the regularized Coulomb operator $\tilde{g}_{12}^{(ij)}$ was introduced

$$\tilde{g}_{12}^{(ij)} \equiv f_{12}\left(\hat{F}_{12} - \epsilon_{ij}\right) - \left[\hat{K}_{12}, f_{12}\right] + \left[\hat{F}_{12}, \boldsymbol{Q}_{12}^t\right]f_{12} + \hat{U}_{12}. \tag{5.45}$$

With this ansatz, the regularized doubles equations are

$$|\Omega_{ij}\rangle = \left(\hat{F}_{12} - \epsilon_{ij}\right)|u_{ij}\rangle + \left(\hat{F}_{12} - \epsilon_{ij}\right)\boldsymbol{Q}_{12}^t f_{12}|t_i t_j\rangle + \boldsymbol{Q}_{12}^t g_{12}|t_i t_j\rangle$$

$$= \left(\hat{F}_{12} - \epsilon_{ij}\right)|u_{ij}\rangle + \boldsymbol{Q}_{12}^t\tilde{g}_{12}^{(ij)}|t_i t_j\rangle, \tag{5.46}$$

and the CC2 energy of Eq. (5.9) is given by

$$E_{\text{corr}} = \text{}$$

$$=2\langle kl|g_{12}|\tau_k\tau_l\rangle - \langle ji|g_{12}|\tau_k\tau_l\rangle$$

$$+ 2\langle kl|g_{12}|u_{kl}\rangle - \langle lk|g_{12}|u_{kl}\rangle$$

$$+ 2\langle kl|g_{12}\boldsymbol{Q}_{12}f_{12}|t_k t_l\rangle - \langle lk|g_{12}\boldsymbol{Q}_{12}f_{12}|t_k t_l\rangle,. \tag{5.47}$$

where the double lines represent the f_{12} correlation factor and the lines representing the two-body cluster functions are interpreted with the regularized u_{ij} functions.

Apart from the chosen explicitly correlated Ansatz, another possibility would be to use the Q_{12} projector instead of Q_{12}^t. With this ansatz the commutator between the Fock operator and the Q_{12}^t projector are replaced by the terms $|D_{t_i t_j}^{8a}\rangle$ and $|D_{t_i t_j}^{8c}\rangle$ of Eqs. (5.32) and (5.33). Since the commutator of the Fock operator and the Q_{12}^t can be efficiently evaluated the given ansatz with the Q_{12}^t projector is preferred in this work. Note also, that the reintroduction of $|D_{t_i t_j}^{8c}\rangle$ into the equation would increase the formal scaling with respect to the number of occupied orbitals by one order of magnitude. The CC2 equations for singles and doubles with the relaxed orbitals t_i and the modified projector Q scale formally as N_{occ}^3 with the number of occupied reference orbitals.

5.2.4 Comparison to $\hat{\mathcal{T}}_1$ Transformed Formulation

The usage of the relaxed orbitals t_i and the corresponding modified projector Q^t is similar to the so called $\hat{\mathcal{T}}_1$ transformed CC2 equations (see Ref. 22 and Ref. 51 for a general introduction). With the $\hat{\mathcal{T}}_1$ transformed Hamiltonian defined as

$$\breve{H} \equiv e^{-\hat{\mathcal{T}}_1}\, \hat{H}_N\, e^{\hat{\mathcal{T}}_1}, \tag{5.48}$$

the CC2 doubles equations in connected form are

$$\langle_{ij}^{12}|\hat{F}\hat{\mathcal{T}}_2|0\rangle_C + \langle_{ij}^{12}|\breve{H}|0\rangle_C = 0. \tag{5.49}$$

The first term of Eq. (5.49) is not affected by the $\hat{\mathcal{T}}_1$ transformation but the second will result in just the $|D_{ij}^1\rangle$ diagram of Tab. 5.2 but with the $\hat{\mathcal{T}}_1$ transformed Coulomb potential $\breve{g}_{12}$. Within the first quantized formulation the $\hat{\mathcal{T}}_1$ operator can be written as[48]

$$\hat{\mathcal{T}}_1 = \sum_n |\tau_k(\mathbf{r}_n)\rangle\langle k(\mathbf{r}_n)| \equiv \sum_n O_n^\tau, \tag{5.50}$$

so that the transformed Coulomb potential becomes[a]

$$\begin{aligned}
\breve{g}_{12} &= e^{-O_1^\tau - O_2^\tau} g_{12} e^{+O_1^\tau + O_2^\tau} \\
&= \left(1 - O_1^\tau - O_2^\tau + O_{12}^\tau\right) g_{12} \left(1 + O_1^\tau + O_2^\tau + O_{12}^\tau\right) \\
&= Q_{12}^\tau g_{12} \tilde{Q}_{12}^\tau,
\end{aligned} \tag{5.51}$$

where the operator $\tilde{Q}^\tau \equiv 1 + O^\tau$ was introduced. An important property of the $\tilde{Q}^\tau$ operator is its application on hole states which results in the relaxed orbitals $\tilde{Q}^\tau|i\rangle = |t_i\rangle$. The second term of Eq. (5.49) is then the same as the second term of Eq. (5.35)

$$\begin{aligned}
\langle_{ij}^{12}|\breve{H}|0\rangle_C &= Q_{12}\breve{g}_{12}|ij\rangle \\
&= Q_{12}^\tau g_{12} \tilde{Q}_{12}^\tau|ij\rangle \\
&= \left(QQ^\tau \otimes QQ^\tau\right) g_{12} \left(\tilde{Q}^\tau|i\rangle \otimes \tilde{Q}^\tau|j\rangle\right) \\
&= Q_{12}^t g_{12}|t_i t_j\rangle.
\end{aligned} \tag{5.52}$$

---

[a]Note that $O^\tau O^\tau = 0$ which follows from $Q|\tau_i\rangle = |\tau_i\rangle$.

The closed-shell CC2 doubles equations given in Eq. (5.35) are therefore equivalent to the real-space representation of the $\hat{\mathcal{T}}_1$ transformed equations given in Ref. 22. This is not the case for the singles equations given in Eq. (5.29) since here the terms including the Fock operator are not transformed. The real-space form of the $\hat{\mathcal{T}}_1$ transformed singles is given in the appendix of Ref. 1.

5.3 CC2 Excitation Energies

In this section, the working equations for the eigenvalues of the coupled-cluster Jacobian in real-space for the closed-shell CC2 model are derived. The ground state cluster functions τ_i and τ_{ij} and the corresponding projected equation in CC2 approximation Ω_i and Ω_{ij} are solved according to section 5.2. Equations for the (right-) eigenfunctions of the CC2 Jacobian are in short notation

$$\delta\Omega_i\left(\mathbf{r}_1\right) = \omega x_i\left(\mathbf{r}_1\right), \qquad\qquad x_i \in L^2\left(\mathbb{R}^3\right), \qquad (5.53)$$

$$\delta\Omega_{ij}\left(\mathbf{r}_1, \mathbf{r}_2\right) = \omega x_{ij}\left(\mathbf{r}_1, \mathbf{r}_2\right), \qquad\qquad x_{ij} \in L^2\left(\mathbb{R}^6\right). \qquad (5.54)$$

The cluster functions x_i and x_{ij} as well as the Jacobian are purely virtual and the doubles have the same permutation symmetries than the ground state cluster functions (see section 4.3)

$$\boldsymbol{Q}|x_i\rangle = |x_i\rangle, \quad \boldsymbol{Q}_{12}|x_{ij}\rangle = |x_{ij}\rangle, \quad \hat{\mathrm{P}}_{ij}\hat{\mathrm{P}}_{12}|x_{ij}\rangle = |x_{ij}\rangle. \qquad (5.55)$$

In diagrammatic form, the singles and doubles equations for the eigenvalues of the Jacobian are given by

$$|\delta\Omega_i\rangle = \sum_n \boldsymbol{Q}|\delta S_i^n\rangle = \omega|x_i\rangle, \qquad (5.56)$$

$$|\delta\Omega_{ij}\rangle = \left(1 + \hat{\mathrm{P}}_{ij}\hat{\mathrm{P}}_{12}\right)\sum_n \boldsymbol{Q}_{12}|\delta D_{ij}^n\rangle = \omega x_{ij}. \qquad (5.57)$$

The variation of the corresponding singles and doubles diagrams is done similar to Sec. 4.3. In the following, the relaxed orbitals t_i (Eq. (5.16)) and the corresponding modified projectors $\boldsymbol{Q}^t, \boldsymbol{Q}_{12}^t$ (Eq. (5.17)) will be used. The variation of t_i and the projectors follows directly from their definition

$$|\delta t_i\rangle = |\delta\tau_i\rangle = |x_i\rangle, \qquad (5.58)$$

$$\delta\boldsymbol{Q}^t = -\delta\boldsymbol{O}^t = -\boldsymbol{O}^x = -|k\rangle\langle x_k|, \qquad (5.59)$$

$$\delta\boldsymbol{Q}_{12}^t = -\boldsymbol{Q}^t \otimes \boldsymbol{O}^x - \boldsymbol{O}^x \otimes \boldsymbol{Q}^t \qquad (5.60)$$

5.3.1 Singles Equations

The variation of the projected singles equations (5.29) is

$$|\delta\Omega_i\rangle = \left(\hat{\mathrm{F}} - \epsilon_i\right)|x_i\rangle + |V_{x_i}\rangle, \qquad (5.61)$$

with the variation of the applied singles potential given by

$$|V_{x_i}\rangle \equiv |\delta V_{\tau_i}\rangle = \boldsymbol{Q}\left(|\delta S_{t_i}^{4a}\rangle + |\delta S_i^{4c}\rangle\right) + \boldsymbol{Q}^t\left(|\delta S_{t_i}^{5b}\rangle + |\delta S_i^{2b}\rangle\right) + \delta\boldsymbol{Q}^t\left(|S_{t_i}^{5b}\rangle + |S_i^{2b}\rangle\right). \quad (5.62)$$

Explicit forms for the variation of the diagrams are given in Tab. 5.3. The eigenvalue equation for the singles part of the Jacobian is rearranged to

$$|\delta\Omega_i\rangle - \omega|x_i\rangle = \left(\hat{F} - \epsilon_i - \omega\right)|x_i\rangle + |\delta V_{\tau_i}\rangle = 0. \quad (5.63)$$

5.3.2 Doubles Equations

The equation for the two-body cluster functions x_{ij} can be derived similar to the singles from the diagrams in Tab. 5.2 or directly as the variation of Eq. (5.35)

$$|\delta\Omega_{ij}\rangle - \omega|x_{ij}\rangle = \left(\hat{F}_{12} - \epsilon_{ij} - \omega\right)|x_{ij}\rangle + \boldsymbol{Q}_{12}^t g_{12}\left(|x_i t_j\rangle + |t_i x_j\rangle\right) + \delta\boldsymbol{Q}_{12}^t g_{12}|t_i t_j\rangle. \quad (5.64)$$

5.3.3 Regularization

The doubles of the applied Jacobian (Eq. (5.64)) are again singular due to the Coulomb potential. A regularization similar to the ground state equations can be realized by choosing an appropriate explicitly correlated ansatz like

$$\begin{aligned}
|x_{ij}\rangle &= |v_{ij}\rangle + \delta\left(\boldsymbol{Q}_{12}^t f_{12}|t_i t_j\rangle\right) \\
&= |v_{ij}\rangle + \boldsymbol{Q}_{12}^t f_{12}\left(|x_i t_j\rangle + |t_i x_j\rangle\right) + \delta\boldsymbol{Q}_{12}^t f_{12}|t_i t_j\rangle.
\end{aligned} \quad (5.65)$$

Since $|x_{ij}\rangle = |\delta\tau_{ij}\rangle$ by definition it follows $|v_{ij}\rangle = |\delta u_{ij}\rangle$ for the regularized two-body functions. The doubles equation (5.54) in regularized form is then given by using the regularized form of the ground state equations (5.46) and the ansatz from Eq. (5.65)
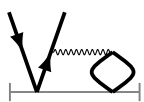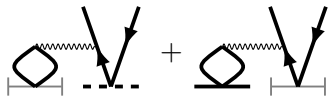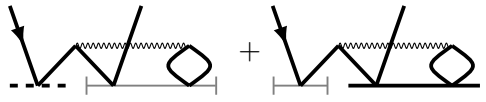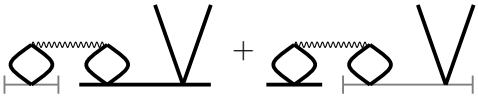
$$\begin{aligned}
|\delta\Omega_{ij}\rangle - \omega|x_{ij}\rangle &= \left(\hat{F}_{12} - \epsilon_{ij}\right)|v_{ij}\rangle + \delta\left(\boldsymbol{Q}_{12}^t \tilde{g}_{12}^{(ij)}|t_i t_j\rangle\right) - \omega|x_{ij}\rangle \\
&= \left(\hat{F}_{12} - \epsilon_{ij} - \omega\right)|v_{ij}\rangle + \delta\left(\boldsymbol{Q}_{12}^t \tilde{g}_{12}^{(ij)}|t_i t_j\rangle\right) - \omega\delta\left(\boldsymbol{Q}_{12}^t f_{12}|t_i t_j\rangle\right) \\
&= \left(\hat{F}_{12} - \epsilon_{ij} - \omega\right)|v_{ij}\rangle + \delta\left(\boldsymbol{Q}_{12}^t\left(\tilde{g}_{12}^{(ij)} - \omega f_{12}\right)|t_i t_j\rangle\right) \\
&= \left(\hat{F}_{12} - \epsilon_{ij} - \omega\right)|v_{ij}\rangle + \delta\left(\hat{V}_r^{(ij)}|t_i t_j\rangle\right)
\end{aligned} \quad (5.66)$$

with the regularized potential defined as

$$\hat{V}_r^{(ij)} \equiv \boldsymbol{Q}_{12}^t\left(\tilde{g}_{12}^{(ij)} - \omega f_{12}\right). \quad (5.67)$$

Again the ansatz chosen in Eq. (5.65) is not the only ansatz which regularizes Eq. (5.54). In particular the second term of the ansatz is not needed and the $\boldsymbol{Q}_{12}^t$ projector could again be replaced by the $\boldsymbol{Q}_{12}$ projector.

Table 5.3: Diagrams for the variation of the closed-shell CC2 singles with respect to the one- and two-body cluster functions of the ground state and the corresponding interpretation in real-space formalism.[a]

abbrev.	diagram and explicit expression
$\boldsymbol{Q}\lvert\delta\mathrm{S}_i^{2\mathrm{b}}\rangle$	$\boldsymbol{Q}\left(2\langle k\lvert g_{12}\lvert x_{ik}\rangle_2 - \langle k\lvert g_{12}\lvert\tau_{ik}\rangle_1\right)$
$\boldsymbol{Q}\lvert\delta\mathrm{S}_{t_i}^{5\mathrm{b}}\rangle$	$\boldsymbol{Q}\left(2g_{x_k}^k\lvert t_i\rangle - g_{t_i}^k\lvert x_k\rangle\right)$ $+\boldsymbol{Q}\left(2g_{\tau_k}^k\lvert x_i\rangle - g_{x_i}^k\lvert\tau_k\rangle\right)$
$\boldsymbol{Q}\lvert\delta\mathrm{S}_{t_i}^{4\mathrm{a}}\rangle$	$-\boldsymbol{Q}\left(2\langle l\lvert g_{t_i}^k(2)\lvert x_{kl}\rangle_2 - \langle l\lvert g_{t_i}^k(1)\lvert x_{kl}\rangle_1\right)$ $-\boldsymbol{Q}\left(2\langle l\lvert g_{x_i}^k(2)\lvert\tau_{kl}\rangle_2 - \langle l\lvert g_{x_i}^l(1)\lvert\tau_{kl}\rangle_1\right)$
$\boldsymbol{Q}\lvert\delta\mathrm{S}_i^{4\mathrm{c}}\rangle$	$\boldsymbol{Q}\left(4\langle l\lvert g_{x_k}^k\lvert\tau_{il}\rangle_2 - 2\langle l\lvert g_{x_k}^k\lvert\tau_{il}\rangle_1 - 2\langle k\lvert g_{x_k}^l\lvert\tau_{il}\rangle_2 + \langle k\lvert g_{x_k}^l\lvert\tau_{il}\rangle_1\right)$ $+\boldsymbol{Q}\left(4\langle l\lvert g_{\tau_k}^k\lvert x_{il}\rangle_2 - 2\langle l\lvert g_{\tau_k}^k\lvert x_{il}\rangle_1 - 2\langle k\lvert g_{\tau_k}^l\lvert x_{il}\rangle_2 + \langle k\lvert g_{\tau_k}^l\lvert x_{il}\rangle_1\right)$

[a]Adapted with permission from Ref. 2. Copyright 2017 American Chemical Society.

5.4 Implementation Details

The closed-shell CC2 equations for excitation energies and ground state correlation are solved similar to the Hartree-Fock equations (1.27) given in section 1.5. In order to solve for the ground state singles, the following equation is iterated

$$|\tau_i\rangle = -2\,\hat{G}_\mu\left\{\hat{v}_f|\tau_i\rangle + |V_{\tau_i}\rangle\right\}, \quad \mu = \sqrt{-2\epsilon_i} \tag{5.68}$$

where $\hat{G}_\mu$ is the three dimensional BSH Green's operator (see Eq. (1.28)). Similar the regularized doubles are determined by

$$|u_{ij}\rangle = -2\,\hat{G}_\mu\left(\mathbf{r}_1,\mathbf{r}_2\right)\left\{\left(\hat{v}_f\left(\mathbf{r}_1\right)+\hat{v}_f\left(\mathbf{r}_2\right)\right)|u_{ij}\rangle + \mathbf{Q}_{12}^t\tilde{g}_{12}^{(ij)}|t_it_j\rangle\right\}, \quad \mu = \sqrt{-2\epsilon_{ij}}, \tag{5.69}$$

with the six dimensional BSH Green's operator. In the same way the singles and regularized doubles of the Jacobian eigenvector are solved. The singles of the CC2 Jacobian eigenvectors are determined by

$$|x_i\rangle = -2\,\hat{G}_\mu\left\{\hat{v}_f|x_i\rangle + |V_{x_i}\rangle\right\}, \quad \mu = \sqrt{-2\left(\epsilon_i+\omega\right)}, \tag{5.70}$$

and correspondingly the doubles of the CC2 eigenvectors

$$|v_{ij}\rangle = -2\,\hat{G}_\mu\left(\mathbf{r}_1,\mathbf{r}_2\right)\left\{\left(\hat{v}_f\left(\mathbf{r}_1\right)+\hat{v}_f\left(\mathbf{r}_2\right)\right)|v_{ij}\rangle + \delta\left(\hat{V}_r^{(ij)}|t_it_j\rangle\right)\right\}, \quad \mu = \sqrt{-2\left(\epsilon_{ij}+\omega\right)}. \tag{5.71}$$

The excitation energy is computed from Eq. (5.56) as

$$\omega = \frac{\langle x_k|\delta\Omega_k\rangle}{\langle\mathbf{x}|\mathbf{x}\rangle}, \quad \langle\mathbf{x}|\mathbf{x}\rangle \equiv \sum_k\langle x_k|x_k\rangle, \tag{5.72}$$

where the "bra"-element $\langle x|$ is the same one-body part of the "right"-eigenvector of the CC2 Jacobian, and the kinetic part is evaluated by partial integration

$$-\frac{1}{2}\langle x_k|\nabla^2|x_k\rangle = \frac{1}{2}\langle\nabla x_k|\nabla x_k\rangle. \tag{5.73}$$

On demand, the singles can be normalized.

For convenience, the definitions of the applied singles potential $|V_{\tau_i}\rangle$ and the regularized doubles potentials $\tilde{g}_{12}^{(ij)}$ and $\hat{V}_r^{(ij)}$ are repeated here:

$$|V_{\tau_i}\rangle \equiv \mathbf{Q}\left(|S_{t_i}^{4a}\rangle + |S_i^{4c}\rangle\right) + \mathbf{Q}^t\left(|S_{t_i}^{5b}\rangle + |S_i^{2b}\rangle\right), \tag{5.30}$$

$$\tilde{g}_{12}^{(ij)} \equiv \left(f_{12}\left(\hat{F}_{12}-\epsilon_{ij}\right) - \left[\hat{K}_{12},f_{12}\right] + \left[\hat{F}_{12},\mathbf{Q}_{12}^t\right]f_{12} + \hat{U}_{12}\right), \tag{5.45}$$

$$|V_{x_i}\rangle \equiv |\delta V_{\tau_i}\rangle = \mathbf{Q}\left(|\delta S_{t_i}^{4a}\rangle + |\delta S_i^{4c}\rangle\right) + \mathbf{Q}^t\left(|\delta S_{t_i}^{5b}\rangle + |\delta S_i^{2b}\rangle\right) + \delta\mathbf{Q}^t\left(|S_{t_i}^{5b}\rangle + |S_i^{2b}\rangle\right), \tag{5.62}$$

$$\hat{V}_r^{(ij)} \equiv \mathbf{Q}_{12}^t\left(\tilde{g}_{12}^{(ij)} - \omega f_{12}\right). \tag{5.67}$$

5.4.1 NEMO Formalism

Instead of the conventional occupied orbitals, the so called numerical exponential molecular orbitals (NEMOs)[71] can be used. Similar to the explicit correlated ansatz for the electronic cusp, the NEMO ansatz regularizes the singularities arising from the nuclear potentials. While the regularization of the electron-electron singularity is practically unavoidable, the use of the NEMO ansatz is optional; nevertheless, it saves a significant amount of memory (see Ref. 40 for a detailed discussion).

In this section, the NEMO ansatz is introduced briefly; explicit derivations, as well as the specific form of the nuclear correlation factors and the resulting potentials, can be found in Ref. 67 (one-electron part) and Ref. 40 (two-electron part). The used notation for the NEMOs as F_i and the corresponding nuclear correlation factor as R follows Refs. 67 and 40 and will not be used outside of this section.

The NEMO ansatz for the occupied orbitals is given by

$$|i\rangle = R|F_i\rangle, \tag{5.74}$$

where R is the nuclear correlation factor and F_i the NEMO. Unlike the regularization of the electron-electron singularity, the regularized equations are obtained by a similarity transformation. The nuclear correlation factor is therefore always invertible. Compared to the electron-electron correlation factor, the commutator of the nuclear correlation factor with the kinetic energy is built up in a slightly different way from the nuclear Coulomb potential V_{ne} and the corresponding regularized nuclear potential operator $\hat{U}_{ne}$

$$-\frac{1}{2}\left[\nabla, R\right] = R\,\hat{U}_{ne} - R\,V_{ne}\,. \tag{5.75}$$

As an instructive example the NEMO Hartree-Fock equations are given

$$\hat{F}_R\,|F_i\rangle = \epsilon_i|F_i\rangle, \tag{5.76}$$

with the transformed (closed-shell) Fock operator

$$\hat{F}_R \equiv R^{-1}\hat{F}R = -\frac{1}{2}\nabla + 2\hat{J} - \hat{K}_R + \hat{U}_{ne}\,. \tag{5.77}$$

The transformed exchange operator $\hat{K}_R$ acts on NEMOs as

$$\begin{aligned}
\hat{K}_R\,|F_i\rangle &\equiv R^{-1}\hat{K}R|F_i\rangle \\
&= R^{-1}\hat{K}|i\rangle \\
&= R^{-1}|k\rangle\langle k|g_{12}|i\rangle \\
&= |F_k\rangle g_i^k\,.
\end{aligned} \tag{5.78}$$

The convolutions g_i^k still depend on the conventional orbitals and are implemented by introducing $|R|^2$ as weight function

$$g_i^k \equiv \int \mathrm{d}\mathbf{r}_2 \, \phi_k^* \left(\mathbf{r}_2\right) g \left(\mathbf{r}_1 - \mathbf{r}_2\right) \phi_i$$
$$= \int \mathrm{d}\mathbf{r}_2 \, F_k^* \left(\mathbf{r}_2\right) \left|R\left(\mathbf{r}_2\right)\right|^2 g \left(\mathbf{r}_1 - \mathbf{r}_2\right) F_i \left(\mathbf{r}_2\right) \tag{5.79}$$

Other operators like $\boldsymbol{Q}$ and $\hat{\mathrm{J}}$ are transformed in the same way. The NEMO ansatz is used for the cluster functions τ_i and x_i analogously to the occupied orbitals in Eq. (5.74). For two-electron functions, the NEMO ansatz looks like

$$|u_{ij}\rangle = (R \otimes R)\,|\eta_{ij}\rangle \equiv R_{12}|\eta_{ij}\rangle, \tag{5.80}$$

which leads to one additional term in the regularized Coulomb operator (5.45) resulting from the transformed $\hat{\mathrm{U}}_{12}$ potential

$$R_{12}^{-1}\hat{\mathrm{U}}_{12}R_{12} = \hat{\mathrm{U}}_{12} + R_{12}^{-1}\left[\hat{\mathrm{U}}_{12}, R_{12}\right]. \tag{5.81}$$

5.4.2 CIS and CIS(D) Approximation

Besides CC2 models, other models which all can be seen as approximations to CC2 were implemented. For the ground state, this is MP2 and for the excited state CIS and CIS(D).[72] MRA based MP2 and CIS were already implemented into MADNESS and details can be found in Refs. 6, 18, 40 (MP2) and Refs. 11, 73 (CIS).

MP2: The MP2 pair functions can be obtained from the CC2 working equations by setting the ground state singles τ_i to zero

$$|\Omega_{ij}^{\mathrm{MP2}}\rangle = |\Omega_{ij}^{\mathrm{CC2}}\rangle\Big|_{\tau_i=0}$$
$$= \left(\hat{\mathrm{F}}_{12} - \epsilon_{ij}\right)|\tau_{ij}\rangle + \boldsymbol{Q}_{12}g_{12}|ij\rangle, \tag{5.82}$$

and the MP2 correlation energy is

$$E_{\mathrm{corr}}^{\mathrm{MP2}} = 2\langle kl|g_{12}|\tau_{kl}\rangle - \langle lk|g_{12}|\tau_{kl}\rangle. \tag{5.83}$$

CIS: The CIS model uses a CI wavefunction (see Eq. (1.22)) where the cluster operator contains only the one-body cluster operator. CIS excitation energies can be obtained from linear response theory (similar to coupled-cluster, but for CIS the model is in fact variational, see Ref. 57 for details). Another way to obtain the working equation for CIS excitation energy is to use the coupled-cluster singles model (CCS) which results in the same equations for excitation energies. In Ref. 11 the CIS equation were derived by applying the Tamm-Dancoff

approximation (TDA) to the time-dependent Hartree-Fock equations. All three ways lead to the same working equations which are

$$|\delta\Omega_i^{\text{CIS}}\rangle = \mathcal{Q}|\text{S}_i^{3\text{a}}\rangle + \mathcal{Q}|\text{S}_i^{3\text{b}}\rangle + \mathcal{Q}|\text{S}_i^{3\text{c}}\rangle = \omega|x_i\rangle. \tag{5.84}$$

The CIS vectors $|\mathbf{x}^{\text{CIS}}\rangle$ are normalized, and the CIS energy is given by

$$\omega^{\text{CIS}} = \langle x_k|\Omega_k^{\text{CIS}}\rangle. \tag{5.85}$$

CIS(D): CIS(D) uses MP2 as ground state, the CIS functions as excited state singles, and the excited state doubles are obtained from the CC2 working equations by setting the ground state singles to zero

$$|\delta\Omega_{ij}^{\text{CIS(D)}}\rangle = |\delta\Omega_{ij}^{\text{CC2}}\rangle\Big|_{\tau_i=0}. \tag{5.86}$$

The CIS(D) excitation energy is calculated similar to the CC2 excitation energy in Eq. (5.72); again, with the ground state singles set to zero

$$\begin{aligned}
\omega^{\text{CIS(D)}} &= \langle x_k|\delta\Omega_k\rangle\Big|_{\tau_i=0} \\
&= \sum_n \langle x_k|\text{S}_k^n\rangle\Big|_{\tau_i=0} \\
&= \omega^{\text{CIS}} + \left(\langle x_k|\delta\text{S}_k^{2\text{b}}\rangle + \langle x_k|\delta\text{S}_k^{2\text{c}}\rangle + \langle x_k|\delta\text{S}_k^{4\text{a}}\rangle + \langle x_k|\delta\text{S}_k^{4\text{b}}\rangle + \langle x_k|\delta\text{S}_k^{4\text{c}}\rangle\right)\Big|_{\tau_i=0}. \tag{5.87}
\end{aligned}$$

For the case, that there is only one hole state the $\text{S}^{4\text{a}}$ and $\text{S}^{4\text{c}}$ parts cancel each other and the $\text{S}^{4\text{b}}$ part becomes equal to the MP2 correlation energy. The CIS(D) energy is in this case

$$\begin{aligned}
\omega^{\text{CIS(D)}} &= \omega^{\text{CIS}} + E_{\text{corr}}^{\text{MP2}} + \left(\langle x_1|\delta\text{S}_1^{2\text{b}}\rangle + \langle x_1|\delta\text{S}_1^{2\text{c}}\rangle\right)\Big|_{\tau_1=0} \\
&= \omega^{\text{CIS}} + E_{\text{corr}}^{\text{MP2}} + E_{\text{corr}}^{\text{CIS(D)}}. \tag{5.88}
\end{aligned}$$

The $E_{\text{corr}}^{\text{CIS(D)}}$ term is structurally comparable with the MP2 correlation energy since it can be written as

$$E_{\text{corr}}^{\text{CIS(D)}} = \langle 0|\hat{\mathcal{R}}_1^\dagger\,\hat{\text{H}}_{\text{N}}\,\hat{\mathcal{R}}_2|0\rangle = \langle\text{CIS}|\,\hat{\text{H}}_{\text{N}}\,\hat{\mathcal{R}}_2|0\rangle, \tag{5.89}$$

with $\hat{\mathcal{R}}_1$ and $\hat{\mathcal{R}}_2$ as the cluster operators which excite into the CIS singles and CIS(D) doubles. With $\hat{\mathcal{T}}_2$ as the cluster operator for the MP2 doubles, the MP2 correlation energy can be written in a similar way

$$E_{\text{corr}}^{\text{MP2}} = \langle 0|\,\hat{\text{H}}_{\text{N}}\,\hat{\mathcal{T}}_2|0\rangle. \tag{5.90}$$

Because of this structural similarity, the $E_{\text{corr}}^{\text{CIS(D)}}$ term is interpreted as correlation energy of the excited state. Note again, that this holds only for closed-shell systems with only one occupied orbital.

Table 5.4: Parameters and corresponding keywords in MADNESS

parameter	keyword	description
$\tilde{\epsilon}$	thresh_3D	MRA threshold for 3D functions
ϵ	thresh_6D	MRA threshold for 6D functions
d_1	dconv_3D	convergence for Green's operator iteration of one-body functions
d_2	dconv_6D	convergence for Green's operator iteration of two-body functions
d_3	econv	energy convergence
N_{f}	freeze	Freeze hole states 1 to N_{f}
L	L	size of the one- and two-body simulation boxes $\Omega^3 = (-L, L)^3$ and $\Omega^6 = (-L, L)^6$

5.4.3 Iteration Scheme

The working equations of the last section are iterated subsequently until an overall convergence is reached. For the ground state equations, the singles and doubles can be initialized as zero functions since the equations for the doubles (5.69) have a non-vanishing inhomogeneity. This makes the first iteration of the CC2 ground state doubles equivalent to MP2.

For the calculation of excitation energies the doubles are again initialized as zero functions. Since the excited state doubles have no inhomogeneity which is not proportional to the excited state singles, an initialization of singles and doubles as zero functions results in the trivial solution to the equations. Instead, a CIS calculation is performed beforehand (see Refs. 11 and 73) and the result is used as first guess for the CC2 calculation.

In Fig. 5.2 the iteration scheme is given as a flow chart and a description of the parameters is given in Tab. 5.4. Both algorithms require converged Hartree-Fock orbitals which are computed with MADNESS in a previous step (see section 1.5 or Refs. 5 and 33 for more details).

5.4.4 Evaluation of Fock Operator Dependent Terms

In the working equations for the ground state correlation energies (Eqs. (5.68) and (5.69)) as well as for the excitation energies (Eqs. (5.70) and (5.71)), several terms are left which still include the Fock operator. For the ground state those terms are

$$f_{12} \left(\hat{\mathrm{F}}_{12} - \epsilon_{ij} \right) |t_i t_j\rangle, \tag{5.91}$$

$$\left[\hat{\mathrm{F}}_{12}, \boldsymbol{Q}_{12}^t \right] f_{12} |t_i t_j\rangle, \tag{5.92}$$
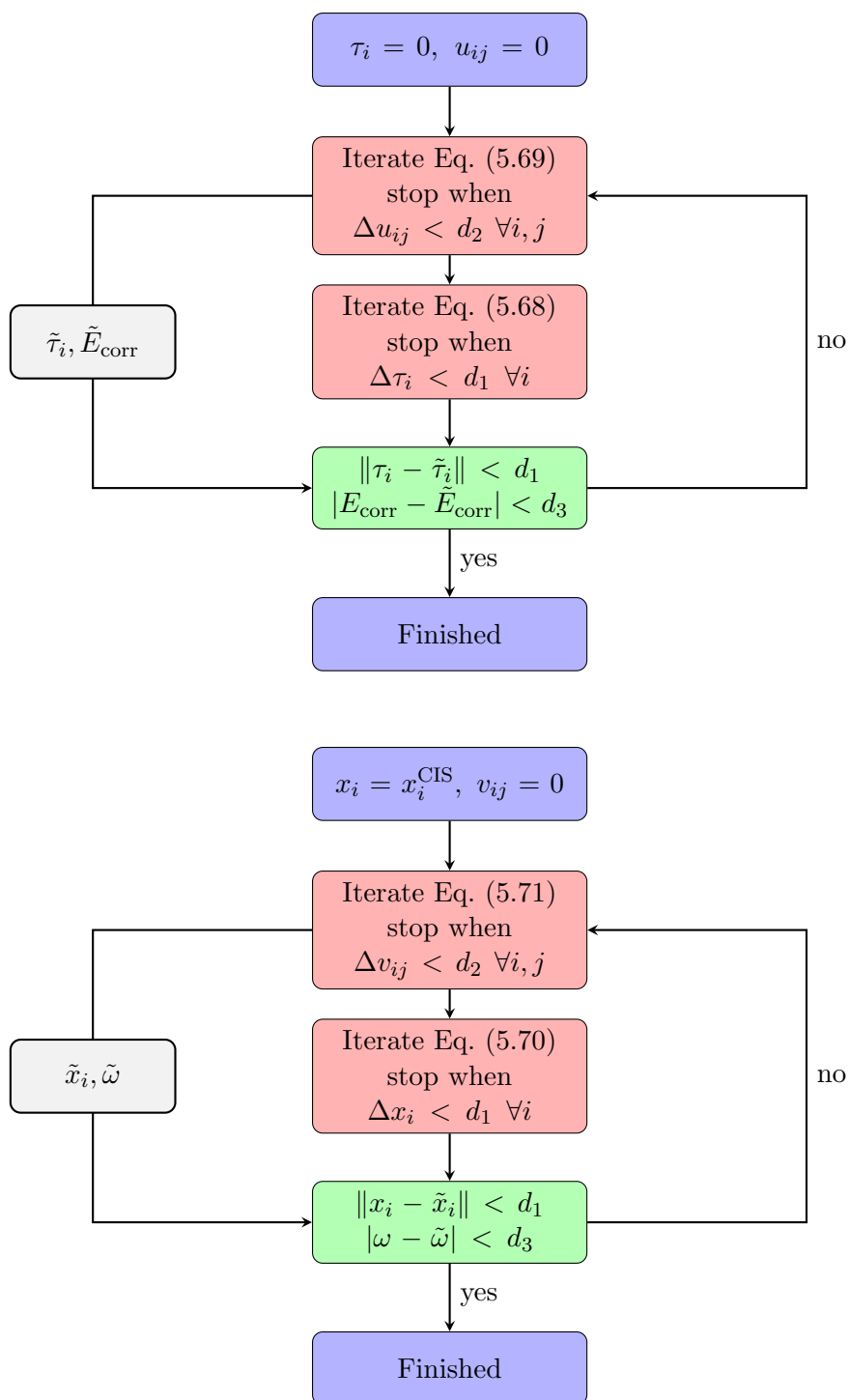
Figure 5.2: Flowcharts for the determination of the CC2 ground state correlation energies (top) and excitation energies (bottom).

and they can be evaluated with the singles equation (5.29) rearranged to

$$\left(\hat{F} - \epsilon_i\right)|\tau_i\rangle = -|V_{\tau_i}\rangle. \tag{5.93}$$

For the term in Eq. (5.91) this leads to [a]

$$\left(\hat{F}_{12} - \epsilon_{ij}\right)|t_i t_j\rangle = \left(\hat{F} - \epsilon_i\right)|t_i\rangle \otimes |t_j\rangle + |t_i\rangle \otimes \left(\hat{F} - \epsilon_j\right)|t_j\rangle$$
$$= -\left(|V_{\tau_i} t_j\rangle + |t_i V_{\tau_j}\rangle\right). \tag{5.94}$$

The commutator from Eq. (5.92) can be evaluated in a similar way by considering the one-particle commutator

$$\left[\hat{F}, \boldsymbol{Q}^t\right] = -\left[\hat{F}, \boldsymbol{O}^t\right]$$
$$= -\left(\hat{F}|t_k\rangle\langle k| - |t_k\rangle\langle k|\hat{F}\right)$$
$$= -\left(\hat{F} - \epsilon_k\right)|\tau_k\rangle\langle k|$$
$$= |V_{\tau_k}\rangle\langle k| \equiv \boldsymbol{O}^{V_\tau}. \tag{5.95}$$

With this, the two-particle commutator from Eq. (5.92) is evaluated as

$$\left[\hat{F}_{12}, \boldsymbol{Q}_{12}^t\right] = \left(1 + \hat{P}_{12}\right)\boldsymbol{Q}^t \otimes \left[\hat{F}, \boldsymbol{Q}^t\right]$$
$$= \left(1 + \hat{P}_{12}\right)\boldsymbol{Q}^t \otimes \boldsymbol{O}^{V_\tau}. \tag{5.96}$$

For the excited state equations the corresponding terms are evaluated similarly with the rearranged singles equations (5.63) leading to

$$\left(\hat{F}_{12} - \epsilon_{ij} - \omega\right)|x_i t_j\rangle = \left(\hat{F} - \epsilon_i - \omega\right)|x_i\rangle \otimes |t_j\rangle + |x_i\rangle \otimes \left(\hat{F} - \epsilon_j\right)|t_j\rangle$$
$$= -\left(|V_{x_i} t_j\rangle + |x_i V_{\tau_j}\rangle\right). \tag{5.97}$$

With the identity (5.21) the variation of the regularized potential can be written as

$$\delta\hat{V}_r^{(ij)} = \delta\boldsymbol{Q}_{12}^t\left(\tilde{g}_{12}^{(ij)} - \omega f_{12}\right) + \boldsymbol{Q}_{12}^t \delta\tilde{g}_{12}^{(ij)}$$
$$= \delta\boldsymbol{Q}_{12}^t\left(\tilde{g}_{12}^{(ij)} - \omega f_{12}\right) + \boldsymbol{Q}_{12}^t\left[\hat{F}_{12}, \delta\boldsymbol{Q}_{12}^t\right] f_{12}$$
$$= \delta\boldsymbol{Q}_{12}^t \tilde{g}_{12}^{(ij)} + \left(\left[\hat{F}_{12}, \delta\boldsymbol{Q}_{12}^t\right] - \omega\delta\boldsymbol{Q}^t\right) f_{12}. \tag{5.98}$$

The second term is evaluated as

$$\left(\left[\hat{F}_{12}, \delta\boldsymbol{Q}_{12}^t\right] - \omega\delta\boldsymbol{Q}_{12}^t\right) = -\left(1 + \hat{P}_{12}\right)\left(\left[\hat{F}_{12}, \boldsymbol{Q}^t \otimes \boldsymbol{O}^x\right] - \omega\boldsymbol{Q}^t \otimes \boldsymbol{O}^x\right)$$
$$= -\left(1 + \hat{P}_{12}\right)\left(\boldsymbol{Q}^t \otimes \left(\left[\hat{F}, \boldsymbol{O}^x\right] - \omega\boldsymbol{O}^x\right) - \left[\hat{F}, \boldsymbol{O}^\tau\right] \otimes \boldsymbol{O}^x\right)$$
$$= \left(1 + \hat{P}_{12}\right)\left(\boldsymbol{Q}^t \otimes \boldsymbol{O}^{V_x} - \boldsymbol{O}^{V_\tau} \otimes \boldsymbol{O}^x\right), \tag{5.99}$$

---

[a]Note that $\left(\hat{F} - \epsilon_i\right)|t_i\rangle = \left(\hat{F} - \epsilon_i\right)|\tau_i\rangle$ since $\left(\hat{F} - \epsilon_i\right)|i\rangle = 0$.

where the following relation for the one-particle commutator was used

$$\left[\hat{F}, O^x\right] - \omega O^x = \left(\hat{F} - \epsilon_k - \omega\right)|x_k\rangle\langle k|$$
$$= -|V_{x_k}\rangle\langle k| \equiv -O^{V_x}. \tag{5.100}$$

5.4.5 Internal Checks

The application of the $\hat{U}_{12}$ operator and the exchange-commutator $\left[\hat{K}_{12}, f_{12}\right]$ in the regularized Coulomb operator (see Eq.(5.45)) can become inaccurate. In order to detect inaccuracies, two internal checks were implemented.

For the exchange commutator, the error results from accumulated inaccuracies of low-rank tensor additions (see Ref. 18). To get an estimate on the magnitude of this error, the expectation value

$$\langle xy|\left[\hat{K}_{12}, f_{12}\right]|xy\rangle = 0, \tag{5.101}$$

is calculated (here x and y are generic functions).

Inaccuracies of the $\hat{U}_{12}$ operator result mainly from undersampling. This problem is solved by enforcing deeper refinement near the electron-electron coalescence points (see also Sec. 2.1). Numerical accuracy of the $\hat{U}_{12}$ operator is checked similar with the relation

$$-\frac{1}{2}\langle xy|\left[\hat{\nabla}_{12}, g_{12}\right]|xy\rangle = \langle xy|\hat{U}_{12}|xy\rangle - \langle xy|g_{12}|xy\rangle = 0. \tag{5.102}$$

6 Numerical Results and Discussion

The implementation of closed-shell MRA-CC2 (as well as CIS, MP2 and CIS(D)) was tested on small molecules which are H_2, BH, BeH_2, CH_2, H_2O, and C_2H_4. Numerical results in comparison with LCAO calculations are given in this section. In this work, the CIS model was mostly used as first guess for CC2; a detailed discussion on the performance of MRA-CIS on small organic molecules can be found in Refs. [11] and [73] (see also Refs. [10] and [12] for the related MRA-TDDFT model). All reported results are given in atomic units. Part of the results were already published in Refs. 1[a] and Refs. 2[b].

6.1 Computational Details

In the following, the used parameters for MRA and LCAO calculations are given.

Molecules The coordinates for the BH and CH_2 molecule were taken from Ref. [20] and Ref. [21]. All other molecules are optimized CC2/aug-cc-pVTZ structures. The coordinates of all used molecules can be found in the appendix A2. In all calculations the 1s orbitals were kept frozen for all non hydrogen atoms (frozen core approximation).

MRA Parameters: The default threshold for the two-body functions (6D MRA representation) was $\epsilon = 10^{-3}$ but for some calculations $\epsilon = 10^{-4}$ was also used (in those cases the two thresholds are explicitly given in the corresponding tables). The one-body threshold (3D MRA representation) was always chosen two magnitudes smaller than the two-body threshold (*i.e.* $\tilde{\epsilon} = 10^{-5}$ and $\tilde{\epsilon} = 10^{-6}$). One- and two-body convergence thresholds were set to $d_1 = 0.1 \cdot d_2$ and $d_2 = \epsilon$. Polynomial orders of the MRA representation were $k = 5$ and $k = 6$. All MRA calculation were performed with the NEMO ansatz using a Slater type nuclear correlation factor with exponent $a = 1.5$ (see Ref. [67]). The size of the simulation box was 60 a_0 in each dimension ($L = 30$). The exponent of the correlation factor was set to $\gamma = 1$.

LCAO calculations: MP2, CIS, CIS(D), CC2, and MP2-F12 calculations where performed with the ricc2[74] module of TURBOMOLE[75]. CC2-F12 energies were computed with KOALA[76,77] and CC2-R12+ results were taken from Ref. [20]. As basis sets mainly the (d-)aug-cc-pVXZ[78–81] basis sets, with the corresponding auxiliary basis sets[82,83] were used. Additionally the XZaPa-NR (X-tuple-ζ augmented polarized augmented nonrelativistic)[84] basis sets were used for BeH_2 (the corresponding auxilliary basis sets are then chosen as the highest aug-cc-pVXZ available). In the case of the 7ZaPa-NR set the k-function of the basis-set were

---

[a]Tabs. 6.3, 6.4, 6.7 and parts of Tab. 6.1
[b]Tabs. 6.13, 6.15 as well as parts of Tab. 6.11 and Tab. 6.12

excluded since TURBOMOLE does not support them. The basis set without k-functions is denoted as 7ZaPa-NR*. Triply augmented basis sets were created by adding the diffuse functions from the doubly augmented set with exponents divided by two. In the same way, the doubly augmented sets for beryllium were created. Basis set extrapolations for correlation energies were computed as[85]

$$\mathrm{CBS}(X,Y) = \frac{E_X X^3 - E_Y Y^3}{X^3 - Y^3}, \tag{6.1}$$

where X and Y denote the cardinal numbers of two aug-cc-pVXZ sets and E_X, E_Y the corresponding correlation energies. MP2-F12 and CC2-F12 denote explicit correlated calculations with F+K approximation, the fixed-amplitudes (SP) ansatz, and an f_{12} exponent of 1.4. For a comparison of the different explicitly correlated CC2 methods with MRA-CC2 see Ref. 2.

Plots: All isosurfaces where created with VESTA[86] and an isovalue of 0.002.

6.2 Ground State Correlation Energies

The MP2 and CC2 correlation energies of BeH_2, BH, CH_2, H_2O, and C_2H_4 are given in Tabs. 6.1 (BeH_2), 6.3 (BH), 6.5 (CH_2), 6.7 (H_2O), and 6.9 (C_2H_4). Additionally the individual MP2 pair correlation energies are given in Tabs. 6.2 (BeH_2), 6.4 (BH), 6.6 (CH_2), 6.8 (H_2O), and 6.10 (C_2H_4); to take the permuted pair into account, off-diagonal pair correlation energies are already multiplied by a factor of two.

BeH_2 and BH: For BeH_2 the MP2 correlation energy of MRA with $\epsilon = 10^{-4}$ agrees perfectly with the best MP2-F12 calculation. The difference between the best CC2 correlation energy obtained with MRA and CC2-F12/aug-cc-pV5Z is similar to the difference between MP2-F12/aug-cc-pV5Z and MP2-F12/7ZaPa-NR*, so that the best MRA result is assumed to be close to the basis set limit. MRA results with $\epsilon = 10^{-3}$ are slightly below the results obtained with the tighter threshold but are still within the targeted accuracy ϵ. The BH molecule shows similar results, where again the difference between CC2-F12/aug-cc-pV5Z and the best MRA results is in the same range as the difference between MP2-F12/aug-cc-pV5Z and MP2-F12/aug-cc-pV6Z. Since the best MRA-MP2 results agrees with MP2-F12/aug-cc-pV6Z it is again assumed that the MRA-CC2 result is close the basis set limit. The individual MP2 pair energies, given in Tab. 6.2 and Tab. 6.4 are also all within the targeted accuracy when compared to the best explicitly correlated calculation. CC2-R12+ results, taken from Ref. 20, slightly overestimate the correlation energy.

CH_2 and H_2O: For the larger molecules CH_2 and H_2O the MRA results differ up to a few millihartree from the extrapolated or explicitly correlated values. The reason for that is an

accumulation of small errors in the individual pair correlation energies. For MP2, the pair correlation energies of MRA, as well as the best explicitly correlated calculation, are given in Tab. 6.6 (CH_2), and Tab. 6.8 (H_2O). The individual pair correlation energies are all within the targeted accuracy, where the largest deviations are in the range of half a millihartree. For correlation energies, the precision, given by the MRA threshold, is only guaranteed for the individual pair energies. In order to have guaranteed accuracy for total correlation energies, the corresponding MRA threshold would depend on the number of pairs and therefore on the system size. For the accurate calculation of total correlation energies of larger molecules, local formulations will therefore be unavoidable.

C_2H_4:   The calculations for the C_2H_4 molecule, given in Tab. 6.9, show a similar behaviour than for H_2O and CH_2, with deviations up to 11 millihartree in the total correlation energy. Again, the individual MP2 pair energies, given in Tab. 6.10, are all within the MRA target accuracy when compared to the best explicitly correlated LCAO result.

Internal Checks: The internal checks of Sec. 5.4.5 were performed within each calculation. For the exchange-commutator, slight deviations ($< 1.5\epsilon$) from the targeted accuracy ϵ were detected for H_2O and the ($\epsilon = 10^{-4}, k = 5$) calculation of BH. Larger deviations of about 5ϵ were detected for the $k = 5$ calculation of the C_2H_4 molecule, while only slight deviations were detected for $k = 6$. In Tab. 6.10 the pair energies and the exchange-commutator accuracy checks are given explicitly for C_2H_4. A direct correlation between the deviation of the pair energies and the inaccuracy of the exchange-commutator is not observed which may be due to the application of the Green's operator and its smoothing properties. For all other calculations the expectation value of the exchange-commutator was below the targeted accuracy. Increasing inaccuracies with growing system size can be expected from the current implementation where a possible solution is again a local formulation of the working equations. An efficient local formulation of the exchange operator within an MRA framework has been described in Ref. 87. Along with the local reformulation of the working equations, an improvement of the low-rank tensor methods which are currently used is expected to increase accuracy and performance further.

Accuracy checks for the $\hat{U}_{12}$ operator were below the targeted accuracy in all calculations.

Table 6.1: Correlation energies (in mE_{h}) for BeH$_2$.[a]

Basis	MP2	CC2	MP2-F12	CC2-F12
aug-cc-pVTZ	-61.60	-61.70	-66.66	-66.79
aug-cc-pVQZ	-64.75	-64.88	-67.10	-67.24
aug-cc-pV5Z	-65.90	-66.03	-67.19	-67.33
CBS(4,5)	-67.10	-67.24		
6ZaPa-NR	-66.44	-66.58	-67.24	
7ZaPa-NR*	-66.64	-66.77	-67.23	
MRA($\epsilon=10^{-3}$,k=5)	-66.63	-66.77		
MRA($\epsilon=10^{-3}$,k=6)	-67.03	-67.17		
MRA($\epsilon=10^{-4}$,k=5)	-67.23	-67.37		

[a]Adapted with permission from Ref. 1.

Copyright 2017 American Chemical Society.

Table 6.2: Deviation of MRA-MP2 and MP2-F12 for the individual pair correlation energies (in mE_{h}) of BeH$_2$.

	MP2-F12	ΔMRA-MP2 ($\epsilon=10^{-3}$)		($\epsilon=10^{-4}$)
Pair	7ZaPa-NR*	(k=5)	(k=6)	(k=5)
2,2	-15.87	-0.14	-0.04	0.00
2,3	-32.54	-0.33	-0.09	0.01
3,3	-18.82	-0.13	-0.07	-0.02

Table 6.3: Correlation energies (in mE_h) for BH.[a]

Basis	MP2	CC2	MP2-F12	CC2-F12	CC2-R12+[b]
aug-cc-pVQZ	−78.63	−79.02	−81.77	−82.19	−81.24
aug-cc-pV5Z	−80.21	−80.62	−81.91	−82.36	−82.02
aug-cc-pV6Z	−80.92	−81.34	−82.00		−82.63
CBS(5,6)	−81.91	−82.33			
MRA($\epsilon=10^{-3}$,k=5)	−81.40	−81.70			
MRA($\epsilon=10^{-3}$,k=6)	−81.69	−81.98			
MRA($\epsilon=10^{-4}$,k=5)	−82.00	−82.47			
MRA($\epsilon=10^{-4}$,k=6)	−81.98	−82.47			

[a]Adapted with permission from Ref. 1

Copyright 2017 American Chemical Society.

[b]CC2-R12+ results taken from the appendix of Ref. 20.

Table 6.4: Deviation of MRA-MP2 and MP2-F12 for the individual pair correlation energies (in mE_h) of BH.[a]

		ΔMRA-MP2 ($\epsilon=10^{-3}$)			
	MP2-F12	($\epsilon=10^{-3}$)		($\epsilon=10^{-4}$)	
Pair	aug-cc-pV6Z	(k=5)	(k=6)	(k=5)	(k=6)
2,2	−27.01	−0.20	−0.12	0.00	−0.01
2,3	−25.91	−0.26	−0.10	0.00	0.04
3,3	−29.08	−0.15	−0.09	−0.00	−0.05

[a]Adapted with permission from Ref. 1. Copyright 2017 American Chemical Society.

Table 6.5: Correlation energies (in mE_h) for CH_2.

Basis	MP2	CC2	MP2-F12
aug-cc-pVQZ	-149.28	-150.02	-155.50
aug-cc-pV5Z	-152.40	-153.18	-155.73
aug-cc-pV6Z	-153.81	-154.59	-155.83
CBS(5,6)	-155.74	-156.53	
MRA(k=5)	-154.28	-154.91	
MRA(k=6)	-154.90	-155.51	

Table 6.6: Deviation of MRA-MP2 and MP2-F12 for the individual pair correlation energies (in mE_h) of CH_2.

	MP2-F12	ΔMRA-MP2	
Pair	aug-cc-pV6Z	(k=5)	(k=6)
2,2	-17.97	-0.18	-0.09
2,3	-32.81	-0.37	-0.24
2,4	-24.72	-0.21	-0.09
3,3	-22.42	-0.20	-0.19
3,4	-30.60	-0.49	-0.30
4,4	-27.31	-0.09	-0.03

Table 6.7: Correlation energies (in mE_h) for H_2O.[a]

Basis	MP2	CC2	MP2-F12	CC2-F12
aug-cc-pVQZ	-286.41	-288.79	-300.02	-302.37
aug-cc-pV5Z	-293.40	-295.77	-300.60	-302.94
aug-cc-pV6Z	-296.46	-298.81	-300.83	
CBS(5,6)	-300.65	-302.98		
MRA(k=5)	-297.52	-299.65		
MRA(k=6)	-298.70	-300.82		

[a]Adapted with permission from Ref. 1

Table 6.8: Deviation of MRA-MP2 and MP2-F12 for the individual pair correlation energies (in mE_h) of H_2O.

Pair	MP2-F12 aug-cc-pV6Z	ΔMRA-MP2 (k=5)	(k=6)
2,2	−13.29	−0.27	−0.14
2,3	−29.38	−0.14	−0.05
2,4	−26.18	−0.26	−0.14
2,5	−28.35	0.06	0.08
3,3	−25.72	−0.54	−0.36
3,4	−41.81	−0.63	−0.51
3,5	−40.35	−0.38	−0.20
4,4	−25.81	−0.52	−0.34
4,5	−43.64	−0.40	−0.34
5,5	−26.31	−0.23	−0.12

Table 6.9: Correlation energies (in mE_h) for C_2H_4.

Basis	MP2	CC2	MP2-F12
aug-cc-pVQZ	−358.40	−361.64	−372.07
aug-cc-pV5Z	−365.21	−368.53	−372.49
aug-cc-pV6Z	−368.31	−371.66	−372.66
CBS(5,6)	−372.57	−375.96	
MRA(k=5)	−361.97	−365.30	
MRA(k=6)	−363.74	−367.05	

Table 6.10: Deviation of MRA-MP2 and MP2-F12 for the individual pair correlation energies (in mE_h) of C_2H_4, and the result of the exchange-commutator accuracy check of Eq. (5.101).

Pair	MP2-F12 aug-cc-pV6Z	ΔMRA-MP2 (k=5)	(k=6)	$\langle ij \vert \left[\hat{K}_{12}, f_{12}\right] \vert ij \rangle$ (k=5)	(k=6)
3, 3	−9.81	−0.23	−0.13	−4.81	−1.54
3, 4	−10.04	−0.07	−0.05	−4.82	−1.47
4, 4	−10.36	−0.37	−0.34	−4.20	−1.46
3, 5	−13.67	−0.09	−0.11	−3.61	−1.20
4, 5	−17.52	−0.50	−0.43	−2.54	−0.83
5, 5	−11.13	−0.42	−0.36	−0.15	−0.19
3, 6	−18.92	−0.26	−0.21	−2.65	−1.08
4, 6	−18.78	−0.56	−0.44	−1.91	−0.90
5, 6	−20.84	−0.57	−0.52	−0.21	−0.30
6, 6	−15.15	−0.49	−0.44	−0.32	−0.53
3, 7	−11.46	−0.09	−0.05	−3.63	−1.20
4, 7	−19.35	−0.54	−0.50	−2.73	−0.90
5, 7	−22.51	−0.83	−0.75	−0.20	−0.19
6, 7	−20.59	−0.67	−0.61	−0.27	−0.35
7, 7	−12.77	−0.59	−0.44	−0.21	−0.14
3, 8	−21.72	−0.54	−0.42	−2.87	−1.00
4, 8	−17.83	−0.70	−0.45	−2.08	−0.72
5, 8	−20.83	−0.72	−0.53	−0.27	−0.14
6, 8	−32.74	−1.07	−1.20	−0.25	−0.32
7, 8	−18.92	−0.74	−0.58	−0.32	−0.11
8, 8	−27.73	−0.65	−0.36	−0.30	−0.11

6.3 Excitation Energies

Various excitation energies were calculated for the same molecules as before and the corresponding results are given in Tabs. 6.12 (BeH_2), 6.13 (BH), 6.14 (CH_2), 6.15 (H_2O), and 6.16 (C_2H_4). Additionally, the convergence of CIS(D) excitation energies for two excitations of the hydrogen molecule is investigated in Tab. 6.11. The individual excitation energies are labelled by the irreducible representation of the corresponding symmetry group, where the labelling refers to the irreducible representation of the whole excitation.[a] The transformational behaviour of the corresponding singles functions can be determined from the corresponding reference orbitals and the multiplication table of the corresponding point group. Take for example the B_2 excitation of H_2O with the transformational behaviour of the functions denoted as superscript

$$
\begin{pmatrix} \phi_5^{B_2} \\ \phi_4^{A_1} \\ \phi_3^{B_1} \\ \phi_2^{A_1} \\ \phi_1^{A_1} \end{pmatrix} \xrightarrow{B_2\text{Excitation}} \begin{pmatrix} x_5^{A_1} \\ x_4^{B_2} \\ x_3^{A_2} \\ x_2^{B_2} \\ x_1^{B_2} \end{pmatrix}.
$$

The frozen core approximation is indicated by the transparent notation of the core orbital ϕ_1 and the corresponding singles function x_1. Since only singlet excitations are calculated the spin multiplicity will not be denoted explicitly.

H_2: For two electron systems, like H_2, the CIS(D) energy consists of three formally[b] independent parts (see Sec. 5.4.2). For the Σ_u^+ excitation energy, which is the lowest excitation energy of H_2, the deviation of the CIS(D) excitation energy is dominated by the deviation of the MP2 correlation energy. In the case of the d-aug-cc-pV6Z calculation, where the deviation in the CIS energy approaches zero, the deviation of CIS(D) is equal to the deviation in MP2. In Fig. 6.1 the CIS functions for the two H_2 states are represented. Both functions are comparable in diffuseness. The Σ_u^+ state can be well approximated with s-functions which are diffuse enough in the singly augmented basis sets. The s-functions, centred at the hydrogen atoms, are not able to represent the nodal structure of the Π_u state, but p-functions are. Since the aug-cc-pVXZ series adds more p-functions, which tend to get more diffuse with rising cardinal number X, the results improve but still differ significantly from the MRA calculation. In order to accurately describe the diffuse Π_u state, doubly augmented sets are necessary. For the doubly augmented basis sets, the Π_u state shows a similar behaviour than the Σ_u^+ state for the singly augmented sets and the deviation from the MRA calculation is again dominated by the MP2 deviation. The MRA results calculated with $\epsilon = 10^{-3}$

---

[a]Note that the MADNESS implementation of MRA-CC2 does neither exploit nor enforce spatial symmetry. For the TURBOMOLE calculations, the largest Abelian subgroup of the corresponding symmetry group was used.

[b]All parts still depend on the reference orbitals and the term which is interpreted as the CIS(D) correlation energy depends on the CIS orbitals.

are close to the $\epsilon = 10^{-4}$ results and all deviations are below the targeted accuracy. The non-monotonous convergence of the CIS error for double-ζ basis sets can be explained by the unconverged reference orbitals indicated by the Hartree-Fock eigenvalues ϵ_1 where the deviation is larger than for the CIS excitation energy.

BeH$_2$: The first four excitation energies in Tab. 6.12 (labelled as $\Pi_{\rm g}$, $\Pi_{\rm u}$, $\Sigma_{\rm u}^+$, and $\Sigma_{\rm g}^+$) are in good agreement with the largest LCAO calculations for all three models. For the last two states ($2\Sigma_{\rm u}^+$ and $\Delta_{\rm u}$), triply augmented basis sets are needed in order to accurately describe the excitation. The excitation energy for the $2\Sigma_{\rm u}^+$ state did not converged to the expected state. Instead, convergence towards the first $\Sigma_{\rm u}^+$, or towards the $\Pi_{\rm u}$ excitation energy were observed; a problem known from MRA-CIS.[11] Convergence to a different state usually occurs if the used guess has significant overlap with a lower lying state. Since the application of the Green's function tends to converge to the lowest state possible,[88] such a condition often leads to convergence towards the lower lying state. In MRA-CIS, this problem is solved by orthogonalization of the corresponding states. Since the CC2 Jacobian is not Hermitian, the corresponding eigenstates are not in general orthogonal and orthogonalization like in MRA-CIS is not an option here. Let it be noted at this point that most states computed here are orthogonal by symmetry making this problem less probable to occur. One way to avoid convergence to wrong states would be to compute the corresponding left eigenvectors and use them to orthogonalize the states subsequently. Another possible solution which avoids the calculation of left eigenvectors is to solve for the whole set of demanded excitation energies at once and enforce the condition $\boldsymbol{\Omega} = \mathbf{S}\boldsymbol{\omega}$ to hold after each macro-iteration. The given matrices are defined similar to Ref. 74 as $\boldsymbol{\Omega}_{mn} = \langle x_{\mathbf{i}_m} | \Omega_{\mathbf{i}_n} \rangle$, $\mathbf{S}_{mn} = \langle x_{\mathbf{i}_m} | x_{\mathbf{i}_n} \rangle$ and $\boldsymbol{\omega}_{mn} = \delta_{mn} \omega_m$. Another possible source for this problem here is the diffuse nature of the corresponding state which probably requires a tighter MRA threshold than 10^{-3}. The CIS funtions of the $2\Sigma_{\rm u}$ state are not orthogonal to the CC2 singles functions of the $1\Sigma_{\rm g}$ state, but, are by symmetry orthogonal to the CC2 singles functions of the $\Pi_{\rm g}$ state. The observed convergence towards the $\Pi_{\rm g}$ functions can only occur if the symmetry is broken at some point. This is possible since the current implementation does not enforce point-group symmetry and the corresponding symmetry of a function can be broken by numerical fluctuations. If the targeted accuracy of MRA is not accurate enough to describe a specific state, those numerical fluctuations become larger in magnitude. The high diffuseness of the functions corresponding to the $\Sigma_{\rm u}^+$ excitation might be one of the reasons why the current MRA threshold is not sufficient for that state. Note that the $\Delta_{\rm u}$ state is also highly diffuse but easier to represent with MRA since the nodal planes are dyadic planes of the MRA refinement scheme.

BH: The two calculated BH excitation energies are close to the results obtained with the largest LCAO basis sets. For the Π state the CC2-R12+ is slightly overestimating the excitation energy. This might be inherited from the ground state where the overestimation of the correlation energy was of comparable size, or, from the truncation of the virtual space entering the R12+ residues[20]. In the case of MRA, the Π excitation energy does not change

significantly if the MRA threshold or the polynomial order are changed. For the Σ^+ state the CC2-R12+ result agrees with the MRA results. The two states of the BH molecule were also discussed in Ref. 20 where the pseudo convergence for CC2-R12+ in the Σ^+ state (between the triple- and quadruple-ζ basis sets) was adressed to the unconverged one-electron part. Here, the insufficiency to describe the one-electron part of the CC2 energy is again indicated by the CIS energy.

CH$_2$: For the CH$_2$ molecule the B$_2$ and A$_2$ excitation energies were computed. Both are in good agreement with LCAO based calculations for all models. In the case of CCSD the aug-cc-pV6Z results are close to the basis set limit[21] so that the same is assumed here for CC2.

H$_2$O: For the water molecule the first B$_2$ excitation energy was calculated. The B$_2$ excitation agrees with the CC2-F12 calculations while the conventional LCAO based method underestimates the excitation energy. CC2-F12 with SP ansatz is known to overestimate excitation energies which results from an imbalanced description between excited and ground state.[a] This happens usually for excitations where the dominant singles contributions differ significantly from the ground state orbitals, which is especially the case if those contributions have different symmetry properties. For the B$_2$ excitation of the water molecule, the dominant part of the CC2 singles vector is the x_5 function which transforms under A$_1$. Two of the four active ground state orbitals of H$_2$O also transform under A$_1$. Those orbitals as well as the x_5 function of the CIS singles are depicted in Fig. 6.3. The B$_2$ excitation is therefore not a case where CC2-F12 with SP ansatz typically fails. It is therefore expected here, that the MRA results are close to the true basis set limit of the B$_2$ excitation energy. A CC2-F12 calculation with the so called extended SP ansatz (XSP)[21], where virtual orbitals are included into the F12 residues [b], should verify this result.

C$_2$H$_4$: For the C$_2$H$_4$ molecule the first B$_{1u}$ excitation was computed and the results are given in Tab. 6.16. The results are comparable to H$_2$O where the deviation of MRA and the best LCAO results is about one millihartree. Again, CC2-F12 results tend to converge to the MRA result, but in this case the CC2-F12 results could only be computed up to the triple-ζ basis set for all atoms so that the result is not as reliable as for H$_2$O. A third CC2-F12 calculation with mixed basis sets (aug-cc-pVTZ on hydrogen and aug-cc-pVQZ on carbon atoms) is given to further verify the results. The CC2 and CIS results for the mixed basis set are similar to the results obtained with the quadruple-ζ basis set on all atoms and the CC2-F12 result lies between the k=5 and k=6 MRA results. The B$_{1u}$ excitation of C$_2$H$_4$ is again not a typical case where the SP ansatz of CC2-F12 fails for symmetry reasons: The dominant part of the singles functions is the x_8 function which transforms as A$_g$ and two active orbitals of the reference transform under the same irreducible representation. In

---

[a]A detailed discussion for the SP ansatz and related approaches can be found in Ref. 21 (CCSD) and Refs. 19, 20 (CC2).

[b]See Refs. 21 and 20 for more details and Ref. 2 for a comparison with the explicit correlated ansatz used for MRA-CC2

Fig. 6.4 the corresponding functions are shown. Because of this, and since the CC2-F12 results seem to converge towards the MRA results it can be expected that the MRA results are in fact close the the true basis set limit. As for H_2O, CC2-F12 calculations with XSP ansatz are expected to verify this result further.

Table 6.11: Convergence of CIS(D) for the H_2 molecule. The differences to the MRA($\epsilon = 10^{-4}$, k=6) values are given in mE_h. See Sec. 5.4.2 for the definition of the terms. Note that ϵ_1 denotes the Hartree-Fock eigenvalue of the occupied orbital.[a]

	GS		$A_{1u} = \Sigma_u^+$			$E_{1u} = \Pi_u$		
Basis[b]	ϵ_1	E_{corr}^{MP2}	ω_{CIS}	$\omega_{CIS(D)}$	$E_{corr}^{CIS(D)}$	ω_{CIS}	$\omega_{CIS(D)}$	$E_{corr}^{CIS(D)}$
apVDZ	−2.14	−6.99	1.25	5.71	−2.54	−98.09	−92.81	−1.71
apVTZ	−0.25	−2.28	−0.04	1.62	−0.62	−51.85	−45.44	4.14
apVQZ	−0.04	−1.01	−0.07	0.71	−0.23	−33.71	−29.09	3.60
apV5Z	−0.00	−0.52	−0.15	0.27	−0.10	−24.22	−20.73	2.98
apV6Z	−0.00	−0.30	−0.08	0.21	−0.02	−18.32	−15.53	2.49
dapVDZ	−2.09	−6.94	1.51	5.97	−2.47	0.77	4.29	−3.42
dapVQZ	−0.26	−2.26	0.20	1.90	−0.56	−0.14	1.65	−0.47
dapVQZ	−0.04	−1.00	0.00	0.80	−0.20	−0.21	0.69	−0.11
dapV5Z	−0.00	−0.51	−0.02	0.43	−0.06	−0.15	0.36	−0.01
dapV6Z	−0.00	−0.30	−0.00	0.30	0.00	−0.10	0.25	0.05
MRA(3,5)	−0.01	0.02	0.00	0.07	0.09	0.01	−0.01	−0.00
MRA(3,6)	−0.00	−0.03	0.00	0.09	0.06	0.00	0.10	0.07
MRA(4,6)	−595.63	−34.25	469.06	473.05	−30.26	482.28	489.26	−27.26

[a]Adapted with permission from Ref. 2. Copyright 2017 American Chemical Society.

[b]apVXZ=aug-cc-pVXZ, dapVXZ=d-aug-cc-pVXZ, MRA(x,y)=MRA($\epsilon = 10^{-x}$, k=y)
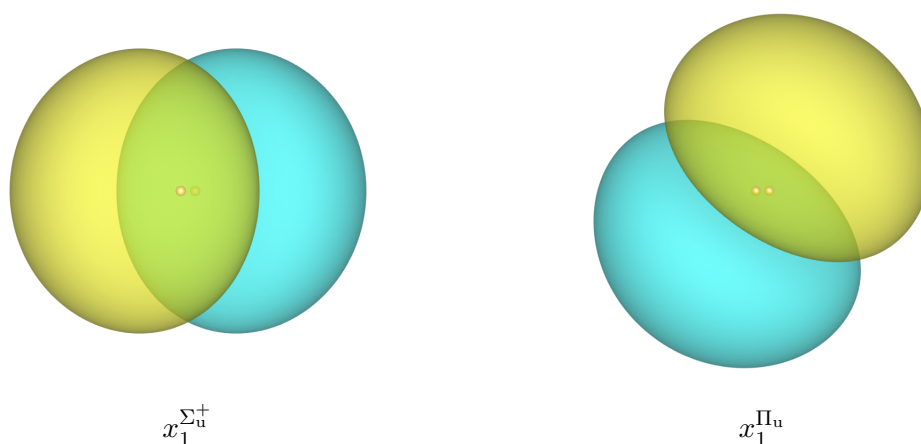
Figure 6.1: The CIS functions for the Σ_u^+ and Π_u states of H_2.

Figure 6.2: The CIS x_3 functions for BeH_2. Note that the superscript labels the irrducible representation of the whole excitation and not of the specific functions.

$x_3^{\Pi_g}$

$x_3^{\Pi_u}$

$x_3^{1\Sigma_u^+}$

$x_3^{\Sigma_g^+}$

$x_3^{2\Sigma_u^+}$

$x_3^{\Delta_u}$
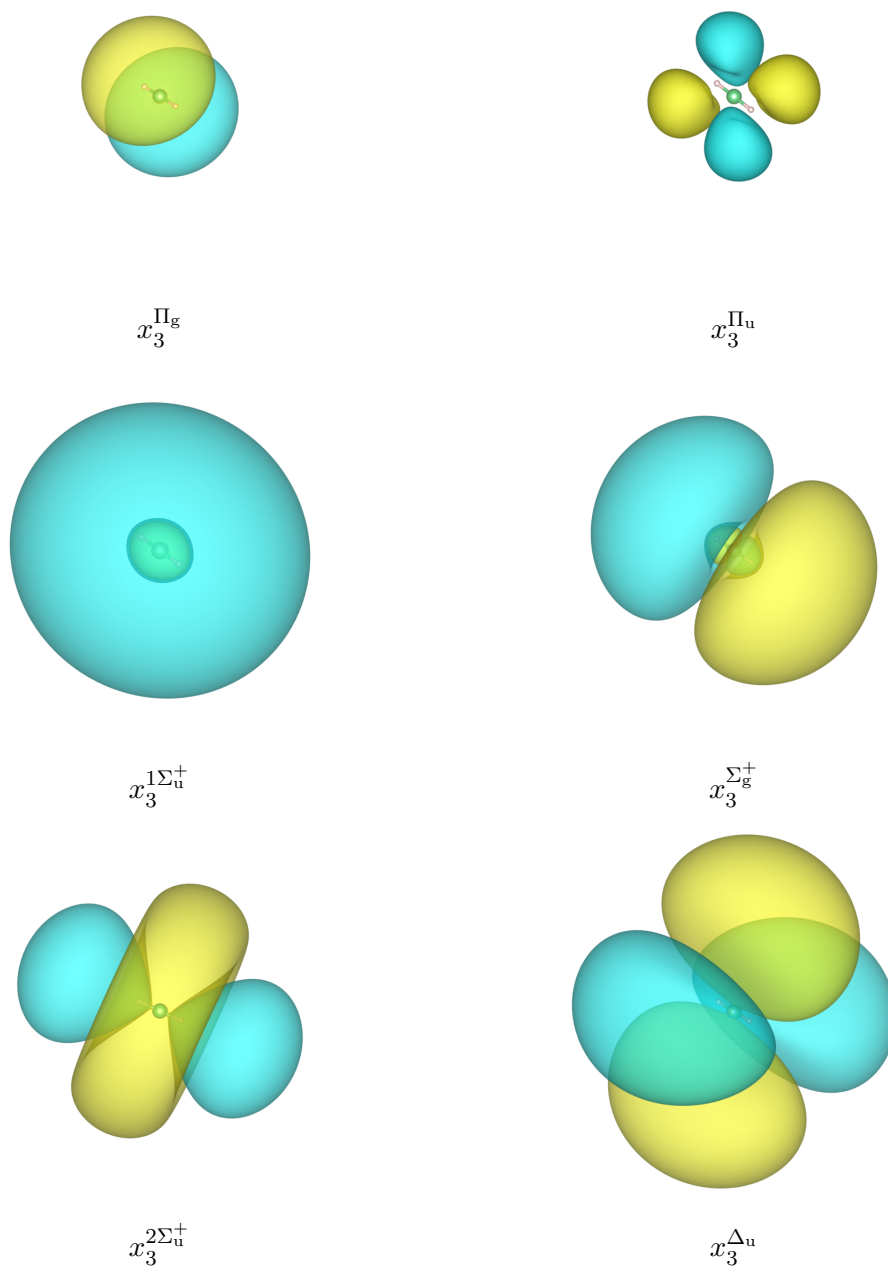
Table 6.12: Excitation energies (in mE_h) for BeH$_2$.[a]

Basis	$E_{1g} = \Pi_g$			$E_{1u} = \Pi_u$		
	CIS	CIS(D)	CC2	CIS	CIS(D)	CC2
aug-cc-pVDZ	259.16	248.78	248.62	340.53	327.82	328.09
aug-cc-pVTZ	259.84	249.83	249.50	339.39	327.32	327.03
aug-cc-pVQZ	259.87	250.20	249.78	338.86	327.36	326.78
aug-cc-pV5Z	259.85	250.31	249.86	338.54	327.38	326.65
7Za-Pa-NR*	259.92	250.43	249.98	338.95	327.61	326.89
MRA(k=5)	259.84	250.29	250.01	338.39	327.36	326.99
MRA(k=6)	259.84	250.44	250.20	338.40	327.58	327.22

	$1A_{1u} = 1\Sigma_u^+$			$A_{1g} = \Sigma_g^+$		
	CIS	CIS(D)	CC2	CIS	CIS(D)	CC2
aug-cc-pVDZ	345.24	340.73	340.41	366.47	362.07	361.74
aug-cc-pVTZ	345.41	344.57	343.69	366.74	366.32	365.33
aug-cc-pVQZ	345.43	345.91	344.80	366.53	367.52	366.26
aug-cc-pV5Z	345.35	346.34	345.15	366.17	367.72	366.36
7Za-Pa-NR*	345.28	346.61	345.37	365.95	367.91	366.48
MRA(k=5)	345.26	346.91	345.63	365.81	367.89	366.52
MRA(k=6)	345.26	347.23	345.98	365.81	368.19	366.82

Basis	$2A_{1u} = 2\Sigma_u^+$			$E_{2u} = \Delta_u$		
	CIS	CIS(D)	CC2	CIS	CIS(D)	CC2
aug-cc-pV5Z	373.40	371.63	370.48	419.73	420.18	419.08
d-aug-cc-pV5Z	370.02	368.90	367.68	396.28	398.04	396.86
t-aug-cc-pV5Z	369.83	368.77	367.54	391.86	393.64	392.46
t-aug-7ZaPa-NR*[a]	369.83	369.07	367.78	391.85	393.99	392.76
MRA(k=5)	369.82	369.01	no conv.	391.65	394.19	392.94
MRA(k=6)	369.82	369.42	no conv.	391.65	394.23	392.96

[a]Adapted with permission from Ref. 2. Copyright 2017 American Chemical Society.

[b]Additional diffuse functions from t-aug-cc-pV5Z*.

Table 6.13: Excitation energies (in m$E_{\rm h}$) for BH.[a]

Basis	$A_1 = \Pi$				$B_1 = \Sigma^+$		
	CIS	CC2	CC2-R12+		CIS	CC2	CC2-R12+[b]
aug-cc-pVDZ	104.75	105.29	107.23		238.41	234.92	238.58
aug-cc-pVTZ	105.16	104.13	104.99		236.43	236.79	238.50
aug-cc-pVQZ	105.19	103.74	103.96		235.91	237.60	238.50
aug-cc-pV5Z	105.20	103.59	103.71		235.42	237.73	238.28
aug-cc-pV6Z	105.20	103.53	103.60		235.22	237.82	238.32
d-aug-cc-pVQZ	104.93	103.12			234.96	237.30	
d-aug-cc-pV5Z	105.20	103.58			234.99	237.41	
d-aug-cc-pV6Z	105.20	103.52			234.99	237.66	
MRA($\epsilon = 10^{-3}$, k=5)	105.20	103.48			234.99	238.29	
MRA($\epsilon = 10^{-3}$, k=6)	105.20	103.49			234.99	238.36	
MRA($\epsilon = 10^{-4}$, k=6)	105.20	103.47					

[a]Adapted with permission from Ref. 2
Copyright 2017 American Chemical Society.
[b]CC2-R12+ results taken from the appendix of Ref. 20

Table 6.14: Excitation energies (in m$E_{\rm h}$) for CH$_2$.

Basis	B$_2$			A$_2$		
	CIS	CIS(D)	CC2	CIS	CIS(D)	CC2
aug-cc-pVTZ	60.77	58.54	59.04	220.22	210.76	211.01
aug-cc-pVQZ	60.85	58.29	58.78	220.27	210.41	210.75
aug-cc-pV5Z	60.86	58.22	58.71	220.29	210.31	210.68
aug-cc-pV6Z	60.87	58.20	58.68	220.30	210.24	210.63
MRA(k=5)	60.86	58.23	58.66	220.30	210.08	210.83
MRA(k=6)	60.86	58.28	58.70	220.30	210.04	210.81

Table 6.15: Excitation energies (in mE_h) for H_2O.[a]

Basis	1B$_2$		
	CIS	CC2	CC2-F12
aug-cc-pVDZ	317.50	259.47	272.22
aug-cc-pVTZ	318.19	264.76	270.51
aug-cc-pVQZ	318.22	266.97	269.75
aug-cc-pV5Z	318.23	267.90	269.45
aug-cc-pV6Z	318.22	268.34	
d-aug-cc-pV6Z	318.19	268.30	
MRA(k=5)	318.18	269.60	
MRA(k=6)	318.16	269.42	

[a]Adapted with permission from Ref. 2.
Copyright 2017 American Chemical Society.

ϕ_2 $\qquad\qquad$ ϕ_4 $\qquad\qquad$ $x_5^{\text{B}_2}$

Figure 6.3: The x_5 function from the B$_2$ excitation of H_2O and the active reference orbitals which transform under the same irreducible representation. Note that B$_2$ labels the irreducible representation of the whole excitation. The four functions transform under A$_1$.

Table 6.16: Excitation energies (in mE_h) for C_2H_4.

Basis	1B$_{1u}$		
	CIS	CC2	CC2-F12
aug-cc-pVDZ	262.11	263.11	270.60
aug-cc-pVTZ	262.03	267.61	270.97
apV(T/Q)Z[a]	262.17	269.34	271.21
aug-cc-pVQZ	261.99	269.34	
aug-cc-pV5Z	261.82	269.88	
aug-cc-pV6Z	261.75	270.14	
MRA(k=5)	261.66	271.38	
MRA(k=6)	261.66	271.01	

[a]aug-cc-pVTZ on H and aug-cc-pVQZ on C

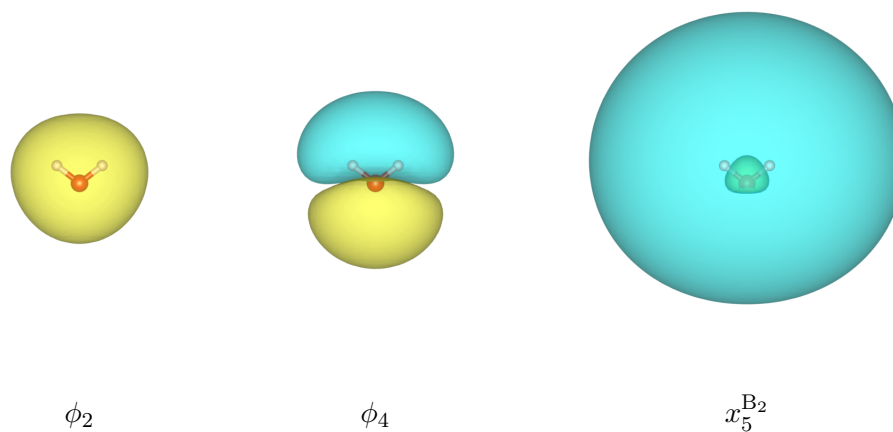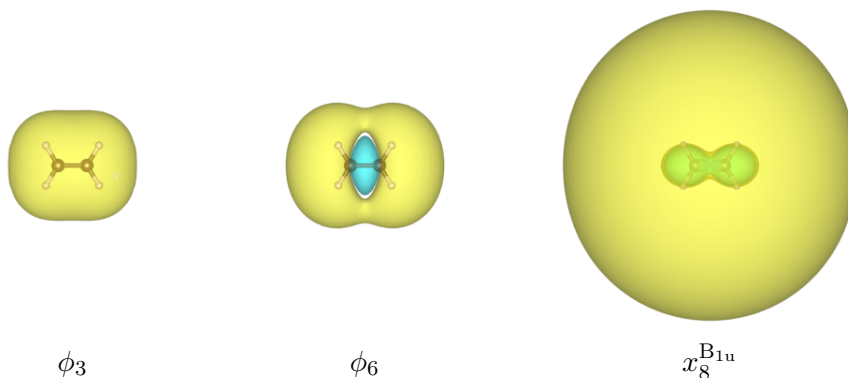ϕ_3 $\qquad\qquad$ ϕ_6 $\qquad\qquad$ $x_8^{B_{1u}}$

Figure 6.4: The x_8 function from the B$_{1u}$ excitation of C_2H_4 and the active reference orbitals which transform under the same irreducible representation. Note that B$_{1u}$ labels the irreducible representation of the whole excitation. The four functions transform under A$_g$.

7 Conclusion and Outlook

In this work real-space coupled-cluster equations were derived and a multiresolution solver for closed-shell CC2 correlation and excitation energies was implemented into the MADNESS library.

The coupled-cluster equations have been formulated in a generalized real-space framework where the cluster operators excite electrons into correlated n-body cluster functions instead of individual virtual orbitals. Conventional coupled-cluster amplitudes are the expansion coefficients if those cluster functions are expanded into (tensor-) products of virtual orbitals. With this connection the real-space and amplitude based forms of the equations can easily be translated into each other. Like in the LCAO based framework, the corresponding equations can be represented diagrammatically where the same diagrams with only slightly adjusted interpretation rules can be used. The working equations are simplified significantly by introducing relaxed orbitals t_i; a procedure which is comparable with the $\hat{\mathcal{T}}_1$-transformation of the Hamiltonian. Excitation energies based on linear response theory can be computed by a set of equations obtained from the functional derivatives of the ground state equations.

An MRA based implementation for ground state correlation energies of excitation energies is only feasible if the two-electron Coulomb singularity is eliminated from the working equations by an explicitly correlated ansatz. Additionally the singularities caused by the nuclear potentials are regularized with the NEMO ansatz which is not as crucial as the regularization of the two-electron singularities but still reduces the amount of data significantly.[40]

For the ground state correlation energies, all pair energies agree well with best explicitly correlated LCAO based results and the deviations are below the given MRA threshold. Deviations of the total correlation energies are larger resulting from an accumulation of small deviations in the individual pair energies. In order to compute total correlation energies with controlled overall precision, the MRA threshold would depend on the number of electrons. It is expected that a local formulation of the current implementation will improve this issue significantly. In addition to the local formulation, tighter thresholds will still be necessary for total correlation energies with millihartree accuracy, especially for larger molecules.

MRA-CC2 excitation energies agree well with the best LCAO based results for all states of the smaller molecules H_2, BeH_2, BH, and CH_2, while for the two states of H_2O and C_2H_4, explicitly correlated approaches are needed for results comparable to MRA-CC2. Other than the ground state correlation energy, excitation energies are relative quantities which are accurate if the functions representing the ground and the excited state are represented in a balanced way. For LCAO based methods this balanced representation is often an issue, es-

pecially for explicitly correlated methods[19,20,61] or if the virtual space is truncated[89] in some way. In both cases the resulting problems are caused by approximations which try to reduce the number of used virtual orbitals. The MRA approach in this work is formulated without virtual orbitals and each function is represented individually in an adaptive and numerically controlled way. Since there is no global truncation, an imbalance between functions of ground and excited state is in general not expected and also not observed in the calculations of this work. For high lying excitation energies and larger (less symmetric) molecules the convergence into lower lying states will become an issue. Possible solutions are either subsequent computation of left and right eigenfunctions and orthonormalization via projection, or simultaneous iteration of multiple roots where the non-Hermitian eigenvalue problem is enforced to hold every macro-iteration. Also, tighter MRA thresholds are probably needed for stable convergence of exited states with strong Rydberg character.

The main bottleneck of the current approach is the vast amount of data needed to represent the six-dimensional two-electron functions and potentials (see also Ref. 6 for a discussion of MRA-MP2 which behaves similar to MRA-CC2 in terms of memory). Usage of low rank tensor representations like high-dimensional SVD reduces the amount of memory significantly. With the NEMO ansatz, the complexity of the functions to represent with MRA is reduced which results in further memory reduction. It is expected that the memory requirement and overall performance can be further reduced by improved low rank representations and optimization of individual algorithms.

A1 Green's Function For the BSH Operator

The Green's Function for the n-dimensional Helmholtz Equation (follwing Kalos[88] and Beylkin[30]) is given by

$$G_\mu (r) = \frac{\mu^\alpha}{(2\pi)^{\alpha+1}} \frac{K_\alpha (\mu r)}{r^\alpha}, \quad \alpha = \frac{n}{2} - 1 \tag{1}$$

In this section a brief justification of this result is given.

The n-dimensional Laplacian is

$$\nabla_n^2 = \frac{1}{r^{n-1}} \frac{\partial}{\partial r} \left(r^{n-1} \frac{\partial}{\partial r} \right) + \hat{A}, \tag{2}$$

where $\hat{A}$ is the angular part. The condition which has to be fulfilled is

$$\left(-\nabla_n^2 + \mu^2 \right) G_\mu \left(|\mathbf{r} - \mathbf{r}'| \right) = \delta \left(|\mathbf{r} - \mathbf{r}'| \right). \tag{3}$$

For $r > 0$ this means

$$\left(-\nabla_n^2 + \mu^2 \right) G(r) = 0. \tag{4}$$

For $r > 0$ and α chosen as above, it holds that

$$
\begin{aligned}
\nabla_n^2 \frac{f}{r^\alpha} &= \frac{1}{r^{n-1}} \frac{\partial}{\partial r} \left(r^{n-1} \frac{\partial}{\partial r} \right) \frac{f(r)}{r^{\frac{n}{2}-1}} \\
&= -\left(\frac{n}{2} - 1 \right)^2 r^{-\left(\frac{n}{2}-1\right)-2} + r^{-\left(\frac{n}{2}-1\right)-1} \frac{\partial f}{\partial r} + r^{-\left(\frac{n}{2}-1\right)} \frac{\partial^2 f}{\partial r^2} \\
&= \left(-\alpha^2 r^{-\alpha-2} + r^{-\alpha-1} \frac{\partial}{\partial r} + r^{-\alpha} \frac{\partial^2}{\partial r^2} \right) f(r).
\end{aligned}
\tag{5}
$$

The condition for the Green's function is then equivalent to the modified Bessel equation

$$
\begin{aligned}
\left(-\nabla_n^2 + \mu^2 \right) \frac{f(r)}{r^\alpha} = 0 &\Leftrightarrow r^\alpha \nabla^2 \left(\frac{f(r)}{r^\alpha} \right) - \mu^2 f(r) = 0 \\
&\Leftrightarrow \left(\frac{\partial^2}{\partial r^2} + r^{-1} \frac{\partial}{\partial r} - \frac{\alpha^2}{r^2} - \mu^2 \right) f(r) = 0 \\
&\Leftrightarrow \left(r^2 \frac{\partial^2}{\partial r^2} + r \frac{\partial}{\partial r} - \left(\alpha^2 + \mu^2 r^2 \right) \right) f(r) = 0.
\end{aligned}
\tag{6}
$$

For $\mu = 1$ this is the modified Bessel equation solved by the modified Bessel function $K_\alpha (r)$. $\mu \neq 1$ corresponds to a transformation $r \to \mu r$ and is solved by $K_\alpha (\mu r)$. The normalization factor $\frac{\mu^\alpha}{(2\pi)^{\alpha+1}}$ ensures equality in Eq. (3). For a derivation based on the Fourier transformation see Ch. 22.4 of Ref. 34.[a] A Gaussian integral representation can be found in Ref. 30.

---

[a]Note that Ref. 34 expresses the Green's function with the Hankel function $H_\alpha^{(1)}$. With the identity $K_\alpha (r) = \frac{\pi}{2} i^{\alpha+1} H_\alpha^{(1)} (ir)$ the representation of Eq. (1) is obtained.

A2 Molecular Coordinates

<table>
<tr><td colspan="4" align="center">Molecular coordinates in a_0</td></tr>
<tr><td colspan="4" align="center">H$_2$</td></tr>
<tr><td>h</td><td>0.00000000000000</td><td>0.00000000000000</td><td>0.69701826106345</td></tr>
<tr><td>h</td><td>0.00000000000000</td><td>0.00000000000000</td><td>-0.69701826106345</td></tr>
<tr><td colspan="4" align="center">BH</td></tr>
<tr><td>b</td><td>0.00000000000000</td><td>0.00000000000000</td><td>-1.16444915420000</td></tr>
<tr><td>h</td><td>0.00000000000000</td><td>0.00000000000000</td><td>1.16444915420000</td></tr>
<tr><td colspan="4" align="center">BeH$_2$</td></tr>
<tr><td>be</td><td>0.00000000000000</td><td>0.00000000000000</td><td>-0.00000000000000</td></tr>
<tr><td>h</td><td>0.00000000000000</td><td>0.00000000000000</td><td>2.51261098858827</td></tr>
<tr><td>h</td><td>0.00000000000000</td><td>0.00000000000000</td><td>-2.51261098858827</td></tr>
<tr><td colspan="4" align="center">CH$_2$</td></tr>
<tr><td>c</td><td>0.00000000000000</td><td>0.00000000000000</td><td>0.18923424000000</td></tr>
<tr><td>h</td><td>-0.00000000000000</td><td>1.62569044000000</td><td>-1.12658982000000</td></tr>
<tr><td>h</td><td>-0.00000000000000</td><td>-1.62569044000000</td><td>-1.12658982000000</td></tr>
<tr><td colspan="4" align="center">H$_2$O</td></tr>
<tr><td>o</td><td>0.00000000000000</td><td>0.00000000000000</td><td>-0.74803583254128</td></tr>
<tr><td>h</td><td>1.43358660382183</td><td>0.00000000000000</td><td>0.37401791627063</td></tr>
<tr><td>h</td><td>-1.43358660382183</td><td>0.00000000000000</td><td>0.37401791627063</td></tr>
<tr><td colspan="4" align="center">C$_2$H$_4$</td></tr>
<tr><td>c</td><td>1.26252820737498</td><td>0.00000000000000</td><td>0.00000000000000</td></tr>
<tr><td>c</td><td>-1.26252820737498</td><td>0.00000000000000</td><td>0.00000000000000</td></tr>
<tr><td>h</td><td>2.32435615900438</td><td>-1.74577043375230</td><td>0.00000000000000</td></tr>
<tr><td>h</td><td>2.32435615900438</td><td>1.74577043375230</td><td>0.00000000000000</td></tr>
<tr><td>h</td><td>-2.32435615900438</td><td>1.74577043375230</td><td>0.00000000000000</td></tr>
<tr><td>h</td><td>-2.32435615900438</td><td>-1.74577043375230</td><td>0.00000000000000</td></tr>
</table>

Bibliography

[1] Kottmann, J. S.; Bischoff, F. A. *J. Chem. Theory Comput.* **2017**, *13*, 5945–5955.

[2] Kottmann, J. S.; Bischoff, F. A. *J. Chem. Theory Comput.* **2017**, *13*, 5956–5965.

[3] Schuchardt, K. L.; Didier, B. T.; Elsethagen, T.; Sun, L.; Gurumoorthi, V.; Chase, J.; Li, J.; Windus, T. L. *J. Chem. Inf. Model.* **2007**, *47*, 1045–1052.

[4] Feller, D. *J. Comput. Chem.* **1996**, *17*, 1571–1586.

[5] Harrison, R. J.; Fann, G. I.; Yanai, T.; Gan, Z.; Beylkin, G. *J. Chem. Phys.* **2004**, *121*, 11587–11598.

[6] Bischoff, F. A.; Valeev, E. F. *J. Chem. Phys.* **2013**, *139*, 114106.

[7] Jensen, S. R.; Saha, S.; Flores-Livas, J. A.; Huhn, W.; Blum, V.; Goedecker, S.; Frediani, L. *J. Phys. Chem. Lett.* **2017**, *8*, 1449–1457.

[8] Yanai, T.; Fann, G. I.; Gan, Z.; Harrison, R. J.; Beylkin, G. *J. Chem. Phys.* **2004**, *121*, 2866–2876.

[9] Bischoff, F. A. *J. Chem. Phys.* **2017**, *146*, 124126.

[10] Yanai, T.; Harrison, R. J.; Handy, N. *Mol. Phys.* **2005**, *103*, 413–424.

[11] Kottmann, J. S.; Höfener, S.; Bischoff, F. A. *Phys. Chem. Chem. Phys.* **2015**, *17*, 31453–31462.

[12] Yanai, T.; Fann, G. I.; Beylkin, G.; Harrison, R. J. *Phys. Chem. Chem. Phys.* **2015**, *17*, 31405–31416.

[13] Jensen, S. R.; Flå, T.; Jonsson, D.; Monstad, R. S.; Ruud, K.; Frediani, L. *Phys. Chem. Chem. Phys.* **2016**, *18*, 21145–21161.

[14] Kato, T. *Comm. Pure Appl. Math.* **1957**, *10*, 151.

[15] Kutzelnigg, W. *Theoret. Chim. Acta* **1985**, *68*, 445–469.

[16] Klopper, W.; Manby, F. R.; Ten-No, S.; Valeev, E. F. *Int. Rev. Phys. Chem.* **2006**, *25*, 427–468.

[17] Kong, L.; Bischoff, F. A.; Valeev, E. F. *Chem. Rev.* **2012**, *112*, 75–107.

[18] Bischoff, F. A.; Harrison, R. J.; Valeev, E. F. *J. Chem. Phys.* **2012**, *137*, 104103.

[19] Fliegl, H.; Hättig, C.; Klopper, W. *J. Chem. Phys.* **2006**, *124*, 044112.

[20] Neiss, C.; Hättig, C.; Klopper, W. *J. Chem. Phys.* **2006**, *125*, 64111.

[21] Köhn, A. *J. Chem. Phys.* **2009**, *130*, 104104.

[22] Christiansen, O.; Koch, H.; Jorgensen, P. *Chem. Phys. Lett.* **1995**, *243*, 409–418.

[23] Großmann, S. *Funktionalanalysis : im Hinblick auf Anwendungen in der Physik*, 4th ed.; Studien-Text: Physik; Aula-Verlag: Wiesbaden, 1988.

[24] Rohwedder, T. An Analysis for some Methods and Algorithms of Quantum Chemistry. Doctoral thesis.

[25] Schneider, R.; Weber, T. *Appl. Numer. Math.* **2006**, *56*, 1383 – 1396.

[26] Yserentant, H. *Regularity and Approximability of Electronic Wave Functions*; Lecture Notes in Mathematics; Springer Berlin Heidelberg, 2010.

[27] Szabo, A.; Ostlund, N. *Modern Quantum Chemistry: Introduction to Advanced Electronic Structure Theory*; Dover Books on Chemistry; Dover Publications, 1989.

[28] Genovese, L.; Deutsch, T.; Neelov, A.; Goedecker, S.; Beylkin, G. *J. Chem. Phys.* **2006**, *125*, 074105.

[29] Genovese, L.; Neelov, A.; Goedecker, S.; Deutsch, T.; Ghasemi, S. A.; Willand, A.; Caliste, D.; Zilberberg, O.; Rayson, M.; Bergman, A.; Schneider, R. *J. Chem. Phys.* **2008**, *129*, 014109.

[30] Beylkin, G.; Mohlenkamp, M. J. *SIAM Journal on Scientific Computing* **2005**, *26*, 2133–2159.

[31] Danos, M.; Rafelski, J. *Pocketbook of Mathematical Functions*; Verlag Harri Deutsch - Thun, 1984.

[32] MADNESS*: Multiresolution Adaptive Numerical Environment for Scientific Simulation*, *https://github.com/m-a-d-n-e-s-s/madness*,.

[33] Harrison, R. J. et al. *Siam J. Sci. Comput.* **2016**, *38*, 123–142.

[34] Hassani, S. *Mathematical Physics: A Modern Introduction to Its Foundations*, 2nd ed.; Springer, 2013.

[35] Daubechies, I. *Ten Lectures on Wavelets*; CBMS-NSF Regional Conference Series in Applied Mathematics; Society for Industrial and Applied Mathematics, 1992.

[36] Jensen, S. R. Real-space all-electron Density Functional Theory with Multiwavelets. Doctoral thesis, 2014.

[37] Alpert, B. K. *SIAM J. Math. Anal.* **1993**, *24*, 246–262.

[38] Alpert, B.; Beylkin, G.; Gines, D.; Vozovoi, L. *J. of Comp. Phys.* **2002**, *182*, 149–190.

[39] Geronimo, J. S.; Iliev, P.; Assche, W. V. *SIAM J. Math. Anal.* **2017**, *49*, 626–645.

[40] Bischoff, F. A. *J. Chem. Phys.* **2014**, *141*, 184106.

[41] Bellman, R.; Corporation, R. *Dynamic Programming*; Rand Corporation research study; Princeton University Press, 1957.

[42] Bischoff, F. A.; Valeev, E. F. *J. Chem. Phys.* **2011**, *134*, 104104.

[43] Beylkin, G.; Coifman, R.; Rokhlin, V. *Comm. Pure Appl. Math.* **1991**, *44*, 141–183.

[44] Beylkin, G. *Proc. Symp. Appl. Math.* **1993**, *47*, 89–117.

[45] Beylkin, G.; Mohlenkamp, M. J. *Proc. Natl. Acad. Sci. U.S.A.* **2002**, *99*, 10246–10251.

[46] Bjørgve, M. Separable representations of the Poisson, Helmholtz and complex Helmholtz kernels. Master thesis, 2017.

[47] Jeziorski, B.; Monkhorst, H. J.; Szalewicz, K.; Zabolitzky, J. G. *J. Chem. Phys.* **1984**, *81*, 368–388.

[48] Bukowski, R.; Jeziorski, B.; Szalewicz, K. *J. Chem. Phys.* **1999**, *110*, 4165–4183.

[49] Shavitt, I.; Bartlett, R. *Many-Body Methods in Chemistry and Physics: MBPT and Coupled-Cluster Theory*; Cambridge Molecular Science; Cambridge University Press, 2009.

[50] Wick, G. C. *Phys. Rev.* **1950**, *80*, 268–272.

[51] Helgaker, T.; Jorgensen, P.; Olsen, J. *Molecular electronic-structure theory*; John Wiley & Sons Inc, 2000.

[52] Čížek, J. *Adv. Chem. Phys.*; John Wiley & Sons, Inc., 2007; pp 35–89.

[53] Schwindt, J. *Conceptual Basis of Quantum Mechanics*; Undergraduate Lecture Notes in Physics; Springer International Publishing, 2015.

[54] Fock, V. *Z. Phys.* **1932**, *75*, 622–647.

[55] Jordan, P.; Klein, O. *Z. Phys.* **1927**, *45*, 751–765.

[56] Schweber, S. *An Introduction to Relativistic Quantum Field Theory*; Harper & Row, 1961.

[57] Christiansen, O.; Jørgensen, P.; Hättig, C. *Int. J. Quantum Chem* **1998**, *68*, 1–52.

[58] Olsen, J.; Jørgensen, P. *J. Chem. Phys.* **1985**, *82*, 3235–3264.

[59] Langhoff, P. W.; Epstein, S. T.; Karplus, M. *Rev. Mod. Phys.* **1972**, *44*, 602–644.

[60] Hättig, C. *Adv. Quant. Chem.* **2005**, *50*, 37–60.

[61] Köhn, A.; Tajti, A. *J. Chem. Phys* **2007**, *127*, 044105.

[62] Plasser, F.; Crespo-Otero, R.; Pederzoli, M.; Pittner, J.; Lischka, H.; Barbatti, M. *J. Chem. Theory Comput.* **2014**, *10*, 1395–1405.

[63] Kjønstad, E. F.; Myhre, R. H.; Martínez, T. J.; Koch, H. *J. Chem. Phys.* **2017**, *147*, 164105.

[64] Kats, D.; Usvyat, D.; Schütz, M. *Phys. Rev. A* **2011**, *83*, 062503.

[65] Wälz, G.; Kats, D.; Usvyat, D.; Korona, T.; Schütz, M. *Phys. Rev. A* **2012**, *86*, 052519.

[66] Schirmer, J. *Phys. Rev. A* **1982**, *26*, 2395–2416.

[67] Bischoff, F. A. *J. Chem. Phys.* **2014**, *141*, 184105.

[68] Hugenholtz, N. *Physica* **1957**, *23*, 481 – 532.

[69] Goldstone, J. *Proc. Roy. Soc. A* **1957**, *239*, 267–279.

[70] Ten-no, S. *Chem. Phys. Lett.* **2004**, *398*, 56–61.

[71] Seelig, F. F. *Z. Naturforsch. A* **1966**, *21*, 1368.

[72] Head-Gordon, M.; Rico, R. J.; Oumi, M.; Lee, T. J. *Chem. Phys. Lett.* **1994**, *219*, 21–29.

[73] Kottmann, J. S. Numerical calculation of exicted states in multiresolution multiwavelet bases. Master thesis, 2014.

[74] Hättig, C.; Weigend, F. *J. Chem. Phys.* **2000**, *113*, 5154–5161.

[75] TURBOMOLE *V7.0 2015, a development of University of Karlsruhe and Forschungszentrum Karlsruhe GmbH, 1989-2007, TURBOMOLE GmbH, since 2007; available from*
http://www.turbomole.com.

[76] KOALA, *an ab-initio electronic structure program, written by S. Höfener with contributions from A. S. Hehn, J. Heuser, and N. Schieschke.*

[77] Höfener, S. *J. Comp. Chem.* **2014**, *35*, 1716–1724.

[78] Dunning, T. H. *J. Chem. Phys.* **1989**, *90*, 1007–1023.

[79] Wilson, A. K.; van Mourik, T.; Dunning, T. H. *J. Mol. Struc.-Theochem.* **1996**, *388*, 339–349.

[80] Peterson, K. A.; Woon, D. E.; Dunning, T. H. *J. Chem. Phys.* **1994**, *100*, 7410–7415.

[81] Kendall, R. A.; Dunning, T. H.; Harrison, R. J. *J. Chem. Phys.* **1992**, *96*, 6796–6806.

[82] Weigend, F.; Köhn, A.; Hättig, C. *J. Chem. Phys.* **2002**, *116*, 3175–3183.

[83] Hättig, C. *Phys. Chem. Chem. Phys.* **2004**, 59–66.

[84] Ranasinghe, D. S.; Petersson, G. A. *J. Chem. Phys.* **2013**, *138*, 144104.

[85] Halkier, A.; Helgaker, T.; Jorgensen, P.; Klopper, W.; Koch, H.; Olsen, J.; Wilson, A. K. *Chem. Phys. Lett.* **1998**, *286*, 243–252.

[86] Momma, K.; Izumi, F. *J. Appl. Crystallogr.* **2011**, *44*, 1272–1276.

[87] Yanai, T.; Fann, G. I.; Gan, Z.; Harrison, R. J.; Beylkin, G. *J. Chem. Phys.* **2004**, *121*, 6680–6688.

[88] Kalos, M. H. *Phys. Rev.* **1962**, *128*, 1791–1795.

[89] Höfener, S.; Klopper, W. *Chem. Phys. Lett.* **2017**, *679*, 52–59.

Ich erkläre, dass ich die Dissertation selbständig und nur unter Verwendung der von mir gemäß 7 Abs. 3 der Promotionsordnung der Mathematisch-Naturwissenschaftlichen Fakultät, veröffentlicht im Amtlichen Mitteilungsblatt der Humboldt-Universität zu Berlin Nr. 126/2014 am 18.11.2014 angegebenen Hilfsmittel angefertigt habe.

Berlin, den _____

_____
Jakob Kottmann